THE UNIVERSITY OF CHICAGO

FROM CANCER CELL INTRINSIC TO EXTRINSIC FACTORS

A DISSERTATION SUBMITTED TO

THE FACULTY OF THE DIVISION OF THE BIOLOGICAL SCIENCES

AND THE PRITZKER SCHOOL OF MEDICINE

IN CANDIDACY FOR THE DEGREE OF

DOCTOR OF PHILOSOPHY

COMMITTEE ON CANCER BIOLOGY

BY

CHUFAN CAI

CHICAGO, ILLINOIS

JUNE 2024

To my parents and Daozheng

The journey of a PhD is not just about academic achievement,

but about personal growth and resilience.

TABLE OF CONTENTS

LIST OF FIGURES

LIST OF TABLES

ACKNOWLEDGMENTS

I couldn’t have reached this stage without the help of many people during my PhD and in my life. I would like to take this opportunity to express my sincere gratitude for their support.

First and foremost, I would like to thank my mentor, Dr. Jing Chen. During the lowest point of my PhD, Jing generously took me into his lab and helped me go back on track, he fully supported, cared, and guided me over the years. Not only is he an extraordinary scientist from whom I've gleaned invaluable insights into scientific thinking, but he is also my career coach and life mentor. Jing has taught me how to work with people with an open mind, considering others' perspectives, and how to be a team player. He has showed me how to gain confidence in the long run and prioritize what truly matters. Without Jing’s support and mentorship, it would be impossible for me to complete my PhD study.

Second, I would like to thank my co-mentor, Dr. Simon Schwörer. Simon is always willing to share his thoughts and ideas and I have deeply benefited from his hands-on mentorship and his way of thinking and interpreting results. I really appreciate the chance to work so closely with a young, energetic, and brilliant scientist, who has truly inspired me. Simon always dedicates his time to help me refine my presentations and prepare for interviews, as well as providing constructive feedback on my writings. Simon’s mentorship plays a substantial role in shaping my academic growth.

Third, I would like to thank my thesis committee members, Dr. Barbara Kee and Dr. Scott Oakes for their insights and time invested on my projects. Specifically, my committee chair, Dr. Brandon Faubert, for writing my letters.

Next, I would like to thank all my Chen Lab and Schwörer Lab colleagues for all the insightful discussions and help. Specifically, Dr. Rong Wu and Dr. Jiayi Tu, who have contributed to the AHCYL1 project, and taught me scientific techniques and skills.

Importantly, I must express my deepest gratitude to my parents. Throughout my entire PhD journey spanning five years, I have not seen them in person. Despite the distance, they have shown great understanding and support, recognizing the inherent anxieties, stresses, and busyness that come with pursuing a PhD. They made every effort to minimize “disruptions” in my study during this time. I promise here that this will never happen again, and I commit to seeing them at least once a year from now on. I am immensely grateful for their love and sacrifice.

The person I want to thank the most is Daozheng Gong, my fiancé. He understands me, tolerates me, and provides full spiritual support during my PhD. I am always inspired and motivated by his love for science. It would be impossible for me to complete my PhD study without Daozheng.

ABSTRACT

When talking about cancer, a lot of hallmarks can picture it, such as self-sufficiency in growth signals, evading apoptosis, invasion, and metastasis, and so on. However, the driving factor that really defines a cancer is oncogenic mutation, the intrinsic feature of a cancer cell. Over the years, efforts and progresses have been made in targeting either oncogenes themselves or their downstream effectors, but cancer still remains the second leading cause of deaths out of all diseases. More and more studies seek therapeutic opportunities by looking into other cancer vulnerabilities, and the cancer extrinsic factors have gained much attention in the recent years, such as the immune system, tumor microenvironment, and cell-cell interaction. Here, I will present my doctoral research, a study from cancer cell intrinsic factors to extrinsic factors and both directions decipher the molecular mechanisms of a tumor.

For cancer intrinsic factor study, we looked at cancer cell metabolic alterations that are oncogene dependent. Here we report that, from an RNAi screen, the top candidate AHCYL1 is overexpressed in human melanoma harboring mutant *NRAS* but not *BRAF* or *WT*. In addition, AHCYL1 is selectively critical for both *NRAS*-mutated human melanoma cell proliferation and tumor growth. Specifically, we identify AHCYL1 as an oncogene-dependent key regulator of ER calcium homeostasis, with its deficiency leading to decreased ER calcium levels, activating the UPR and ultimately causing cell apoptosis. Our findings suggest that targeting the AHCYL1-IP3R axis presents a novel therapeutic approach for *NRAS*-mutated melanomas, with potential applicability to all cancers harboring *RAS* mutations, such as *KRAS*-mutated human colorectal cancers.

For the cancer extrinsic factor study, from a high-content screen using a human blood nutrient library in combination with a fibroblast reporter (FIRE) system, we identified and

validated that extracellular ATP (eATP) blunts TGFβ-induced SMA expression and promotes cytokines-induced IL-6 expression in pancreatic stellate cells (PSCs) in both time- and dose-dependent manner. Pretreatment of PSCs with physiological concentrations of eATP is sufficient to alter fibroblast states and to promote PDAC tumor growth. Mechanistically, our data suggest that eATP acts independently of its canonical purinergic receptor pathways to promote an iCAF state in PSCs. The JAK-STAT pathway, one of the major regulators of iCAFs, is strongly activated upon eATP treatment and mediates its effect in inducing an iCAF state. Further, we showed that this is serum dependent. These findings support the idea that TME metabolites can alter PDAC progression by regulating CAF heterogeneity.

CHAPTER 1: INTRODUCTION

1.1 Targeting oncogenic *RAS* is challenging

Oncogenes are genes that when mutated or overexpressed can promote cancer development, such as *RAS*, *RAF*, and *EGFR*.

Ras is a family of small guanosine triphosphatase (GTPase) that serve as molecular switches that are active when bound with guanosine triphosphate (GTP) and inactive when bound with guanosine diphosphate (GDP) (Figure 1.1). The switch between active and inactive form of Ras governs important cellular processes, including cell proliferation, differentiation, and survival. When *RAS* is mutated, it's locked in the permanent active state that continuously initiates downstream signaling that fostering uncontrolled cell proliferation and can drive cancer.

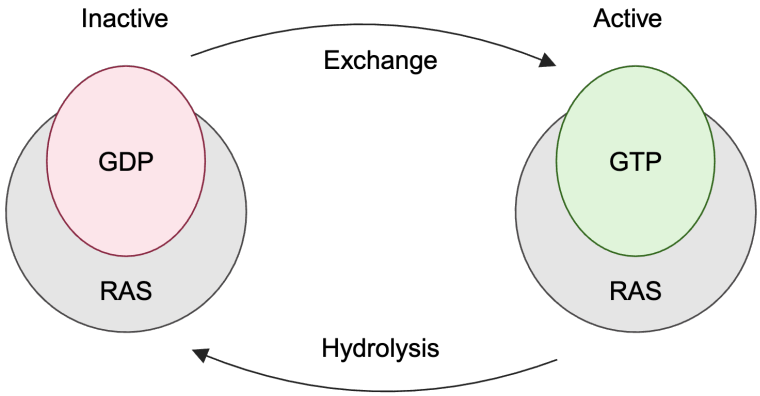

Figure 1.1 RAS switches between active and inactive form.

RAS mutations in *HRAS*, *KRAS*, and *NRAS*, are the most frequent mutations found in human cancers, for example, pancreatic ductal adenocarcinoma (PDAC), colorectal adenocarcinoma, lung adenocarcinoma, and melanoma (Table 1.1) (Moore et al. 2020). Over the years, a lot of efforts have been made on developing effective inhibitors against RAS proteins.

Human cancer types	***RAS* mutation isoforms**	**Frequency**
Pancreatic ductal adenocarcinoma	KRAS	86%
Colorectal adenocarcinoma	KRAS	41%
Lung adenocarcinoma	KRAS	32%
Melanoma	NRAS	29%
Head and neck squamous cell carcinoma	HRAS	5%
Bladder urothelial carcinoma	HRAS	4%

Table 1.1 *RAS* mutations and frequencies in human cancers.

However, targeting RAS proteins is extremely challenging. RAS has long been labeled as "undruggable" due to its small, smooth-surfaced globular shape that lacks the distinct binding pockets (Moore et al. 2020). This structural feature complicates the design of molecules capable of effectively disrupting mutated RAS activity without affecting normal RAS activity that plays critical roles in other non-cancer cells.

Despite the ever-present challenges of targeting RAS mutant itself, multiple RAS inhibitors have been successfully developed in the recent years. Notably, two KRAS inhibitors, Sotorsib and Adagrasib, have been approved by the U.S. Food and Drug Administration (FDA). However, both inhibitors specifically target *KRAS G12C*, a *KRAS* mutation that is most prevalent in human lung adenocarcinoma (comprising 46% of all *KRAS* mutations), but less commonly found in other *RAS*-mutated cancers, such as PDAC (less than 2%) and CRC (around 10%) (Qunaj et al. 2023; Moore et al. 2020; Singhal, Li, and O'Reilly 2024). Thus, RAS targeting inhibitors are still limited, and more RAS inhibitors are currently under clinical trials (Singhal,

Li, and O'Reilly 2024). Yet, another concern is developed drug resistance after *RAS* targeting: nearly all patients with identified resistance mutations acquire alterations that reestablish RAS-MAPK signaling (Singhal, Li, and O'Reilly 2024).

In conclusion, not only do we need to develop more effective oncogene inhibitors, but also, we need a better understanding of other vulnerabilities of cancers. Following sections will discuss my studies on aiming to better understand melanoma harboring mutant *NRAS* and PDAC harboring mutant *KRAS*.

1.2 Human cutaneous melanoma harbors mutually exclusive oncogene mutations

Melanoma is a type of skin cancer that arises from the melanocytes, the pigment-producing cells in the skin. Human cutaneous melanoma only accounts for 1 - 2% of all skin cancers but is responsible for over 75% of skin cancer deaths, making melanoma the most dangerous type of skin cancers ("Melanoma" 2018).

Raf proteins are a family of cytosolic serine/threonine kinases that are part of the Ras-Raf-MAPK pathway. There are three Raf kinase members in the family: A-Raf, B-Raf, and c-Raf (Raf-1). Mutations in the human *RAF* gene leads to its constitutive activation that causes malignant transformation (Leicht et al. 2007).

Nearly 50% of the melanoma patients exhibit *BRAF* mutations (90% of them are *BRAF V600E*), 20% of the patients express mutant *NRAS*, and 5% of the patients harbor mutated *KIT*. The rest of the human cutaneous melanomas are considered as wild type (*WT*), means there are no *BRAF*, *NRAS*, or *KIT* mutation, or basically, any driver mutation found yet in these patients (Figure 1.2). Worth noting is that, mutations in human melanoma are mutually exclusive, meaning that usually we only see one mutation within the same patient (Deng et al. 2019).

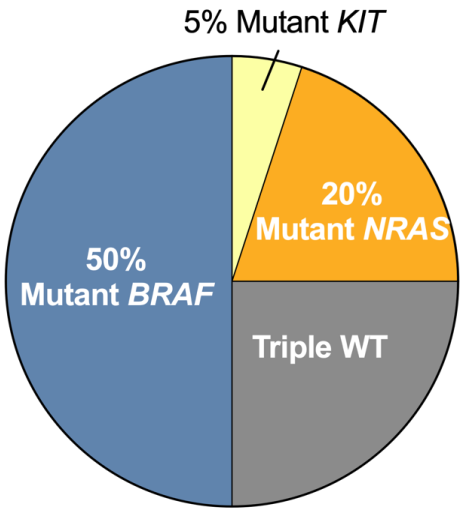

Figure 1.2 Oncogene mutations in human cutaneous melanoma.

Treatments for melanoma patients harboring mutant *BRAF* have been developed. The standard of care is a combination of BRAF and MEK inhibitors (Bollag et al. 2012; D. B. Johnson and Sosman 2013), and currently FDA approved BRAF inhibitors include Vemurafenib, Dabrafenib, and Encorafenib, MEK inhibitors include Trametinib, Cobimetinib, and Binimetinib (Gonzalez-Cao et al. 2023).

NRAS-mutated melanoma is typically more aggressive than *BRAF*-mutated or *WT* melanomas (Thomas et al. 2015; Jakob et al. 2012; Liszkay et al. 2021; Devitt et al. 2011). However, there is currently no specific treatment available for *NRAS*-mutated melanoma, and *NRAS* mutated melanomas are not susceptible to BRAF inhibitors, presenting poor prognosis. Thus, treatments specific for *NRAS* mutant harboring melanoma patients are required.

Over the past decade, our research group and others elucidated multiple oncogene-specific metabolic regulations (Xia et al. 2017; Kang et al. 2015; Gao et al. 2022; Zhao et al. 2017; Lin et al. 2018; Min and Lee 2018; Tarrado-Castellarnau, de Atauri, and Cascante 2016).

Specifically, we identified and reported two *NRAS* specific metabolic alterations in human melanoma, Phospholipase A2, group VII (PLA2G7) and Adenosylhomocysteinase like protein 1 (AHCYL1). PLA2G7 and Lyso-PAF act as key elements of RAS-RAF1 signaling and exhibit intracellular signaling functions (Gao et al. 2022). Our AHCYL1 story highlights the concept of oncogene-specific calcium regulation in cancer cells, and sheds light on oncogene-mediated metabolic rewiring in cancer cells compare to normal cells, providing new insights in development of novel precision medicine for cancer treatment (Hanahan 2022).

1.3 Endoplasmic reticulum (ER) calcium homeostasis and the unfolded protein response (UPR)

The ER is the major intracellular site for calcium storage and release that modulates cellular calcium homeostasis, and it coordinates with mitochondria and lysosomes. Calcium levels in these cellular compartments are much higher than in the cytosol (Table 1.2).

Cellular compartments	Calcium concentration
Extracellular space	1 - 2 mM
ER	300 μM -1 mM
Mitochondria	0.1 nM - 1 mM
Cytosol	50 - 100 nM
Endolysosome	~500 μM

Table 1.2 Reported cellular calcium levels (Trebak and Kinet 2019).

The ER calcium is mainly regulated by the second messenger, Inositol 1,4,5-triphosphate (IP3). Upon extracellular signal received by G protein-coupled receptors (GPCRs) and receptor tyrosine kinases (RTKs), phospholipase C (PLC) is activated and hydrolyzes phosphatidylinositol 4,5-bisphosphate (PIP2) into IP3 and diacylglycerol (DAG). Then, IP3 diffuses rapidly through the cytoplasm and binds to IP3 receptors (IP3Rs) located on the ER, which induces the release of calcium from intracellular stores within the ER lumen into the cytoplasm and act as secondary massagers and mediate a wide range of cellular responses.

The ER is mostly composed of calcium-dependent molecular chaperones that are responsible for protein folding. Thus, disrupting ER calcium homeostasis causes the accumulation of unfolded or misfolded proteins and subsequently leads to ER stress that attenuates cell proliferation or triggers apoptosis (Sehgal et al. 2017; Preissler et al. 2020; Ibarra et al. 2022; Krebs, Agellon, and Michalak 2015; Luo and Lee 2013; Bahar, Kim, and Yoon 2016; Monteith, Prevarskaya, and Roberts-Thomson 2017; Krebs, Groenendyk, and Michalak 2011).

Disturbed ER calcium homeostasis can cause ER stress, and the accumulation of misfolded and unfolded proteins can activate the URP, which is initiated by three ER membrane-bound sensors: inositol-requiring enzyme 1 (IRE1), protein kinase RNA-like ER kinase (PERK) and activating transcription factor 6 (ATF6) (Figure 1.3).

Upon detection of unfolded proteins, IRE1 undergoes oligomerization and autophosphorylation, leading to its activation. Activated IRE1 possesses endoribonuclease activity, which mediates the unconventional splicing of X-box binding protein 1 (XBP1) mRNA. Spliced XBP1 mRNA encodes a transcription factor, XBP1s, which translocates to the nucleus

and activates the expression of genes. For detecting the activation of the IRE1 branch, one can detect XBP1 splicing by gel electrophoresis (Chalmers et al. 2017).

For the PERK branch, ER stress triggers PERK dimerization and autophosphorylation, leading to its activation as a kinase. Activated PERK phosphorylates the alpha subunit of eukaryotic translation initiation factor 2 (eIF2α), resulting in global translation attenuation. However, translation of selective mRNAs, such as activating transcription factor 4 (ATF4), is enhanced under these conditions. For detecting the PERK branch activation, people usually detect eIF2α phosphorylation and ATF4 protein levels.

For the ATF6 branch, ER stress induces the trafficking of ATF6 from the ER to the Golgi apparatus, where it undergoes proteolytic cleavage by site-1 and site-2 proteases (S1P and S2P). This cleavage releases the cytosolic fragment of ATF6, which acts as a transcription factor. For detecting ATF6 branch, people usually detect ATF6 cleavage.

Ultimately, all three branches of the UPR lead to transcription of genes involved in ER protein folding, ER-associated degradation (ERAD), lipid metabolism, and antioxidant responses. With resolved ER stress, they restore ER homeostasis and promote cell survival; with unresolved and persistent ER stress, the UPR causes cell apoptosis.

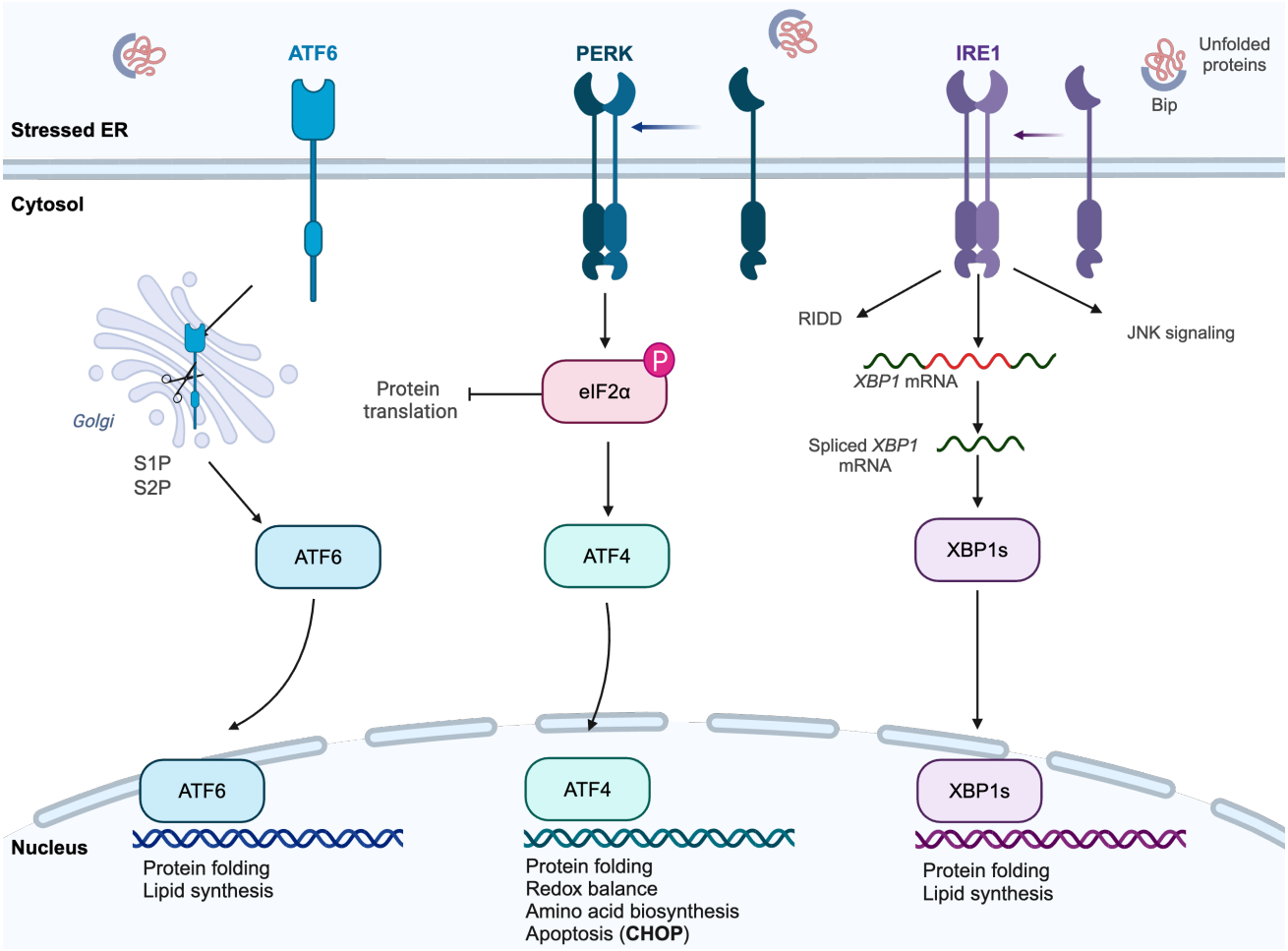

Figure 1.3 The UPR signaling pathway (created with BioRender.com).

1.4 AHCYL1 governs ER calcium homeostasis

Adenosylhomocysteinase (AHCY) is an enzyme in the methionine-homocysteine cycle that catalyzes S-Adenosylhomocysteine (SAH) into adenosine and L-homocysteine. Worth noting is that, AHCY is the only protein in mammals that can perform this reaction.

There are two other proteins that share similar structure as AHCY: they are AHCY like protein 1 (AHCYL1) and AHCY like protein 2 (AHCYL2) (Devogelaere, Sammels, and De Smedt 2008).

Comparing to AHCY, AHCYL1 is consisted of a similar AHCY domain and an extra IRBIT domain (Figure 1.4). In its AHCY domain, there are two point mutations at site 256 and site 450 as well as an extra coiled-coil region, making AHCYL1 no longer present any enzymatic functions (Devogelaere, Sammels, and De Smedt 2008). Its IRBIT domain has been reported to bind to all three types of the IP3Rs and compete with second messenger IP3 and suppress IP3R activity (Ando et al. 2006) (Figure 1.5). Worth noting is that, such competition between IP3 and AHCYL1 is concentration dependent: at physiological IP3 concentrations, IP3 can't activate IP3R under the expression of AHCYL1; however, at high IP3 concentrations, such as 10 μM, the effect of AHCYL1 can be overridden by IP3 (Ando et al. 2006).

AHCYL2 consists of the same AHCY and IRBIT domain as AHCYL1 but an extra P/A domain (Figure 1.4). The extra P/A domain is rich in proline and alanine and thus non-structural (Figure 1.4), making its IRBIT hardly interact with the IP3R as AHCYL1 (Devogelaere, Sammels, and De Smedt 2008).

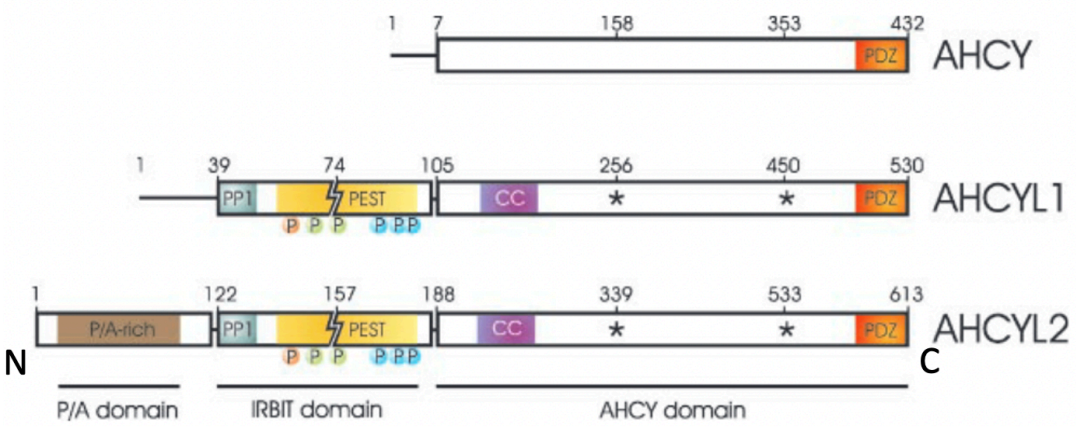

Figure 1.4 A summary of AHCY family protein structures (Devogelaere, Sammels, and De Smedt 2008).

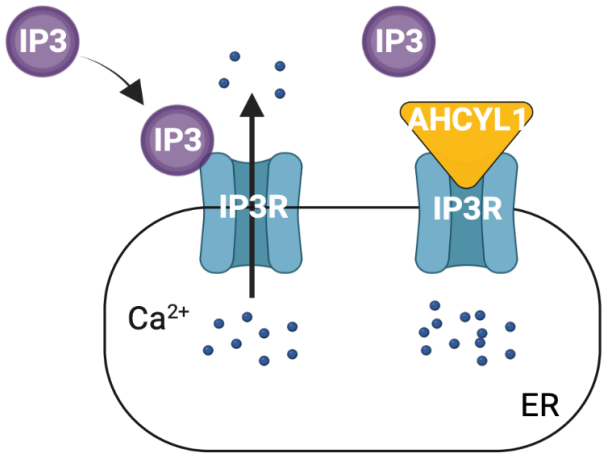

Figure 1.5 AHCYL1 is an inhibitory gatekeeper of the IP3R (created with BioRender.com).

1.5 Challenges in human PDAC therapies

Human PDAC represents 90% of all pancreatic malignancies, and it is one of the most aggressive cancers, with a five-year survival rate of 13% (American Cancer Society 2024). PDAC is predicted to become the second leading cause of cancer-related deaths in the United States by 2030 (Orth et al. 2019).

A heathy pancreas has two major functions: the endocrine function, which involves the secretion of hormones by endocrine cells within the islets of Langerhans to regulate blood sugar levels, and the exocrine function, which controls the secretion of digestive enzymes by acinar cells to support food digestion. Very rare malignancy cases originate from the endocrine component of a pancreas, causing pancreatic neuroendocrine tumor (PanNET). Notably, the majority of PDAC (90%) originate from the exocrine component of the pancreas.

Despite the aggressiveness of PDAC, current treatments for PDAC are limited and lack efficiency (Principe et al. 2021).

Surgical resection is considered the primary treatment for localized PDAC and offers the best chance for long-term survival. However, early detection of feasibly respectable PDAC is challenging, because early-stage PDAC often does not cause specific symptoms from its deep location of the pancreas. Not to say that the PDAC surgery, pancreaticoduodenectomy (Whipple procedure), is one of the most complicated surgeries (Are, Dhir, and Ravipati 2011; Karim et al. 2018).

PDAC patients also receive chemotherapy both before and after a surgery, often with gemcitabine-based regimens (e.g., gemcitabine plus nab-paclitaxel or FOLFIRINOX) (Garajová et al. 2023). Neoadjuvant chemotherapy may be used to shrink the tumor and improve the likelihood of successful surgery in patients with initially unresectable tumors. Adjuvant

chemotherapy is given after surgery to reduce the risk of cancer recurrence. However, chemotherapy only offers modest benefits for PDAC overall survival, in that many patients do not respond well to chemotherapy and toxicity and chemoresistance can develop (Principe et al. 2021).

Human PDAC is another cancer type that has prominent mutations in *RAS*, with around 90% of the PDAC patients harbor mutant *KRAS* (Moore et al. 2020). Other PDAC somatic mutations include *p53* mutations in 80% of cases, *CDKN2A* mutations in 60% of cases, and *SMAD4* mutations in 40% of cases (Garajová et al. 2023). *KRAS* alterations include G12D (42%), G12V (32%), G12R (15%), G12C (1.5%), G12A (0.4%) and G12S (0.1%) (Kolbeinsson et al. 2023). Despite the ever-present challenge of targeting RAS proteins directly as discussed in section 1.1, several KRAS inhibitors are under clinical trial. For example, MRTX1133 is a non-covalent, selective KRAS G12D inhibitor, and a phase I study (NCT05737706) of MRTX1133 in KRAS G12D advanced solid tumors is proceeding (Wang et al. 2022; Zhou et al. 2023; Kemp et al. 2023).

In addition to targeting the intrinsic features of PDAC cancer cells, with a growing understanding of PDAC biology, much work has focused on PDAC tumor microenvironment (TME).

1.6 PDAC has a complicated TME

PDAC is characterized by prominent desmoplastic response, in which the dense stroma can make up to 90% of the tumor mass (Helms, Onate, and Sherman 2020) (Figure 1.6). A tumor stroma mainly consists of basement membrane, cancer associated fibroblasts (CAFs), extracellular

matrix (ECM) (collagens, glycoproteins, polysaccharides), immune cells, and vasculature. Attempts have been made to target these components within PDAC stroma.

PDAC is a poorly immune infiltrated, immunologically "cold" tumor (Karamitopoulou 2019). PDAC (excluding MSI-high tumors) did not show any response to immunotherapies. Limited $CD8^+$ cytotoxic effector T cells infiltrate and the broad immunity within a PDAC is mostly immunosuppressive myeloid cells and Tregs. Some studies focus on making tumors immunologically active by activating innate lymphocytes or creating an inflammatory response in the TME, thereby augmenting T cell priming (Balachandran, Beatty, and Dougan 2019).

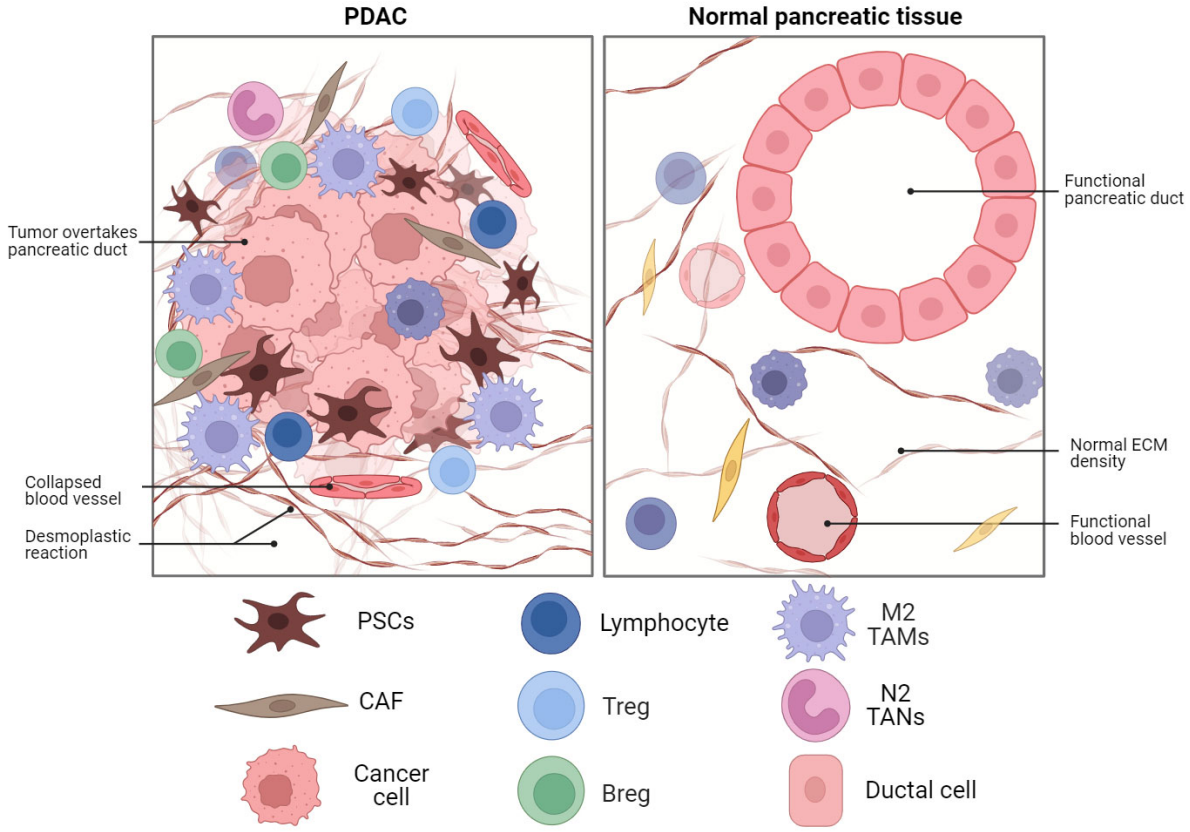

Figure 1.6 A comparison between PDAC TME and normal pancreatic tissue (Adapted from Joseph et al. 2024) (created with BioRender.com).

In addition, PDAC has impaired vasculature from the stromal reaction, which causes poor blood vessel perfusion (Figure 1.6). Abnormal blood vessel structure can cause a hypoxic and nutrient poor TME that contributes to tumor progression and treatment resistance (Kamphorst et al. 2015; Carroll, Buckley, and Kelly 2021). Also, PDAC patients with mature blood vessels have batter overall survival (Katsuta et al. 2019).

Over the years, efforts have also been made in targeting the PDAC ECM. For example, in mice harboring PDAC, targeting hyaluronan improves chemotherapy through more efficient drug delivery (Jacobetz et al. 2013). However, a clinical trial targeting hyaluronan has failed in phase III to show any benefits in PDAC patients (Hakim et al. 2019). In addition, attempts have been made in depleting other ECM components, such as collagen I, but that ultimately promotes PDAC growth and reduces survival in mouse models (Chen et al. 2021). Consistently, depletion of alpha smooth muscle actin (SMA)-expressing CAFs, the source of collagen I, also leads to increased tumor progression (Özdemir et al. 2014). In addition, PDAC patients with higher amount of SMA-expressing CAFs inside the tumors show better overall survival, but they also respond poorly to immunotherapies (Özdemir et al. 2014). These results suggest that depleting certain ECM components can accelerate tumor growth but may present clinical benefits when combined with other therapies, such as chemotherapy and immunotherapy.

Thus, a better understanding of PDAC stroma is needed to develop advanced approaches for therapies that target both the stroma and cancer cells.

1.7 CAFs are heterogeneous

The PDAC stroma has a high abundance of CAFs, which primarily produce the stromal milieu. During the development of PDAC, CAFs can originate from diverse cells, such as pancreatic stellate cells (PSCs), resident tissue fibroblasts, mesenchymal stem cells, endothelial cells, pericytes, and adipocytes (T. Zhang et al. 2022). Among them, PSCs are considered the major source of PDAC CAFs (Hrabák et al. 2021) and are a predominant cell type in the PDAC stroma, and mediate the desmoplastic response (Sousa et al. 2016).

Stellate cells (SCs) are tissue-resident mesenchymal cells and can be found in the liver (hepatic stellate cells) as well as the pancreas (PSCs). SCs are rich in vitamin A and lipids (Watari, Hotta, and Mabuchi 1982), enabling SCs be able to be isolated by differential centrifugation. Under normal conditions, PSCs are quiescent, and they can regulate the production of ECM. PSCs can be activated upon tissue damage, inflammation, and cancer for tissue generation and wound healing. In part because of this, cancer is considered as wounds that do not heal (Dvorak 1986).

Over the last decade, functionally and transcriptionally heterogeneous CAF populations have been identified and gradually appreciated in both mouse and human PDAC (Öhlund et al. 2017; Elyada et al. 2019; Dominguez et al. 2020; Hosein et al. 2019). From a single cell RNA-seq analysis on PDAC tumors from genetically engineered mice, CAF unsupervised clustered into three major populations (Figure 7): myofibroblastic CAFs (myCAFs), inflammatory CAFs (iCAFs), and antigen presenting CAFs (apCAFs) (Elyada et al. 2019).

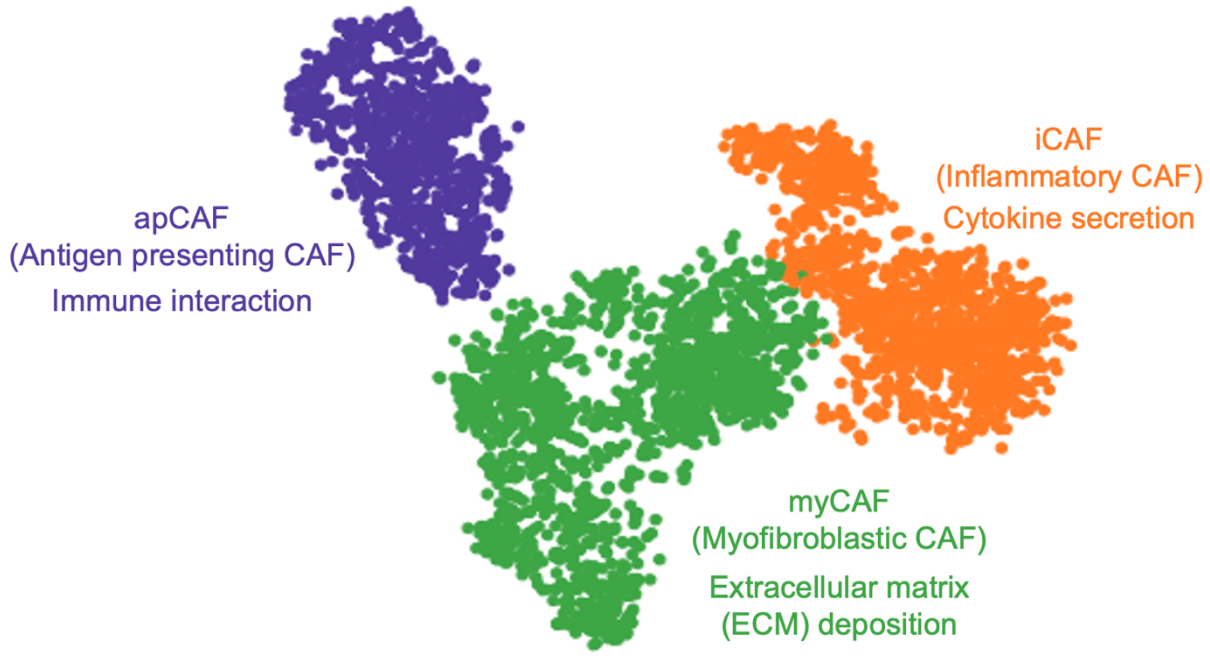

Figure 1.7 CAF clustering from single cell RNA-seq (Elyada et al. 2019).

myCAFs feature expression of SMA, are the main producers of extracellular matrix, and are thought to be tumor restraining (McAndrews et al. 2022; Özdemir et al. 2014). Meanwhile, iCAFs are characterized by low SMA expression and their ability to secret inflammatory cytokines and chemokines such as IL-6 and CXCL1, and are thought to be tumor promoting (McAndrews et al. 2022; Lo et al. 2017; Schwörer et al. 2023). myCAF and iCAFs are the most abundant CAF populations in PDAC, however, another distinct yet smaller CAF population has been identified recently, the apCAFs. apCAFs express MHC II and CD74 but lack classical co-stimulatory molecules; consequently, apCAFs can potentially activate $CD4^+$ T cells but cause anergy (Elyada et al. 2019). Based on their distinct roles in PDAC, selectively altering the CAF states is thought to have significant clinical benefits.

Heterogeneity within the CAF population has been suggested to be established in part by growth factors and cytokines. For example, TGFβ can induce myCAFs, TNFα, IL-1α and LIF can induce the iCAF state, and IFNγ can induce the apCAF state (Biffi et al. 2019; Elyada et al. 2019) (Figure 1.8). While cytokines and growth factors can drive CAF heterogeneity, iCAF and myCAF states are plastic, i.e., they can convert into each other (Figure 1.8). How this plasticity is regulated is largely unknown. Our lab recently identified oxygen availability in the TME as a central regulator of CAF state decisions, indicating that metabolic factors in the tumor microenvironment (TME) can modulate the CAF state (Schwörer et al. 2023).

Thus, we define a CAF state based on the expression of its defined markers, and most importantly, ask whether such state can be greatly altered by the extrinsic environment over cell intrinsic programs.

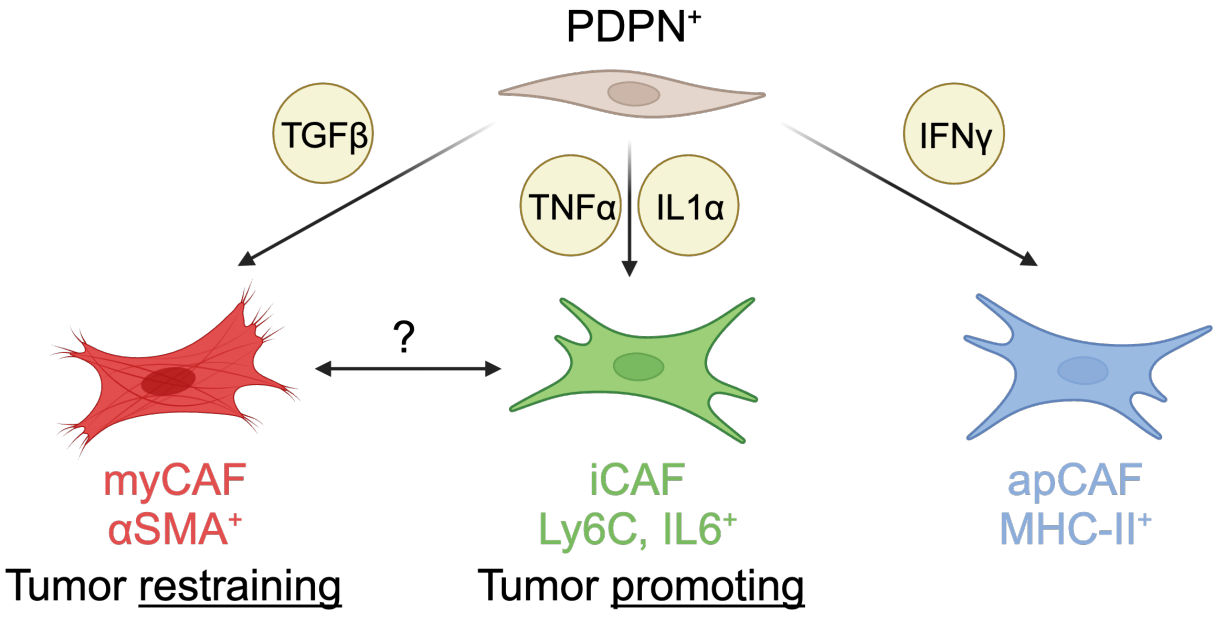

Figure 1.8 CAF heterogeneity can be driven by cytokines and growth factors (created with BioRender.com).

For iCAFs, after receiving extracellular signals from cytokines and growth factors, there are two major intracellular signaling pathways that establish the inflammatory state: JAK-STAT3 pathway and NF-κB pathway (Biffi et al. 2019).

For canonical JAK-STAT signaling pathway, after receiving external stimuli, JAK is recruited to the cell surface receptor and activated by phosphorylation, which leads to the recruitment and phosphorylation of STAT. Then, STAT dimerizes and translocates into the nucleus and regulates gene transcription as transcription factors. JAK-STAT pathway plays crucial roles in inflammatory responses and cell proliferation.

The canonical NF-κB pathway is a central regulator of the immune system and inflammation. NF-κB signaling is triggered by a wide range of extracellular stimuli, including pro-inflammatory cytokines (such as TNF-α and IL-1), microbial pathogens (such as bacterial lipopolysaccharides), and cellular stressors (such as oxidative stress and DNA damage). Then, IκB kinase (IKK) complex is activated and degrades IκB proteins, which releases the NF-κB dimers that translocate into the nucleus and regulates inflammatory gene transcription.

For iCAFs specifically, a recent study showed that IL1 activates the NF-κB pathway and induces LIF expression. Then LIF acts in an autocrine manner to bind and activate the JAK-STAT pathway, which ultimately produces inflammatory mediators, like IL-6 (Figure 1.9) (Biffi et al. 2019).

myCAFs are regulated by the TGFβ/Smad pathway. Upon activation by TGFβ, TGFβ receptor (a kinase) phosphorylates and activates SMAD2 and SMAD3, which then form a complex with SMAD4. The SMAD complex then translocates into the nucleus and initiates gene transcription for ECM remodeling. In the context of cancer, SMAD4 can be a tumor suppressor.

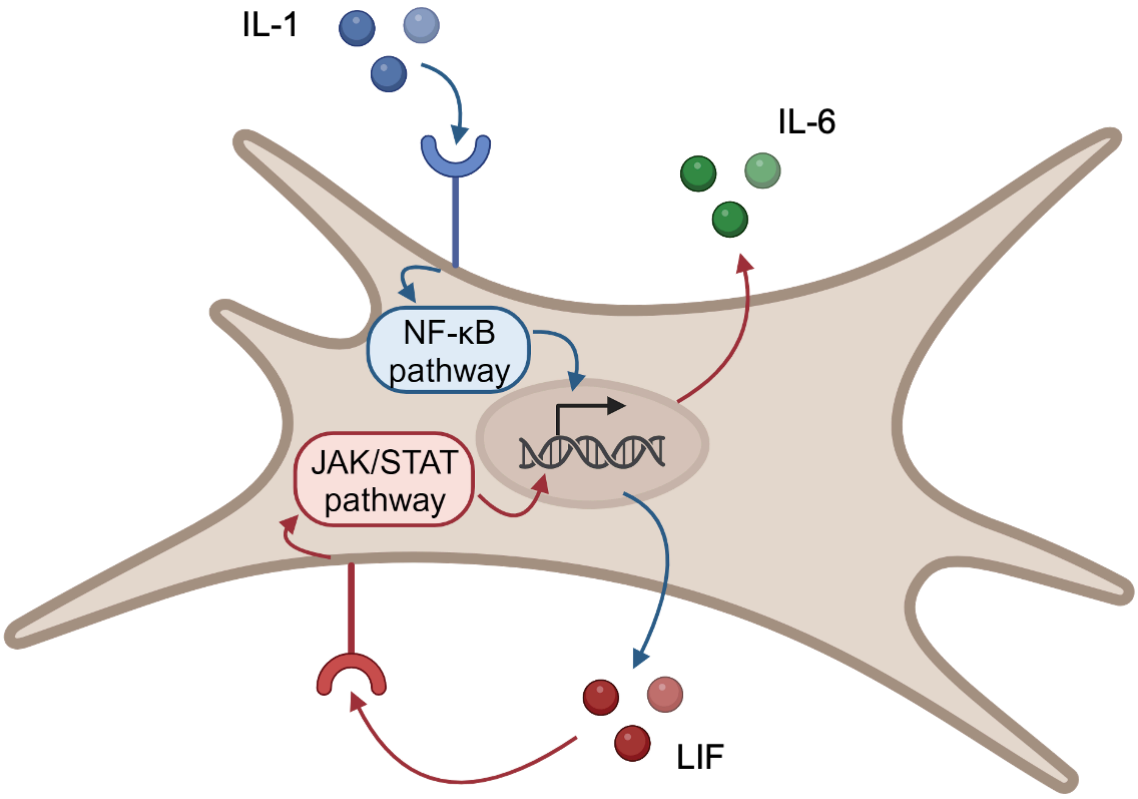

Figure 1.9 Reported major iCAF regulatory pathways (created with BioRender.com).

1.8 Extracellular nucleotides and purinergic receptors

Extracellular adenosine triphosphate (eATP) has been found to accumulate at high micromolar levels in the TME (Pellegatti et al. 2008; L.-P. Hu et al. 2019). eATP accumulates in the TME due to cellular stress and apoptosis; in addition, hypoxia also induces ATP release without cell injury (Di Virgilio et al. 2018). Given the fact that PDAC has necrotic centers and hypoxia regions as discussed in section 1.6, eATP might contribute to iCAF accumulation in PDAC hypoxic regions (Schwörer et al. 2023). Intriguingly, a recent study found macrophages can

release ATP under hypoxia (Bhattacharyya et al. 2022), and macrophages are a major immune population in the PDAC (Poh and Ernst 2021).

Intracellular ATP is an energy carrier, while eATP mainly act as a signaling molecule modulating immune functions. One of the most established pathways is mediated by eATP binding to purinergic receptors (Di Virgilio et al. 2018) (Figure 1.10).

Purinergic receptors are a class of cell membrane receptors include P1 receptors (Adenosine receptors) that are G protein-coupled receptors (GPCRs) activated by adenosine; P2X receptors (P2X1-P2X7) that are ligand-gated ion channels activated by eATP; P2Y receptors that are GPCRs activated by ATP, ADP, UTP, and UDP (Di Virgilio et al. 2018). There are two major outcomes under purinergic receptor activation, intracellular calcium flux and cAMP alteration.

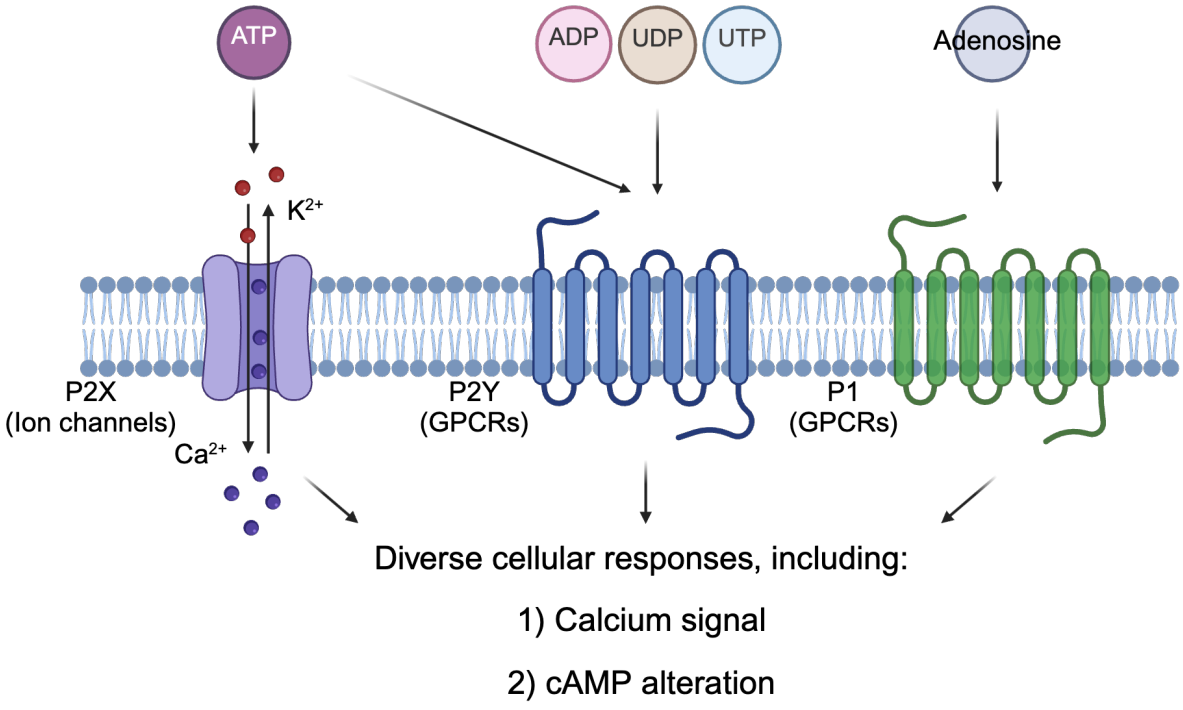

Figure 1.10 Extracellular nucleotides and purinergic receptors (created with BioRender.com).

The ATP molecule is relatively large and contains a lot of negative charges, thus it is thought to be cell impermeable. However, it was found that ATP-treated mouse cells significantly and rapidly increase their membrane permeability, which leads to a massive efflux of nucleotide pools (Chaudry 1982). In addition, some equilibrative nucleoside transporters (ENTs) can mediate the uptake of eATP, although more pronounced in its degraded form, adenosine (Boswell-Casteel and Hays 2017).

CHAPTER 2: NRAS MUTANT DICTATES AHCYL1-GOVERENED ER CALCIUM HOMEOSTASIS FOR MELANOMA TUMOR GROWTH

ACKNOWLEDGEMENTS:

Dr. Rong Wu performed entire experiments and analysis in Fig. 2.1; C-H in Fig. 2.2; B in Fig. 2.3; B-D in sup Fig. 2.1; all the experiments and analysis in sup Fig. 2.4.

Dr. Jiayi Tu performed experiments and analysis of A-E in Fig. 2.2; G&K in Fig. 2.4; all the calcium analysis in sup Fig. 2.7; C&D in sup Fig. 2.8; all the experiments in sup Fig. 2.9.

The rest experiments were all performed by me.

2.1 Introduction

For a long time, calcium signaling in malignancy has not gained much attention as it was once viewed as uniform across all non-excitable cells, including both the normal and the cancer cells. However, over the past decade, accumulating evidence has shown that cancer cells apply altered requirement for calcium homeostasis to fulfill their need for proliferation and survival (Zheng et al. 2022). Since then, calcium signaling has become attractive targets for developing novel cancer therapies, especially ones targeting the ER. The ER is the major intracellular site for calcium storage and release that modulates cellular calcium homeostasis, and it coordinates with mitochondria and lysosomes. The ER is mostly composed of calcium-dependent molecular chaperones that are responsible for protein folding. Thus, disrupting ER calcium homeostasis causes the accumulation of unfolded or misfolded proteins and subsequently leads to ER stress that attenuates cell proliferation or triggers apoptosis (Sehgal et al. 2017; Preissler et al. 2020; Ibarra et al. 2022; Krebs, Agellon, and Michalak 2015; Luo and Lee 2013; Bahar, Kim, and Yoon 2016; Monteith, Prevarskaya, and Roberts-Thomson 2017; Krebs, Groenendyk, and Michalak 2011).

To fulfill their need for proliferation and survival, cancer cells apply differentially expressed calcium pumps, channels, or exchangers, such as the upregulation of IP3R3 (Zheng et al. 2022; Marchi et al. 2020; Monteith, Prevarskaya, and Roberts-Thomson 2017; Marchi and Pinton 2016; Cui et al. 2017). The differential expression of cancer calcium regulating proteins have been reported to be driven by oncogenes and tumor suppressors (Zheng et al. 2022; Bittremieux et al. 2016). Yet, detailed characterization of how calcium signals are remodeled to achieve homeostasis in cancer cells is still needed, and whether different cancer oncogenic

background maintains oncogene-specific calcium homeostasis status remains elusive. Particularly, the effect of oncogene *NRAS* on cellular calcium homeostasis has not been studied.

Human cutaneous melanoma is the most dangerous type of skin cancer, with nearly fifty percent of patients exhibiting *BRAF* mutations and twenty percent expressing mutated *NRAS*. Notably, these mutations are mutually exclusive in melanoma patients. Therefore, we use human melanoma as a model to investigate oncogene-dependent calcium homeostasis regulations and focus on identifying mutant *NRAS* specific requirements. This is because *NRAS*-mutated melanoma is typically more aggressive than *BRAF*-mutated and *wild-type* melanomas (Thomas et al. 2015; Jakob et al. 2012; Liszkay et al. 2021; Devitt et al. 2011), and while clinical treatments for *BRAF*-mutated melanoma involve the combination of BRAF and MEK inhibitors (Bollag et al. 2012; D. B. Johnson and Sosman 2013), there is currently no specific treatment available for *NRAS*-mutated melanoma. Previously in our research group, we conducted a comprehensive RNAi-based screen targeting a subset of genes related to cell metabolism (Kang et al. 2015) in human melanoma cells expressing mutant *NRAS* or *BRAF*. Reanalysis of the screen results reveals that the ER protein AHCYL1, that governs ER calcium homeostasis, is selectively critical for human melanoma expressing *NRAS* mutation.

AHCYL1 has been reported to bind to and suppress the IP3R (Ando et al. 2003). Although AHCYL1 shares a similar protein structure with adenosylhomocysteinase (AHCY), it does not have enzymatic activity due to two site mutations and a coiled-coil region that is not present in AHCY (Devogelaere, Sammels, and De Smedt 2008). IP3R is activated by the binding of IP3. With an additional IRBIT domain, AHCYL1 inhibits

IP3 binding and prevents calcium efflux from the ER induced by IP3, thereby suppresses IP3R activity (Ando et al. 2006; Devogelaere et al. 2006). Previous study has correlated AHCYL1 expression with colorectal cancer patient survival (Li et al. 2022). However, the exact mechanism by which AHCYL1 affects cancer cell proliferation and survival as well as the role of AHCYL1 in human melanoma remain unclear.

Here, we report that, AHCYL1 is selectively critical for human melanoma expressing *NRAS* mutation, but not for those expressing *BRAF* mutation. Specifically, we identify AHCYL1 as an oncogene-dependent key regulator of ER calcium homeostasis, with its deficiency leading to decreased ER calcium levels, activating the UPR and ultimately causing cell apoptosis. Our findings suggest that targeting the AHCYL1-IP3R axis presents a novel therapeutic approach for *NRAS*-mutated melanomas, with potential applicability to all cancers harboring *RAS* mutations, such as *KRAS*-mutated human colorectal cancers.

2.2 Materials and Methods

Cell culture:

Cell experiments were conducted and designed according to protocols approved by the Institutional Biosafety Committee of the University of Chicago.

Human HEK293T (RRID: CVCL_0063), HMCB (RRID: CVCL_3317), A375 (RRID: CVCL_0132), VMM39 (RRID: CVCL_A739), SK-MEL-5 (RRID: CVCL_0527), A2058 (RRID: CVCL_1059), VM1985 (RRID: N/A), VM164 (RRID: N/A), SK- MEL-2 (RRID: CVCL_0069), HT29 (RRID: CVCL_0320), HCT116 (RRID: CVCL_0291), and Hs 936.T (C1; RRID: CVCL_1033) were obtained from the ATCC, Human SK-MEL-147 was from Sigma SCC440 (RRID: CVCL_3876). Human Mel-ST cells were obtained from a 2015 MC paper (Kang et al.(Kang et al. 2015); RRID:N/A). VMM39 was cultured in RPMI-1640 (Gibco, 11875-093) with 10% fetal bovine serum (FBS; Sigma, F2442) supplemented with 1% penicillin/streptomycin (P/S; Gibco, 15070-063). HCT116 and HT29 were cultured in McCoy's 5a medium (Cytiva, SH30200.01) with 10% FBS and 1% P/S. All the rest of the cells were cultured in Dulbecco Modified Eagle Medium (DMEM; Gibco, 11965-092) with 10% FBS and 1% P/S. All the cells were cultured at 37℃ and 5% CO2. After thawing, cells were used for up to 10 passages and their authenticities were checked by short tandem repeat analysis. *Mycoplasma* testing was not done. Cell experiments were conducted and designed according to protocols approved by the Institutional Biosafety Committee of the University of Chicago.

Animal study:

The mouse study was approved by the Institutional Animal Care and Use Committee (IACUC) at the University of Chicago. Nude mice (athymic nu/nu, 4-6 weeks old, female, Harlan Laboratories, RRID: IMSR_JAX:002019) were subcutaneously injected with 1×10^6 melanoma cells in 30% Matrigel (Corning, 354234) in PBS on the flanks. Tumor growth was measured starting from 8 days after inoculation by measurement of two perpendicular diameters with calipers. Tumor volume was calculated using formula $4\pi/3 \times (\text{width}/2)^2 \times (\text{length}/2)$, and tumors were harvested from euthanized mice and weighed at experimental endpoints. Freshly excised mouse tumor tissues were minced into small pieces by scissors in HBSS, digested by Collagenase IV (1 mg/mL) and DNase I (200 U/mL) (EMD Millipore, 260913-10MU) in 5 ml HBSS (Gibco, 14025-092) at 37°C for 30 minutes with gentle rocking. The digestion reaction was quenched by 100 µl of 0.5M EDTA pH 8.0. The digested tumor tissues were then filtered into new tube through 70-µm nylon mesh strainer and centrifuged at 300×g for 10 minutes at room temperature, supernatant was discarded. Then, 10 ml Ammonium Chloride Solution (STEMCELL, 07850) was added, and tumor tissues were incubated at room temperature for 5 minutes to remove red blood cells. Reaction was quenched by FBS-containing media and washed 3 times. Next, isolated tumor cells were processed for protein collection, immunoblotting, and Ki-67 (BioLegend, 151208) flow cytometry.

The Cancer Genome Atlas (TCGA) analysis:

mRNA expression data from human skin cutaneous melanoma patient samples (TCGA, PanCancer Atlas) and human colorectal adenocarcinoma patient samples (TCGA, PanCancer Altas) were obtained from TCGA cBioPortal (https://www.cbioportal.org/), and mRNA

expression of z-scores relative to all samples (log RNA-seq V2 RSEM) was compared. Wild-type melanoma refers to melanoma samples expressing both wild-type *NRAS* and wild-type *BRAF*.

Transient expression in human immortalized Mel-ST melanocytes:

Mel-ST cells were seeded the day before transfection to around 70% confluence. 2.5 μg of WT *NRAS*, *NRAS Q61K*, and *BRAF V600E* expression vectors, or an empty expression vector were transiently introduced into Mel-ST cells by Lipofectamine 3000 reagent (Life Technologies, L3000015) following the manufacturer's instructions. Three to five days after transfection, transfected cells were collected for RNA or protein analysis.

RNA extraction and RT-PCR:

Total RNA was purified from cultured cells using TRIzol reagent (Ambion, 15596026), and 1 μg of cDNA was synthesized from total isolated RNA using iScript cDNA Synthesis Kit (Bio-Rad, 1708891) per manufacturer's instructions. qPCR analysis was performed using iTaq Universal SYBR Green Supermix (Bio-Rad, 1725121) with the following primers.

DDIT3 primers: R-CTTGTGACCTCTGCTGGTTCTG; F-GGTATGAGGACCTGCAAGAGGT.

AHCYL1 primers: F-GAAGCAGGCCAAGGAGATCG; R-GAGGACTGTGAGATCGAGCG.

GAPDH primers: F-GTCTCCTCTGACTTCAACAGCG; R-ACCACCCTGTTGCTGTAGCCAA.

ATF2 primers: F-GGTAGCGGATTGGTTAGGACTC; R-TGCTCTTCTCCGACGACCACTT.

ITPR3 primers: F-CTGTGAACTGCAACACCAGC; R-ACTCGTCACACGTCAGGAAC.

AHCYL2 primers: F-AGTCAAGAAGCAGATCCAGTTT; R-TATATGAAGCCGCTGAGCTGTA.

MAPK14 primers: F-CCAGCTTCAGCAGATTATGCG; R-CGCAAAGTTCATCTTCGGCA.

ATF4 primers: F-TTCTCCAGCGACAAGGCTAAGG; R-CTCCAACATCCAATCTGTCCCG.

ATF6 primers: F-CAGACAGTACCAACGCTTATGCC; R-GCAGAACTCCAGGTGCTTGAAG.

XBP1 primers: F-CTGCCAGAGATCGAAAGAAGGC; R-CTCCTGGTTCTCAACTACAAGGC.

PHGDH primers: F-CTGCGGAAAGTGCTCATCAGT; R-TGGCAGAGCGAACAATAAGGC.

SCD primers: F-TCTAGCTCCTATACCACCACCA; R-TCGTCTCCAACTTATCTCCTCC.

HMGCS1 primers: F-GATGTGGGAATTGTTGCCCTT; R-ATTGTCTCTGTTCCAACTTCCAG.

RIT1 primers: F-TTCATCAGCCACCGATTCCC R-GCAGGCTCATCATCAATACGGA.

BTG2 primers: F-GCAGAGGCTTAAGGTCTTCAGC; R-TGGTTGATGCGAATGCAGCGGT.

RRM2 primers: F-CACGGAGCCGAAAACTAAAGC; R-TCTGCCTTCTTATACATCTGCCA.

PFKL primers: F-AAGAAGTAGGCTGGCACGACGT; R-GCGGATGTTCTCCACAATGGAC.

TRIB3 primers: F-GCTTTGTCTTCGCTGACCGTGA; R-CTGAGTATCTCAGGTCCCACGT.

P4HA1 primers: F-GCCAAAGCTCTGTTACGTCTCC; R-CAAAGCAGTCCTCAGCCGTTAG.

GNL3 primers: F-GCCAGGTGAAGGTTCCAAGG; R-CAGCCTCTCGATTGGCATGAT.

HSP90AB1 primers: F-AGAAATTGCCCAACTCATGTCC; R-ATCAACTCCCGAAGGAAAATCTC

CCT7 primers: F-GCTGGTGTTGCATTCAAGAAG; R-TTGCCTGATAATCCTCAACTGTG.

DUT primers: F- GAAGCCGCGGTACTCTCC; R-TGAAATGGCGGGTGTCTCC.

TYMS primers: F-GGTGTTTTGGAGGAGTTGCTGTG; R-GGAGAATCCCAGGCTGTCCAAA.

PCNA primers: F- CAAGTAATGTCGATAAAGAGGAGG; R-GTGTCACCGTTGAAGAGAGTGG.

CDC45 primers: F-GGAGAACACACTCTCCGTGG; R- GGGAAGACCCATGTCTGCAA.

NOLC1 primers: F- GTAGCAGTGATGACTCAGAGGAG; R-CTGGAGGAATCCTCACTGCTAG.

NME1 primers: F-AAGGAGATCGGCTTGTGGTTT; R- CTGAGCACAGCTCGTGTAATC.

RRP9 primers: F-TGAGGCCCGTGCATTTGAG; R-CCCCGTAAAACGCGAATGTC.

WDR43 primers: F-CCTACTTCGCTTTGGCCTCTA; R-GAAGGCACGTACTCCTGGTG.

NPM1 primers: F- ACGGTCAGTTTAGGGGCTG; R-CTGTGGAACCTTGCTACCACC.

GRWD1 primers: F-AGTCCGGCGACACAAGTTC; R-CTCGGTGGTAGAGCACATAGG.

IPO4 primers: F-GCTCCAGATCGTTCTTCGGG; R-CCGTCAGGATCAGGGACTTG.

AIMP2 primers: F-GCCACGTGCAGGAAGAGT; R-CCAGCGCATTGGTGGTTAAA.

TCOF1 primers: F-AAGTCAGCCCACACGCTG; R-GCTTGCCATCTGGGTCATCT.

RABEPK primers: F-AGCTTCATTCCCTCCTGCAC; R-CAATGGCTGCCGATGATGTG.

Immunoblotting and antibodies:

For all western blot experiments, protein lysates were prepared using RIPA cell lysis buffer (Millipore Sigma, 20-188) supplemented with protease inhibitors (Millipore Sigma, 59813300) and incubated on ice for 30 minutes. Protein lysate was quantified using Pierce Rapid Gold BCA Protein Assay Kit (Thermo Fisher Scientific, A53225) and denatured with Laemmli SDS sample buffer (Thermo Fisher Scientific, J61337). Twenty to 30 μg of protein was loaded into wells of homemade SDS-PAGE gel along with molecular weight markers (Thermo Fisher Scientific, 26616). Gel was run at 110V for 1–2 hours. Resolved proteins were then transferred onto a nitrocellulose membrane by wet transfer. After transfer, membrane was blocked in TBST with 5% skimmed milk for 1 hour and probed with relevant primary and secondary antibodies in TBST with 5% skimmed milk. Quantification of western blot bands was carried out by subtracting the background from the band intensity using software ImageJ. The following primary antibodies were used: Rabbit monoclonal anti-GAPDH antibody (1:15,000 dilution, Cell Signaling Technology, 2118S, RRID: AB_561053), Mouse monoclonal anti-β-actin antibody (1:5000, Sigma-Aldrich, A1978, RRID: AB_476692), AHCYL1/SAHH-3 (D-7) antibody (1:1,000, Santa Cruz Biotechnology, sc271581, RRID: AB_10649944), ATF-2 Antibody (F2BR-1; 1:250, Santa Cruz Biotechnology, sc-242, RRID: AB_626708), Rabbit monoclonal anti-BRAF antibody (1:2,000, Cell Signaling Technology, 14814S, RRID: AB_2750887), NRAS Polyclonal antibody (1:2,000, Proteintech, 10724-1-AP, RRID: AB_2154209), ATF-4 (D4B8) Rabbit mAb (1:500, Cell Signaling Technology, 11815, RRID: AB_2616025), ATF-6 (D4Z8V) Rabbit mAb (1:500, Cell Signaling Technology, 65880, RRID: AB_2799696), CREB (48H2) Rabbit mAb (1:500, Cell Signaling Technology, 9197S, RRID: AB_331277), Phospho-CREB (Ser133; 87G3) Rabbit mAb (1:500, Cell Signaling Technology, 9198S, RRID: AB_2561044), Calnexin (C5C9)

Rabbit mAb (Cell Signaling Technology, 2679S, RRID: AB_2228381), IP3 Receptor 1 (D53A5) Rabbit mAb (Cell Signaling Technology, 8568S, RRID: AB_10890699), CHOP (L63F7) Mouse mAb (1:500, Cell signaling Technology, 2895, RRID: AB_2089254), pSTAT3 Tyr705 (1:1000, Cell Signaling Technology, 9131L, RRID: AB_331586), STAT3 (CST), GFP (1:1,000, Sigma, 11814460001, RRID:AB_390913). p65 (1:1,000, Cell Signaling Technology, 8242S, RRID:AB_331757), lamin A/C (1:1,000, Cell Signaling Technology, 4777, RRID:AB_10545756). The following secondary antibody was used: Goat anti-Mouse IgG (HþL) Secondary Antibody, HRP (1:5000 dilution, Thermo Fisher Scientific, 31430, RRID: AB_228307), Goat anti-Rabbit IgG (HþL) Secondary Antibody, HRP (1:5000 dilution, Thermo Fisher Scientific, 31460, RRID: AB_228341). HRP was detected by chemiluminescence by Clarity Western ECL Substrate (Bio-Rad, 1705061) by a film developer.

RNA interference

For RNA interference experiments, cells were seeded the day before to around 70% confluence and were transfected with 30 pmol targeting siRNAs or control siRNAs using Lipofectamine RNAiMAX Transfection Reagent (Life Technologies, 13778030) following manufacturer's instructions. For siAHCYL1 cell proliferation assay, 24 hours after transfection, 50,000 cells were re-seeded in 6-well plate. Cell number was recorded daily on automated cell counter (Bio-Rad, TC20) after mixing cell suspension with trypan blue (Sigma-Aldrich, T8154-100ML). Proteins and RNAs were collected for further analysis on day 4 or day 5. For siATF4 and siATF6 assay, 15 pmol of each siRNA was combined for transfection; for siXBP1 assay, 15 pmol of siXBP1 was transfected. 24h after transfection, transduction for *AHCYL1* knockout was

performed (detailed transduction procedure can be found in the transduction method section). After puromycin selection, 50,000 cells were re-seeded, and endpoint cell number was recorded.

Hs_AHCYL1_2 FlexiTube siRNA (called "siAHCYL1 #1" in the manuscript) (Qiagen, SI00090335); Hs_AHCYL1_3 FlexiTube siRNA (called "siAHCYL1 #2" in the manuscript) (Qiagen, SI00090342); Hs_ATF4_5 FlexiTube siRNA (Qiagen, SI03019345); Hs_ATF6_5 FlexiTube siRNA (Qiagen, SI03019205); XBP-1 siRNA (h): sc-38627 (SANTA CRUZ BIOTECHNOLOGY); Control siRNA (Qiagen, 1022076).

Construction of shRNA knockdown plasmids

All shRNAs were from Human pLKO.1 the RNAi consortium (TRC) Library (BROAD Institute/ Open Biosystems (https://www.broadinstitute.org/rnai-consortium/rnai-consortium-shrna-library). shRNA-mediated stable cell lines were generated following "Lentivirus production and transduction" as stated below. For shAHCYL1 and shAHCYL2 proliferation assay, 50,000 cells were seeded in 6-well plate and cell number was recorded daily. For shITPR3 assay, cells were seeded to around 70% confluence, transfected with siAHCYL1 for 24h and re-seeded and endpoint cell number was recorded.

Human shAHCYL1 #1: GCACTGATAGAACTCTATAAT.

Human shITPR3 #1: CGTGAAGAACAAGACCGACTA.

Human shAHCYL2 #1: GCTCTAGCAGAAAGTGGATTT.

Human shAHCYL2 #2: GCAGAGTTTGGACGAAGAGAA.

Construction of CRISPR-Cas9 knockout plasmids

All sgRNAs were designed by CRISPick (Broad Institute) and ordered from IDT. Guide RNAs were cloned into pLentiCRISPRv2 following Zhang Lab CRISPR cloning protocol (Shalem et al. 2014; Sanjana, Shalem, and Zhang 2014), and transformed and amplified using Stable Competent E. coli (High Efficiency) (NEB, C3040H). Successful cloning was confirmed by low throughput Sanger sequencing at UChicago DNA Sequencing Core.

Human sgAHCYL1 sg1: GATGTTTGGTGGGAAACAAG.

Human sgAHCYL1 sg2: AGATGTTACAAGCAGACCAG.

Human sgATF2 sg1: GCTCGTTCGACCAGTCACCA.

Human sgATF2 sg2: GGACGAACAATAGCTGATGT.

NTC (Doench et al. 2016) (non-targeting control) oligo: GTAGGCGCGCCGCTCTCTAC.

LentiCRISPR v2 plasmid was a gift from Feng Zhang (Addgene plasmid # 52961; http://n2t.net/addgene: 52961; RRID: Addgene_52961) (Sanjana, Shalem, and Zhang 2014).

Construction of CRISPR/Cas9-resistant wild-type AHCYL1 expression plasmid

CRISPR-Cas9-resistant WT AHCYL1 was generated by mutating Human sgAHCYL1 sg1 targeting sequence from GATGTTTGGTGGGAAACAAG into GATGTTcGGcGGcAAgCAgG. After Sanger sequencing validation, expression plasmid was cloned into pENTR-TOPO backbone using pENTER/D-TOPO Cloning Kit (Invitrogen, 45-021-8) following manufacturer's instructions. pENTR-WT-AHCYL1 was cloned into pLenti CMV Blast DEST backbone by Gateway LR Clonase II Enzyme Mix (Invitrogen, 11791020), and amplified using 5-alpha Competent E. coli (High Efficiency) (NEB, C2987H).

pLenti CMV Blast DEST (706-1) was a gift from Eric Campeau & Paul Kaufman (Addgene plasmid # 17451; http://n2t.net/addgene:17451; RRID:Addgene_17451).

Complete DNA sequence of CRISPR-resistant human AHCYL1:

ATGTCGATGCCTGACGCGATGCCGCTGCCCGGGGTCGGGGAGGAGCTGAAGCAGGC
CAAGGAGATCGAGGACGCCGAGAAGTACTCCTTCATGGCCACCGTCACCAAGGCGC
CCAAGAAGCAAATCCAGTTTGCTGATGACATGCAGGAGTTCACCAAATTCCCCACC
AAAACTGGCCGAAGATCTTTGTCTCGCTCGATCTCACAGTCCTCCACTGACAGCTAC
AGTTCAGCTGCATCCTACACAGATAGCTCTGATGATGAGGTTTCTCCCCGAGAGAAG
CAGCAAACCAACTCCAAGGGCAGCAGCAATTTCTGTGTGAAGAACATCAAGCAGGC
AGAATTTGGACGCCGGGAGATTGAGATTGCAGAGCAAGACATGTCTGCTCTGATTTC
ACTCAGGAAACGTGCTCAGGGGGAGAAGCCCTTGGCTGGTGCTAAAATAGTGGGCT
GTACACACATCACAGCCCAGACAGCGGTGTTGATTGAGACACTCTGTGCCCTGGGG
GCTCAGTGCCGCTGGTCTGCTTGTAACATCTACTCAACTCAGAATGAAGTAGCTGCA
GCACTGGCTGAGGCTGGAGTTGCAGTGTTCGCTTGGAAGGGCGAGTCAGAAGATGA
CTTCTGGTGGTGTATTGACCGCTGTGTGAACATGGATGGGTGGCAGGCCAACATGAT
CCTGGATGATGGGGGAGACTTAACCCACTGGGTTTATAAGAAGTATCCAAACGTGTT
TAAGAAGATCCGAGGCATTGTGGAAGAGAGCGTGACTGGTGTTCACAGGCTGTATC
AGCTCTCCAAAGCTGGGAAGCTCTGTGTTCCGGCCATGAACGTCAATGATTCTGTTA
CCAAACAGAAGTTTGATAACTTGTACTGCTGCCGAGAATCCATTTTGGATGGCCTGA
AGAGGACCACAGATGTGATGTTcGGcGGcAAgCAgGTGGTGGTGTGTGGCTATGGTGA
GGTAGGCAAGGGCTGCTGTGCTGCTCTCAAAGCTCTTGGAGCAATTGTCTACATTAC
CGAAATCGACCCCATCTGTGCTCTGCAGGCCTGCATGGATGGGTTCAGGGTGGTAAA
GCTAAATGAAGTCATCCGGCAAGTCGATGTCGTAATAACTTGCACAGGAAATAAGA

ATGTAGTGACACGGGAGCACTTGGATCGCATGAAAAACAGTTGTATCGTATGCAAT
ATGGGCCACTCCAACACAGAAATCGATGTGACCAGCCTCCGCACTCCGGAGCTGAC
GTGGGAGCGAGTACGTTCTCAGGTGGACCATGTCATCTGGCCAGATGGCAAACGAG
TTGTCCTCCTGGCAGAGGGTCGTCTACTCAATTTGAGCTGCTCCACAGTTCCCACCTT
TGTTCTGTCCATCACAGCCACAACACAGGCTTTGGCACTGATAGAACTCTATAATGC
ACCCGAGGGGCGATACAAGCAGGATGTGTACTTGCTTCCTAAGAAAATGGATGAAT
ACGTTGCCAGCTTGCATCTGCCATCATTTGATGCCCACCTTACAGAGCTGACAGATG
ACCAAGCAAAATATCTGGGACTCAACAAAAATGGGCCATTCAAACCTAATTATTAC
AGATACTAA

Lentivirus production, transduction, and cell proliferation assay:

293T cells were seeded the day before virus production and reached 70% confluency for transfection. Lentiviruses were packaged by cotransfecting psPAX2, pMD2.G, and expression plasmids into HEK293T cells using TransIT-LT1 Transfection Reagent (Mirus, MIR 2305). After 18 hours, culture media were changed with virus harvesting media (DMEM with 10% FBS plus 1% BSA), and viruses were collected after 48 hours of transfection. Harvested viruses were filtered through a 0.45 μm filter and used for cell transduction. HMCB cells were transduced with 4 μg/mL polybrene (American Bioanalytical, AB01643-00001), and all other cell lines were transduced with 8 μg/mL polybrene. Transduced cells were selected with 2 μg/mL puromycin (Sigma-Aldrich, P8833) for 48 hours for stable cell lines. Single-cell clones were obtained by serial dilution method from HMCB sgAHCYL1 #1. After resistance selection, 50,000 cells were re-seeded in a 6-well plate for cell proliferation assay on day 0. Meanwhile, chemicals were added: ISRIB (a generous gift from the Elf Lab), 4-Phenylbutyric acid (Sigma-Aldrich, P21005),

TUDCA (Millipore, 580549). Cell number was recorded daily on the automated cell counter (Bio-Rad, TC20) after mixing cell suspension with trypan blue (Sigma-Aldrich, T8154-100ML). Proteins or RNAs were collected for further analysis on day 4 or day 5.

psPAX2 was a gift from Didier Trono (Addgene plasmid # 12260; http://n2t.net/addgene:12260; RRID:Addgene_12260); pMD2.G was a gift from Didier Trono (Addgene plasmid # 12259; http://n2t.net/addgene:12259; RRID:Addgene_12259).

ER isolation

ER and post-mitochondria fraction (PMF) were isolated using an Endoplasmic Reticulum Isolation Kit (Sigma-Aldrich, ER0100) following the manufacturer's instructions. PMF refers to the cytosol after removing the ER, mitochondria, and nucleus. Isolated fractions were lysed by RIPA cell lysis buffer (Millipore Sigma, 20-188) supplemented with protease inhibitors (Millipore Sigma, 59813300) and followed protein extraction steps as stated in "Immunoblotting and antibodies" section. Successful ER isolation was confirmed by calnexin expression, and successful PMF isolation was confirmed by β-actin expression.

ER calcium detection

Cells were seeded 24 hours in advance to around 70% confluence in 35 mm imaging dishes (Cellvis, D35-20-1.5-N) and transfected with 0.8 μg of pCMV R-CEPIA1er plasmid using Lipofectamine 3000 reagent (Life Technologies, L3000015) and Opti-MEM (Gibco, 31985-070) the next day. 24 hours later, media were changed, and cells were proceeded for analysis by either imaging or flow cytometry. For imaging, fluorescence was imaged under 562nm/641nm using Olympus "live cell" DSU Spinning Disk Confocal at UChicago Integrated Light Microscopy

Core. Images and fluorescence intensity were analyzed using ImageJ. For flow cytometry, fluorescence was analyzed on LSR-Fortessa 4-15 flow cytometer or LSRII 4-12 at the UChicago Cytometry and Antibody Technology Core Facility, and data were analyzed using FlowJo v10.4.

pCMV R-CEPIA1er was a gift from Masamitsu Iino (Addgene plasmid # 58216; http://n2t.net/addgene:58216; RRID: Addgene_58216).

XBP1 splicing assay

Total RNA was extracted from samples and reverse transcribed as described above. *XBP1* cDNA was PCR amplified with primers: F-AGGAAACTGAAAAACAGAGTAGCAGC; R-TCCTTCTGGGTAGACCTCTGG. Amplified cDNA was split into half: half was kept for "Uncut *XBP1*" control, half was digested using Pst1-HF (BioLabs, R3140L) enzyme. Samples were loaded with Gel loading dye (BioLabs, B7025S) and run on a DNA gel along with DNA ladder (BioLabs, N3232S). Spliced *XBP1* ratio was calculated by dividing spliced *XBP1* (1S) by total *XBP1* band intensity. *XBP1* band intensity was quantified using ImageJ using "Gels" function.

Apoptosis assay

Cell apoptosis was analyzed using Annexin V (BD, 556547) and PI staining (Thermo Fisher, BMS500PI) following the manufacturer's instructions. Data were collected on LSR-Fortessa 4-15 flow cytometer or LSRII 4-12 at the UChicago Cytometry and Antibody Technology Core Facility and analyzed using FlowJo v10.4.

Cell-cycle analysis

One million cells were collected for each group, washed with PBS, and fixed dropwise with 70% cold ethanol with gentle vortexing. Cells were fixed on ice for 1 hour and washed with cold PBS. 0.5 mg/ml Rnase A was added and incubated at 37 degrees for 1 hour. Cells were stained with 10 μg/ml PI solution (ThermoFisher, BMS500PI) and analyzed by flow cytometry at 488 nm.

RNA-sequencing and analysis:

Sample triplicates were collected and followed by RNA extraction using the PureLink RNA Mini Kit (12183018A, Invitrogen) per the manufacturer's instructions. At least 500 ng of extracted RNA per sample was sent to Novogene for sequencing and bioinformatics analysis. RNA sequencing was performed via Illumina Next-Generation Sequencing. Fragments were aligned with HISAT2 to reference genes, and differential gene-expression analysis was performed by DESeq.

Transcription factor scan

Transcription factor scan was performed using "gene-regulation.com" (http://gene-regulation.com/pub/programs.html), with program "Match - 1.0 Public". Potential transcription factors that recognize AHCYL1 promoter region were identified.

Statistical analysis

Statistical analysis for all experimental data is included in the figure legends, with sample size and type of analysis indicated. P values less than or equal to 0.05 is considered as significant: ns, not significant; *, $P \leq 0.05$; **, $P \leq 0.01$; ***, $P \leq 0.001$.

2.3 Results

AHCYL1 is selectively highly expressed in mutant *NRAS* but not mutant *BRAF* expressing human melanoma.

We previously conducted loss-of-function RNAi screens to identify oncogene-specific metabolic requirements (Kang et al. 2015; Gao et al. 2022), which reveals that AHCYL1 is among the top candidates that are critical for cell proliferation of mutant *NRAS* expressing human melanoma cells, but not for mutant *BRAF* or *WT* expressing human melanoma cells (Fig. S2.1A). Intriguingly, we found that *AHCYL1* mRNA level correlates with *NRAS* mutational status in human skin cutaneous melanoma from the cancer genome atlas (TCGA) analysis (Fig. 2.1A), and we confirmed the selective upregulation of *AHCYL1* mRNA levels (Fig. 2.1B) and protein expression (Fig. 2.1C) in diverse human melanoma cells harboring mutated *NRAS* compared to cells harboring mutated *BRAF*. To further explore the causative connection between *NRAS* mutational status and AHCYL1 expression, we transiently introduced *WT NRAS*, *NRAS Q61K*, *BRAF V600E*, or an empty expression vector into human immortalized Mel-ST melanocytes. We found that, only introducing *NRAS Q61K* results in increased protein and mRNA levels of *AHCYL1* in Mel-ST cells (Fig. 2.1D), suggesting *NRAS* dependent AHCYL1 regulation. Collectively, these results demonstrate that AHCYL1 is selectively upregulated in mutant *NRAS* but not mutant *BRAF* expressing human melanoma, implying AHCYL1 selective criticalness.

AHCYL1 is selectively critical for cell proliferation and tumor growth of *NRAS*-mutated human melanoma.

Next, we sought to investigate whether AHCYL1 selective upregulation in *NRAS*-mutated human melanoma (Fig. 2.1) corresponds with selective requirement of AHCYL1. First, we

knocked down *AHCYL1* using siRNA, and *AHCYL1* deficiency results in selective proliferation attenuation in HMCB cells expressing mutant *NRAS* but not A375 cells expressing mutant *BRAF* (Fig. 2.2A, 2.2B; knockdown efficiency shown in Fig. 2.2C). In addition, we examined three other human melanoma cell lines, VMM39 and SK-MEL-2 that express mutant *NRAS*, and SK5 that expresses mutant *BRAF*. Consistent with these results, *AHCYL1* knockdown by siRNA selectively attenuates the cell proliferation of VMM39 and SK-MEL-2 but not SK5 (Fig. S2.1B-S2.1E).

In addition, shRNA mediated *AHCYL1* knockdown results in attenuated cell proliferation in HMCB (*NRAS Q61K,* Fig. 2.2D), but not in A375 cells (*BRAF V600E*, Fig. 2.2E, 2.2F), confirming selective AHCYL1 requirement in *NRAS*-mutated melanoma cells. Then, we inoculated the HMCB and A375 shAHCYL1 cells into nude mice for xenograft implantation. Consistent with our *in vitro* findings, *AHCYL1* knockdown significantly decreases the tumor growth potential in HMCB shAHCYL1 cells implanted mice (Fig. 2.2G), while no significant changes were observed in A375 shAHCYL1 cells implanted mice (Fig. 2.2H). All these show that AHCYL1 is selectively critical for both the cell proliferation and tumor growth potential of *NRAS*-mutated human melanoma.

To further validate, we conducted CRISPR-Cas9 mediated *AHCYL1* knockout. Consistent with previous findings, HMCB cells (*NRAS Q61K*) show decreased cell proliferation, whereas no significant differences of cell proliferation in A375 cells (*BRAF V600E*) (Fig. 2.2I-2.2K). In addition, we obtained single cell clones from HMCB *AHCYL1* knockout polyclonal cells (Fig. S2.1F) and introduced either WT *AHCYL1* expression vector or control vector back into the single cell clone to a comparable AHCYL1 protein level as in parental HMCB cells (Fig. 2.2L, 2.2M). Introducing AHCYL1 back rescues the growth defect caused by AHCYL1

deficiency, further demonstrating that the growth defect is from AHCYL1 deficiency itself and suggesting no off-target effects from *AHCYL1* sgRNAs (Fig. 2.2L). Then, we injected the HMCB *AHCYL1* knockout and rescue cell line into nude mice, and both the tumor growth potential and Ki-67 expression decrease with *AHCYL1* knockout cells implantation comparing to rescue or control HMCB cell implanted mice (Fig. S2.1G). Moreover, we injected A375 *AHCYL1* knockout cells into nude mice, and there are no significant differences in tumor growth potential or Ki-67 expression comparing to control A375 cells (Fig. S2.1H). We also analyzed the cell cycle before and after *AHCYL1* knockout. Results show that, after *AHCYL1* knockout, HMCB cells exhibit cell cycle arrest at G0/G1 phase (Fig. S2.2A), while no significant change in A375 cells (Fig. S2.2B). These results together suggest that AHCYL1 is selectively critical for both the cell proliferation and the tumor growth potential of *NRAS*-mutated human melanoma.

Both AHCYL1 and AHCYL2 are AHCY-like proteins that share similar protein sequence (Devogelaere, Sammels, and De Smedt 2008). Thus, we investigated the role of AHCYL2 in oncogene-specific metabolic regulations. Based on TCGA analysis, *AHCYL2* mRNA is not upregulated in human *NRAS*-mutated skin cutaneous melanoma (Fig. S2.3A). Additionally, *AHCYL2* mRNA levels are significantly lower than *AHCYL1* mRNA levels in both HMCB cells (Fig. S2.3B) and A375 cells (Fig. S2.3C), with around 50 and 30 times less expression, respectively. This implies much less AHCYL2 expression in human melanoma cells compared to AHCYL1. To examine AHCYL2 requirement, we conducted shRNA-mediated knockdown of *AHCYL2*, and the results show that AHCYL2 it's not critical for HMCB cell proliferation (Fig. S2.3D). Mechanistically, even though sharing similar protein sequences, AHCYL2 cannot bind to IP3R as AHCYL1, due to its extra non-structural proline/alanine tail (Ando, Kawaai, and Mikoshiba 2014; Ando, Mizutani, and Mikoshiba 2009). In conclusion,

AHCYL2 is expressed at much lower levels than *AHCYL1* in human melanoma cells, and not required for cell proliferation in *NRAS*-mutated melanoma.

AHCYL1 is selectively critical for cell proliferation of *KRAS*-mutated human colorectal cancer cells, but not for human colorectal cancer cells expressing mutant *BRAF*.

To explore whether AHCYL1 is critical for other *RAS* mutated cancers, we examined two human colorectal cancer cell lines, HCT116 expressing mutant *KRAS G13D* and HT29 expressing mutant *BRAF V600E*. First, we knocked down *AHCYL1* using shRNA, and AHCYL1 deficiency results in selective growth attenuation in HCT116 cells (*KRAS G13D*) but not HT29 cells (*BRAF V600E*) (Fig. S2.4A-S2.4C). Consistent with the shRNA results, siRNA mediated *AHCYL1* knockdown also causes selective growth attenuation in HCT116 cells but not in HT29 cells (Fig. S2.4D-S2.4F). Thus, these results together suggest that AHCYL1 is selectively critical for *KRAS*-mutated human colorectal cancer cell HCT116 proliferation. However, TCGA data analysis reveals that *KRAS* mutational status does not correlate with *AHCYL1* (Fig. S2.4G) mRNA levels in human colorectal adenocarcinoma patient samples, suggesting that *KRAS* mutants might achieve AHCYL1 reliance through different mechanisms compared to cancer cells expressing *NRAS* mutants.

AHCYL1 deficiency causes ER calcium decrease in *NRAS* mutant-expressing melanoma cells.

AHCYL1 has been reported to bind to and suppress the IP3R, an ER calcium channel protein, and such binding prevents IP3 induced ER calcium release (Ando et al. 2006; Devogelaere et al. 2006). Thus, we examined the calcium levels in the ER before and after AHCYL1 deficiency.

First, we generated HMCB (*NRAS Q61K*) and A375 (*BRAF V600E*) cells with stable IP3R knockdown, isolated the ER proportion and the post-mitochondria fraction (PMF) (the cytosol after removing the nucleus, mitochondria, and the ER), and measured AHCYL1 protein level. Results show that AHCYL1 recruitment and localization on the ER decrease after IP3R (*ITPR3*) knockdown (Fig. 2.3A, S2.5A). We validated that IP3R deficiency doesn't change AHCYL1 protein level in the whole cell lysates from HMCB and A375 cells (Fig S2.5B). Interestingly, the proportion of AHCYL1 localizing on the ER comparing to in the cytosol is also higher in HMCB (*NRAS Q61K*) than in A375 (*BRAF V600E*) (Fig. 2.3B), suggesting higher binding affinity of AHCYL1 to the ER in HMCB cells. Next, we examined ER calcium levels using an ER specific calcium sensor, and found that in HMCB cells expressing mutated *NRAS*, stable knockdown of *AHCYL1* leads to a significant decrease in ER calcium levels, while no significant change was observed in A375 cells expressing mutated *BRAF* (Fig. 2.3C, 2.3D). To further confirm, we measured ER calcium levels in *AHCYL1* knockout HMCB cells, where we put back either WT *AHCYL1* expression vector ("Rescue") or control vector ("AHCYL1 KO") (Fig. 2.2L, 2.2M) and found that putting back WT AHCYL1 rescues the ER calcium decrease resulting from AHCYL1 deficiency (Fig. 2.3E). These results show that, AHCYL1 deficiency selectively leads to ER calcium decrease in HMCB cells expressing mutant *NRAS*. Moreover, we found that in HMCB cells with stable *IP3R* knockdown, AHCYL1 deficiency by siRNA no longer affects the endpoint cell number (Fig. 2.3F). The knockdown efficiency of *AHCYL1* (Fig. 2.3G) and *IP3R* (Fig. 2.3H) mRNA and protein (Fig. 2.3I) are confirmed. This demonstrates that the cell growth attenuation caused by *AHCYL1* deficiency is through the IP3R.

Taken together, our results reveal that AHCYL1 deficiency selectively causes a decrease in ER calcium levels in *NRAS*-mutated human melanoma cells.

AHCYL1 deficiency in *NRAS* mutant-expressing melanoma cells activates the UPR and triggers subsequent cell apoptosis.

Since ER calcium homeostasis is critical for calcium-dependent chaperons function as well as for protein folding, we investigated whether the observed ER calcium decrease from AHCYL1 deficiency (Fig. 2.3) causes ER stress (Hetz, Zhang, and Kaufman 2020). Cells sense and respond to ER stress by activating the UPR (Sehgal et al. 2017; Preissler et al. 2020; Ibarra et al. 2022; Krebs, Agellon, and Michalak 2015; Luo and Lee 2013; Bahar, Kim, and Yoon 2016), so we examined all three branches of the UPR after AHCYL1 deficiency in both HMCB and A375 cells, including ATF6 cleavage (Fig. 2.4A, 2.4B), ATF4 expression (Fig. 2.4C, 2.4D), and *XBP1* splicing (Fig. 2.4E). All three branches of the UPR are selectively upregulated after AHCYL1 deficiency mediated by sgRNA (Fig. 2.4A, 2.4D) and by shRNA (Fig. 2.4B, 2.4C and 2.4E) in HMCB cells (*NRAS Q61K*) but not in A375 cells (*BRAF V600E*). This demonstrates the presence of the ER stress. We further confirmed the critical role of the UPR by knocking down *ATF4*, *ATF6*, or *XBP1*. Results show that, knocking down *ATF4*, *ATF6*, or *XBP1* by siRNA abolishes the AHCYL1 dependency on HMCB cell proliferation (Fig. 2.4F-2.4K), indicating that the requirement of AHCYL1 is dependent on the UPR. These data together demonstrate that, *AHCYL1* knockdown causes ER stress and activates the UPR.

Sustained UPR activation can trigger cell apoptosis (Sano and Reed 2013). Indeed, we found that CHOP (*DDIT3*), the transcription factor that plays an important role in UPR-induced apoptosis (Sano and Reed 2013), is significantly upregulated after *AHCYL1* knockout in HMCB cells (Fig. 2.5A, 2.5B, S2.6A, S2.6B). This is consistent with Annexin V and PI cell apoptosis analysis (Fig. 2.5C-2.5E, S2.6C) which shows that the level of apoptosis significantly increases

after AHCYL1 deficiency in HMCB cells expressing mutant *NRAS*. The activation of apoptosis in HMCB cells is also confirmed by the increase of cytochrome C in the cytosol and decrease in the mitochondria after *AHCYL1* knockdown (Fig. S2.6D).

Next, we asked whether apoptosis can be alleviated by reducing the ER stress. To this end, we used ISRIB, a potent integrated stress response (ISR) inhibitor that reverses the effect from eIF2a phosphorylation (Zyryanova et al. 2018; Sidrauski et al. 2015, 2013; Costa-Mattioli and Walter 2020), and found that both the cell apoptosis level (Fig. 2.5F-2.5H) and the endpoint cell number (Fig. 2.5I) are significantly alleviated in HMCB cells (*NRAS Q61K*) with AHCYL1 deficiency. We further validated these findings using two other chemical chaperons, Tauroursodeoxycholic acid (TUDCA) (Grandjean and Wiseman 2020) and 4-Phenylbutyric acid (4-PBA) (Zeng et al. 2017; Grandjean and Wiseman 2020), both of which have been previously reported to reduce the ER stress. We show that both TUDCA (Fig. 2.5J) and 4-PBA (Fig. 2.5K) chaperons significantly relieve the endpoint cell number in AHCYL1-deficient HMCB cells. These results demonstrate that apoptosis caused by AHCYL1 deficiency is from the ER stress.

Furthermore, we validated our key findings in three more human *NRAS* mutation harboring melanoma cell lines, VMM39 (*NRAS Q61K, Q61R*), Hs 936.T (*NRAS Q61K*), and SK-MEL-147 (*NRAS Q61K*). Results show that, shRNA mediated *AHCYL1* knockdown results in reduced cell proliferation and ER calcium levels with elevated ATF4 and CHOP protein levels (Fig. S2.7).

Collectively, these results demonstrate that, AHCYL1 deficiency causes ER stress that activates the UPR and triggers downstream apoptosis.

AHCYL1 deficiency causes cell growth attenuation, ER calcium decrease, and apoptosis in *NRAS-Q61K* overexpressed Mel-ST cells.

To further confirm, we overexpressed *NRAS Q61K* in human immortalized melanocytes Mel-ST (Fig. 2.1C), and checked cell proliferation, ER calcium, and cell death before and after siRNA mediated *AHCYL1* knockdown (Fig. S2.8). Results show that, AHCYL1 deficiency reduces cell proliferation (Fig. S2.8A, S2.8B), ER calcium level (Fig. S2.8C), while increases cell death and *DDIT3* (CHOP) levels (Fig. S2.8D-F), in *NRAS Q61K* overexpressed Mel-ST cells, but not in Mel-ST cells with control vector overexpression. This indicates that AHCYL1 selective requirement for cell proliferation, ER calcium level, and cell death is *NRAS* mutation dependent.

RNA-Seq analysis shows downregulation of gene sets related to cell proliferation in *NRAS*-mutated human melanoma cells HMCB after *AHCYL1* knockdown.

We next performed RNA-Seq analysis on HMCB human melanoma cells expressing mutated *NRAS*, before and after siRNA-mediated *AHCYL1* knockdown. Principal component analysis (PCA) shows that *AHCYL1* knockdown samples separated from control samples (Fig. 2.6A). Volcano plot analysis summarizes genes that are downregulated or upregulated after *AHCYL1* knockdown (Fig. 2.6B) with confirmed *AHCYL1* knockdown efficiency (Fig. 2.6C). To gain further insight, we performed gene set enrichment analysis (GSEA) on hallmark gene sets and summarized the gene sets that are significantly downregulated in *AHCYL1* knockdown samples (Fig. 2.6D). Data reveals that *AHCYL1* knockdown downregulates gene sets related to cell proliferation, and detailed GSEA plots are presented, including Hallmark_MYC_Targets_V1, Hallmark_MYC_Targets_V2, Hallmark_MTORC1_Signaling (Fig. 2.6E-2.6G). There were no significantly upregulated gene sets. To validate our RNA-Seq results, we performed RT-qPCR

and tested representative genes that have been reported to be critical for cell proliferation and survival regulation in HMCB cells in the Hallmark_MYC_Targets_V1 (Fig. S2.9A), Hallmark_MYC_Targets_V2 (Fig. S2.9B), and Hallmark_MTORC1_Signaling gene sets (Fig. S2.9C). We have also tested these genes in A375 cells (Fig. S2.9D-S2.9F). Our results show that knockdown of *AHCYL1* downregulates gene sets related to cell proliferation in *NRAS*-mutated human melanoma cells HMCB.

AHCYL1 transcription in *NRAS*-mutated melanoma cells is regulated by transcription factor ATF2.

Next, we sought to explore the selective AHCYL1 upregulation in *NRAS*-mutated human melanoma (Fig. 2.1). To answer this question, we investigated *AHCYL1* transcription factors (TFs). We used an online tool (gene-regulation.com) that screens for TFs based on their reported binding response elements that can match *AHCYL1* promoter region sequence (Supplemental Table 1). From core and matrix match score, CREB and CRE-BP1 (ATF2) were identified and further validated. We found that treatment with a small molecule CREB inhibitor, 666-15 (Xie et al. 2015), resulted in dose-dependent increase in *AHCYL1* mRNA levels in HMCB cells but not in A375 cells (Fig. S2.10A, S2.10B), indicating CREB doesn't positively regulate *AHCYL1* transcription. Moreover, we checked CREB phosphorylation and found that CREB is more phosphorylated in A375 than HMCB cells (Fig. S2.10C), indicating higher CREB activity in A375 cells, which also implies that *AHCYL1* is not positively regulated by CREB. Thus, these results together suggest that CREB is not a positive regulator of *AHCYL1* transcription.

Next, we examined activating transcription factor 2 (ATF2), and found that based on TCGA analysis, *ATF2* mRNA level is significantly higher in *NRAS*-mutant expressing

human melanoma comparing to *WT* expressing human melanoma (Fig. 2.7A). In addition, both the ATF2 mRNA level (Fig. 2.7B) and protein level (Fig. 2.7C) are significantly upregulated in *NRAS*-mutated HMCB cells than in *BRAF*-mutated A375 cells, which is consistent with AHCYL1 selective upregulation (Fig. 2.1). To further validate, we found that exogenous over expression of *NRAS Q61K*, but not *BRAF V600E*, increases *ATF2* mRNA levels in immortalized skin melanocytes Mel-ST (Fig. 2.7D), suggesting *NRAS* mutant dependent *ATF2* transcription. Then, to check whether ATF2 regulates *AHCYL1* transcription, we knocked out *ATF2* by CRISPR-Cas9 in both HMCB and A375 cells and found that only in HMCB cells (*NRAS Q61K*), *ATF2* deficiency downregulates *AHCYL1* transcription (Fig. 2.7E, 2.7F), indicating *AHCYL1* is selectively regulated by ATF2 in HMCB cells. Whereas in both A375 and HMCB, ATF2 deficiency causes cell growth attenuation (Fig. 2.7E, 2.7F), consistent with previous report that ATF2 is required for mouse skin tumor growth and progression (Papassava et al. 2004). Together, we show that ATF2 selectively positively regulates *AHCYL1* transcription in *NRAS* mutant expressing human melanoma cells (Fig. 2.7G). We also found there is positive correlation between *ATF2* and *AHCYL1* mRNA levels in both *NRAS* or *BRAF* mutation harboring human cutaneous melanoma patients based on TCGA analysis, while *ATF2* and *AHCYL1* levels are in general lower in *BRAF* mutant expressing patients (Fig. S2.11). Since we showed that ATF2 only regulates *AHCYL1* mRNA in HMCB cells expressing mutant *NRAS* (Fig. 2.7), these observations suggest that ATF2 might also be commonly crucial for cell proliferation of *BRAF* mutant-expressing melanoma cells, which, however, is mediated through different mechanisms other than the regulation of *AHCYL1*.

We next sought to explore the upstream of ATF2 and the mechanism of the selective ATF2 upregulation in HMCB cells. Previous studies have shown that ATF2 can be activated by

stress kinases JNK and p38 (Lopez-Bergami, Lau, and Ronai 2010; Fritz et al. 2021; Lau and Ronai 2012; Wan et al. 2020), and that ATF2 is a reported downstream target of MAPK14 (Wan et al. 2020; Fritz et al. 2021) (p38α). To explore this, we knocked down *MAPK14* in HMCB and A375 cells and found that *AHCYL1* transcription significantly decreases in HMCB cells, while no significant changes of *AHCYL1* levels were observed in A375 cells (Fig. S2.12A, S2.12B). Knockdown of *MAPK14* affects cell proliferation in both HMCB and A375 cells (Fig. S2.12C, S2.12D). These results together suggest that *AHCYL1* transcription is selectively regulated by MAPK14 in HMCB cells.

These data together suggest that ATF2 and MAPK14 contribute to *AHCYL1* transcription in *NRAS* mutant expressing human melanoma cells, but not in human melanoma cells expressing *BRAF V600E*.

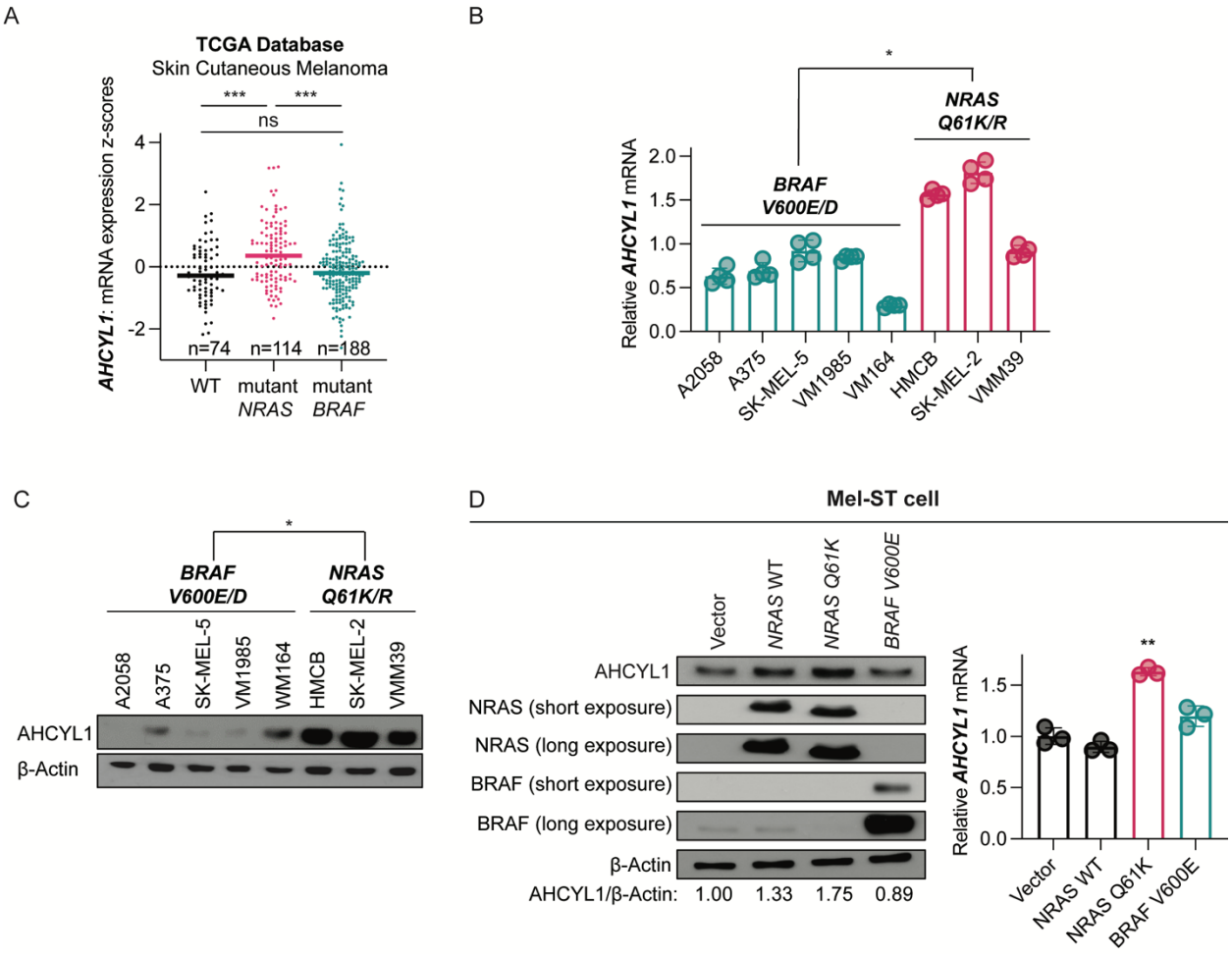

Figure 2.1

AHCYL1 is selectively highly expressed in *NRAS*-mutant but not *BRAF*-mutant expressing human melanoma. A, TCGA database analysis of *AHCYL1* mRNA levels in human skin cutaneous melanoma samples expressing mutated *NRAS*, mutated *BRAF*, or WT. Highlighted lines indicate data set median. B, *AHCYL1* relative mRNA expression in human melanoma cell lines expressing mutated *NRAS* or mutated *BRAF* by RT-qPCR. C, AHCYL1 protein expression in human melanoma cell lines expressing mutated *NRAS* or mutated *BRAF* by immunoblotting. D, AHCYL1 protein expression by immunoblotting (left) and relative *AHCYL1* mRNA expression by RT-qPCR (right) in human immortal melanocytes Mel-ST, exogenously

(continued)

expressed with mutated *NRAS*, mutated *BRAF*, WT, or empty vector. Error bars indicate means $\pm$ SD ($n \geq 3$). P values were calculated using two-tailed, unpaired Student t test (ns, not significant; *, $P \leq 0.05$; **, $P \leq 0.01$; ***, $P \leq 0.001$). All the data in this figure is generated by Dr. Rong Wu.

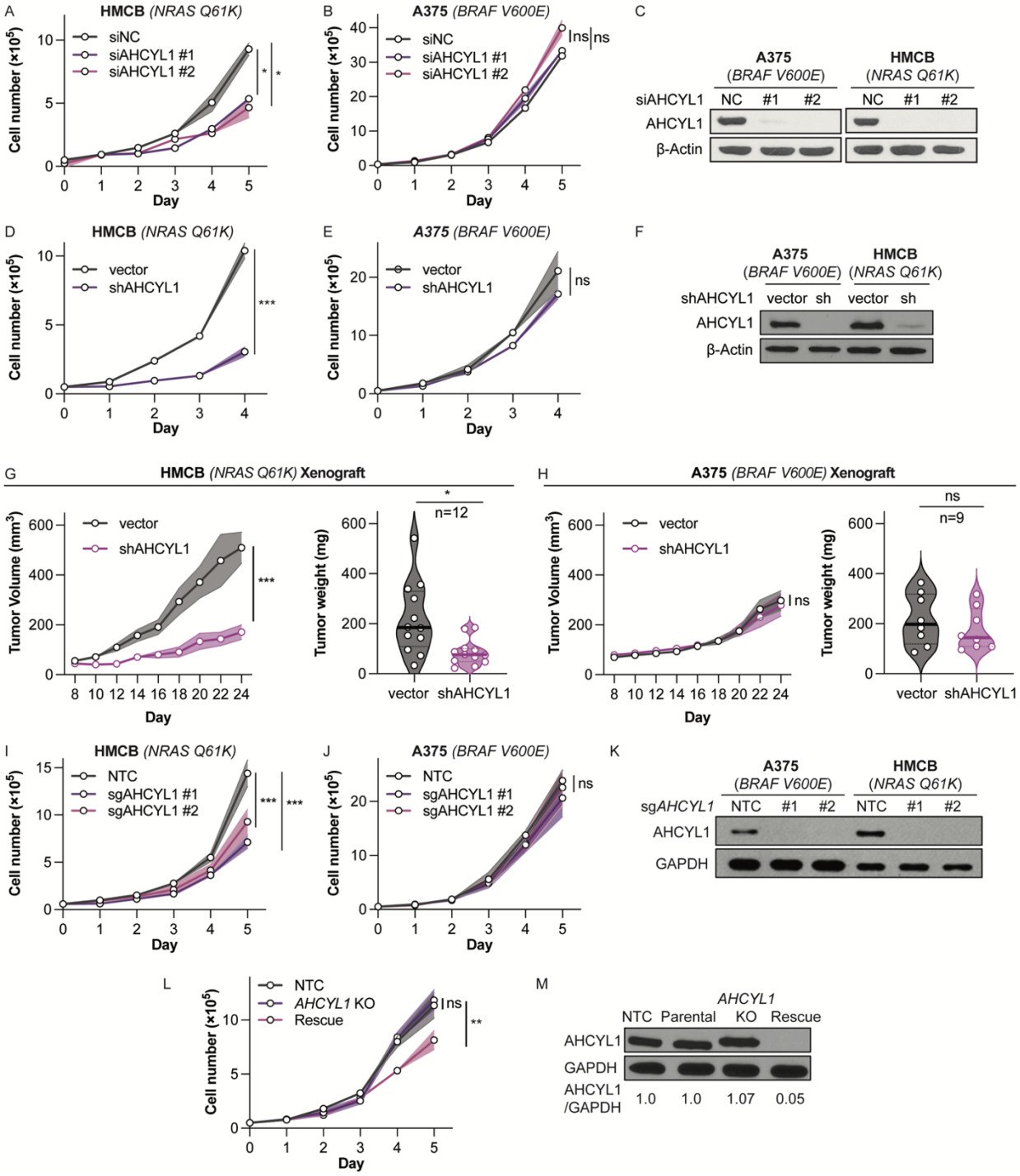

Figure 2.2

AHCYL1 is selectively critical for cell proliferation and tumor growth of *NRAS*-mutated human melanoma, but not for human melanoma expressing mutant *BRAF*. Cell proliferation

(continued)

of human melanoma cells expressing (A) *NRAS* mutation or (B) *BRAF* mutation after siRNA mediated *AHCYL1* knockdown. C, AHCYL1 protein expression after knockdown checked by immunoblotting. Cell proliferation of human melanoma cells expressing (D) mutant *NRAS* or (E) mutant *BRAF* after shRNA mediated *AHCYL1* knockdown. F, AHCYL1 protein expression after knockdown checked by immunoblotting. Tumor volume and tumor weight of nude mice xenograft-implanted with human melanoma cells expressing mutated *NRAS* (G) or mutated *BRAF* (H) after shRNA-mediated *AHCYL1* knockdown. Cell proliferation of human melanoma cells harboring (I) *NRAS* mutation or (J) *BRAF* mutation after CRISPR-Cas9-mediated AHCYL1 knockout. NTC, nontargeting control. K, AHCYL1 protein expression after knockout checked by immunoblotting. L, Cell proliferation of *AHCYL1* knocked out *NRAS*-mutated human melanoma cells after putting back WT AHCYL1 or control vector. "KO" is the single-cell clone developed from HMCB sgAHCYL1 #1 (I), "rescue" is putting back CRISPR-Cas9-resistant WT AHCYL1 into "KO" cells (Supplementary Fig. S1G). M, AHCYL1 protein expression checked by immunoblotting. Error bars indicate means $\pm$ SD ($n \geq 3$). P values were calculated using two-tailed, unpaired Student t test (ns, not significant; *, $P \leq 0.05$; **, $P \leq 0.01$; ***, $P \leq 0.001$). Data A-E was generated by Dr. Jiayi Tu; Date C-H was generated by Dr. Rong Wu.

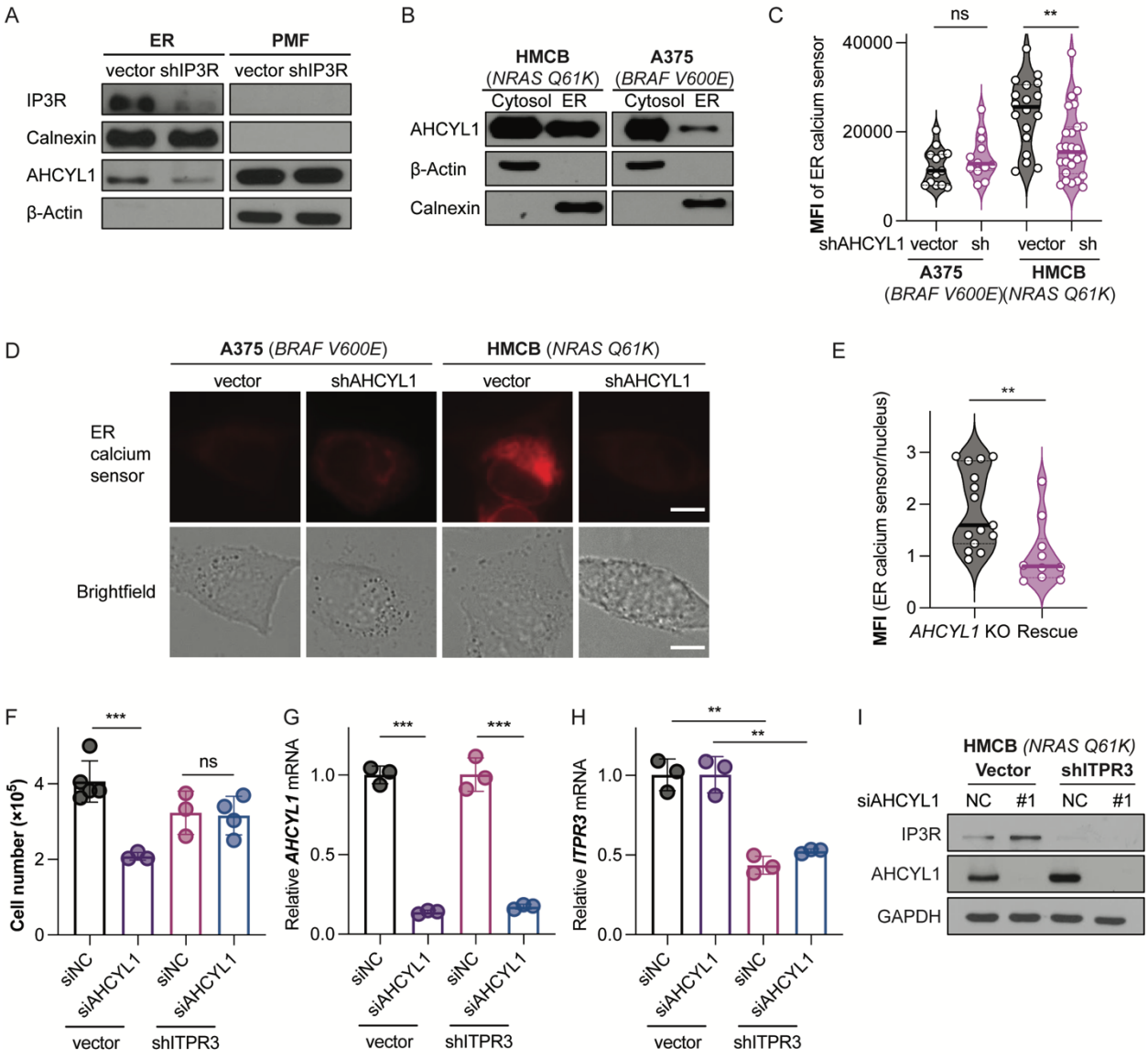

Figure 2.3

AHCYL1 deficiency causes a decrease in ER calcium. A, IP3R and AHCYL1 protein level in isolated ER or in post mitochondria fraction (PMF) of HMCB cells before and after shRNA mediated *IP3R* knockdown. PMF is the cytosol after removing the nucleus, the ER, and the mitochondria. B, AHCYL1 protein localization in human melanoma cells expressing mutant *NRAS* or mutant *BRAF* by immunoblotting. C, Mean fluorescence intensity (MFI) of ER calcium sensor in human melanoma cells expressing mutant *NRAS* or mutant *BRAF*

(continued)

after shRNA mediated *AHCYL1* knockdown. D, Representative images of ER calcium sensor, scale bar is 10 um. E, MFI of ER calcium sensor relative to the nucleus in AHCYL1-ablated *NRAS*-mutated HMCB human melanoma cells after putting back WT AHCYL1 expression vector or control vector. F, Endpoint cell number of ITPR3-ablated *NRAS*-mutated HMCB human melanoma cells after siRNA-mediated *AHCYL1* knockdown. Relative (G) *AHCYL1* and (H) *ITPR3* mRNA expression were checked by RT-qPCR. I, AHCYL1 and IP3R protein expression was checked by immunoblotting. Error bars indicate means $\pm$ SD ($n \geq 3$). P values were calculated using two-tailed, unpaired Student t test (ns, not significant; *, $P \leq 0.05$; **, $P \leq 0.01$; ***, $P \leq 0.001$). Data B is generated by Dr. Rong Wu.

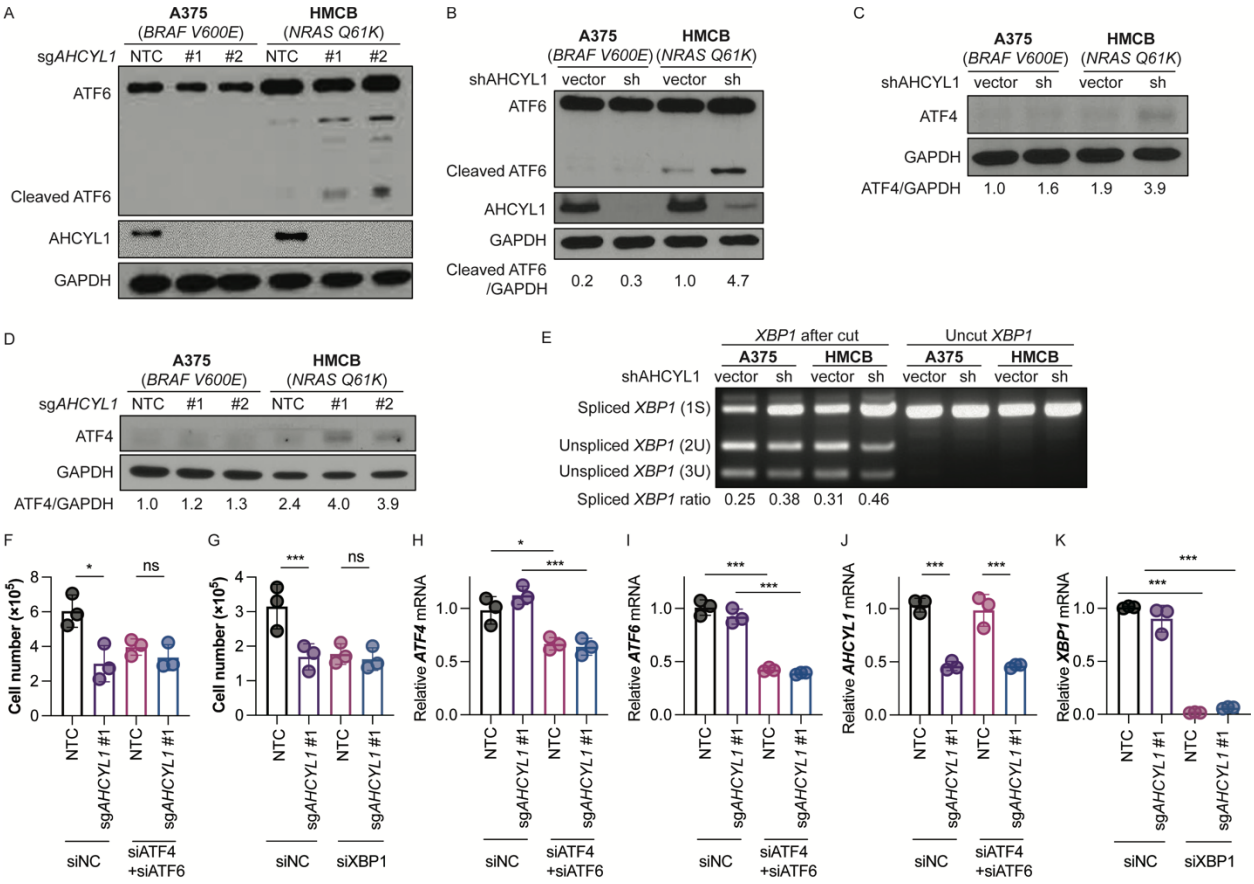

Figure 2.4

AHCYL1 deficiency activates the unfolded protein response (UPR). ATF6 protein cleavage in human melanoma cells expressing mutant *NRAS* or mutant *BRAF* after (A) CRISPR-Cas9–mediated *AHCYL1* knockout or (B) shRNA-mediated *AHCYL1* knockdown by immunoblotting. ATF4 protein expression in human melanoma cells expressing mutant *NRAS* or mutant *BRAF* after (C) shRNA-mediated *AHCYL1* knockdown (two minutes exposure time for ATF4) or (D) CRISPR-Cas9–mediated *AHCYL1* knockout (two minutes exposure time for ATF4) by immunoblotting. E, *XBP1* splicing assay for human melanoma cells expressing mutant *NRAS* or mutant *BRAF* after shRNA mediated *AHCYL1* knockdown by gel electrophoresis. Endpoint cell number of HMCB cells with or without (F) *ATF4* and *ATF6*, or (G) *XBP1*

(continued)

knockdown before and after *AHCYL1* knockout; knockdown efficiency of (H) *ATF4*, (I) *ATF6*, (J) *AHCYL1*, and (K) *XBP1*. Error bars indicate means ± SD ($n \geq 3$). P values were calculated using two-tailed, unpaired Student t test (ns, not significant; *, $P \leq 0.05$; **,$P \leq 0.01$; ***, $P \leq 0.001$). Data G and K were generated by Dr. Jiayi Tu.

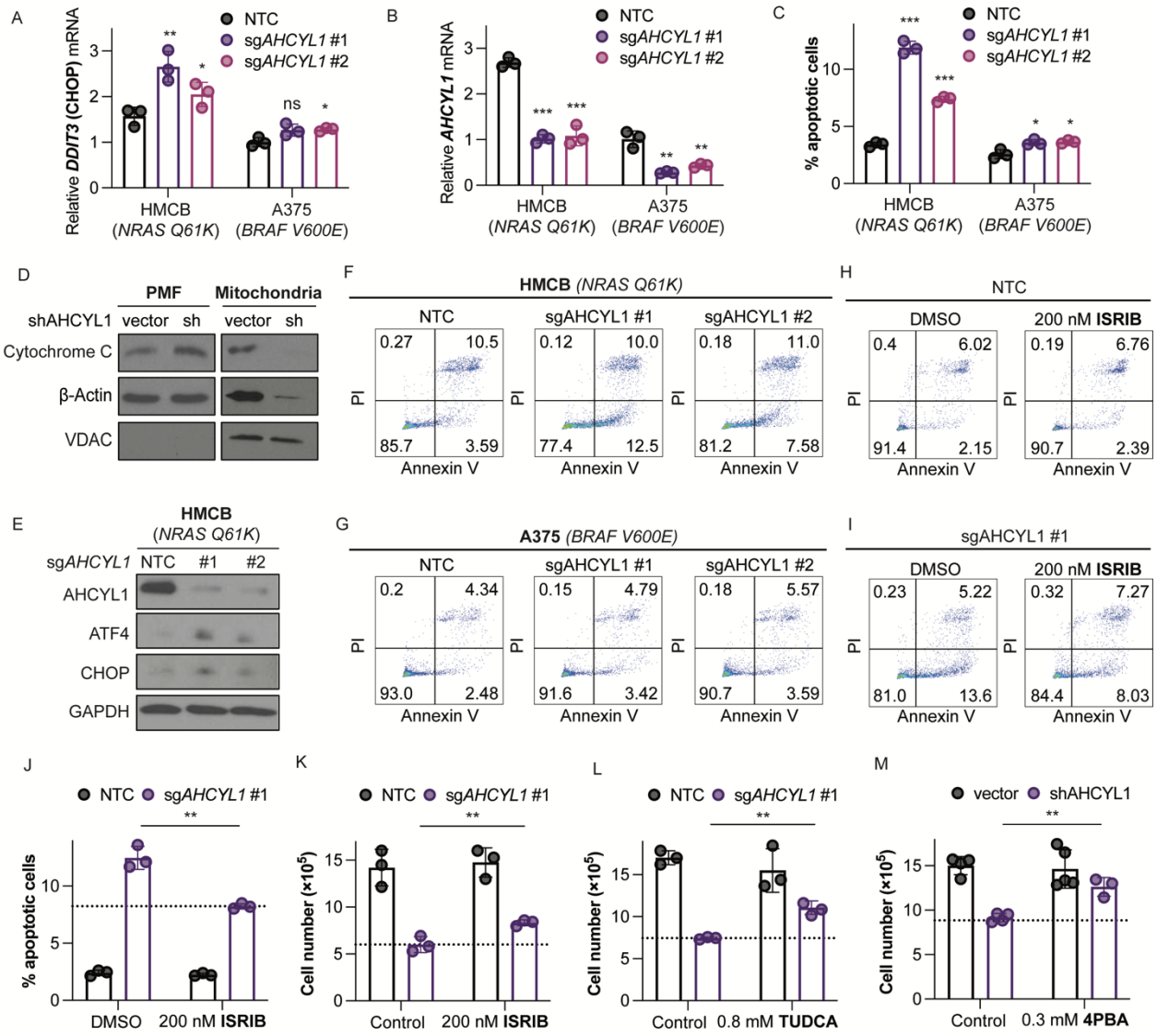

Figure 2.5

AHCYL1 deficiency triggers apoptosis resulting from the UPR activation. Relative (A) DDIT3 (CHOP) and (B) AHCYL1 mRNA expression after CRISPR-Cas9-mediated AHCYL1 knockout in HMCB and A375 human melanoma cells. C, Percentage apoptotic cells after AHCYL1 knockout in HMCB and A375 cells by Annexin V and PI staining. Representative cell apoptosis flow cytometry images by Annexin V and PI staining in human melanoma cells expressing (D) NRAS mutant or (E) BRAF mutant after AHCYL1 knockout. Representative cell

(continued)

apoptosis flow cytometry images in HMCB cells treated with 200 nmol/L ISRIB (F) in control cells or (G) after AHCYL1 knockout; (H) Summary of percentage apoptotic cells. Endpoint cell number of AHCYL1-ablated or control NRAS-mutated HMCB human melanoma cells treated with (I) 200 nmol/L ISRIB, (J) 0.8 mmol/L TUDCA, or (K) 0.3 mmol/L 4PBA. Error bars indicate means $\pm$ SD ($n \geq 3$). P values were calculated using two-tailed, unpaired Student t test (ns, not significant; *, $P \leq 0.05$; **, $P \leq 0.01$; ***, $P \leq 0.001$).

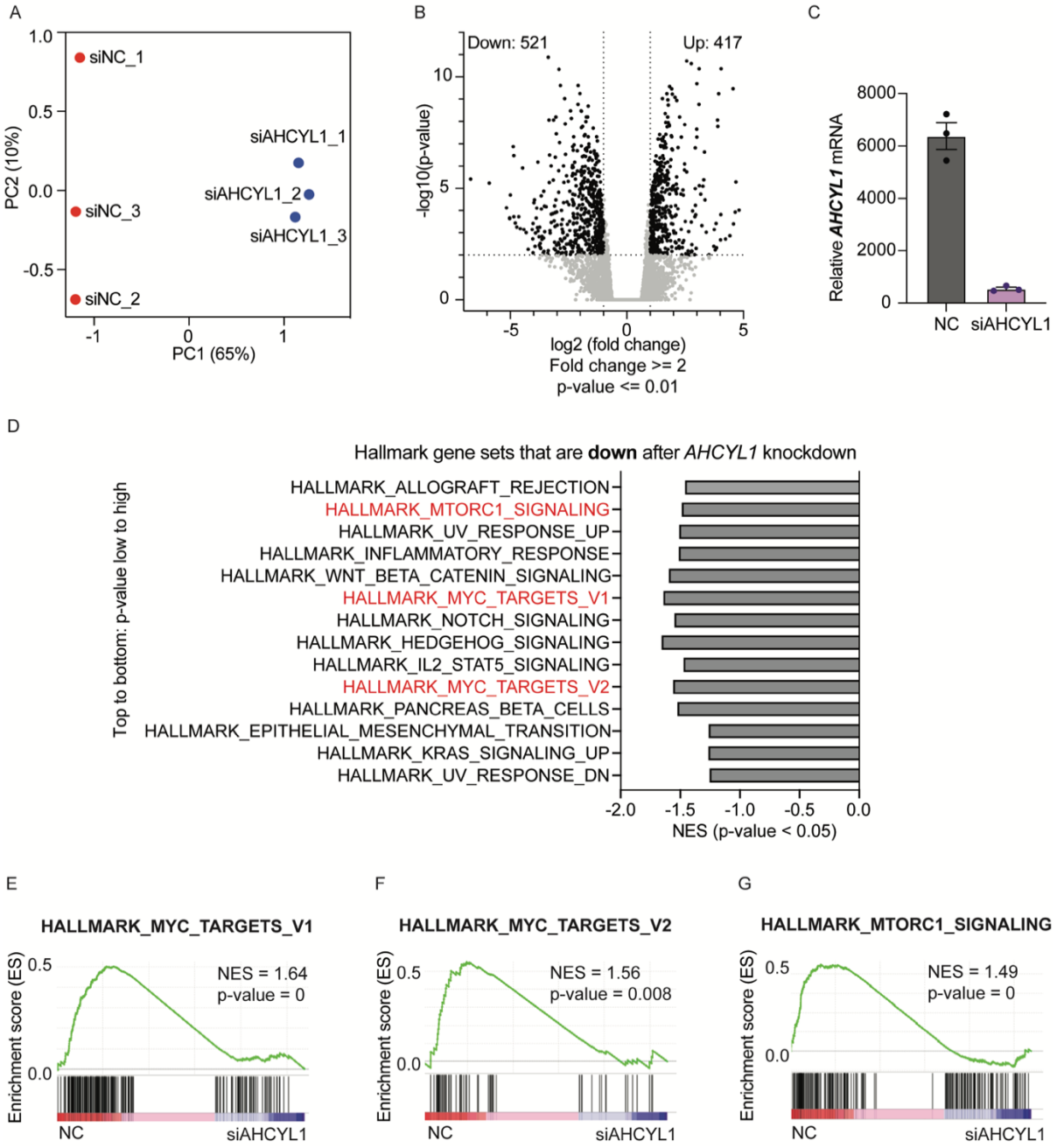

Figure 2.6

RNA-seq analysis shows downregulation of gene sets related to cell proliferation in *NRAS*-mutated human melanoma cells HMCB after *AHCYL1* knockdown. A, Principal component analysis (PCA) of RNA-seq samples from *NRAS*-mutated human melanoma cells after siRNA-mediated *AHCYL1* knockdown. B, RNA-seq volcano plot summary, fold change

(continued)

indicates gene expression of *AHCYL1* knockdown samples subtracted by gene expression of control samples. C, Relative *AHCYL1* mRNA levels after siRNA-mediated *AHCYL1* knockdown from RNA-seq analysis. D, Downregulated hallmark gene sets by gene set enrichment analysis (GSEA). GSEA of hallmark gene set (E) MYC targets V1, (F) MYC targets V2, and (G) MTORC1 signaling after siRNA-mediated *AHCYL1* knockdown in *NRAS*-mutated human melanoma cells. NES, normalized enrichment score. Error bars indicate means ± SD ($n \geq 3$). P values were calculated using two-tailed, unpaired Student t test (ns, not significant; *,$P \leq 0.05$; **, $P \leq 0.01$; ***, $P \leq 0.001$). Samples sent for RNA-seq analysis was generated by Dr. Rong Wu.

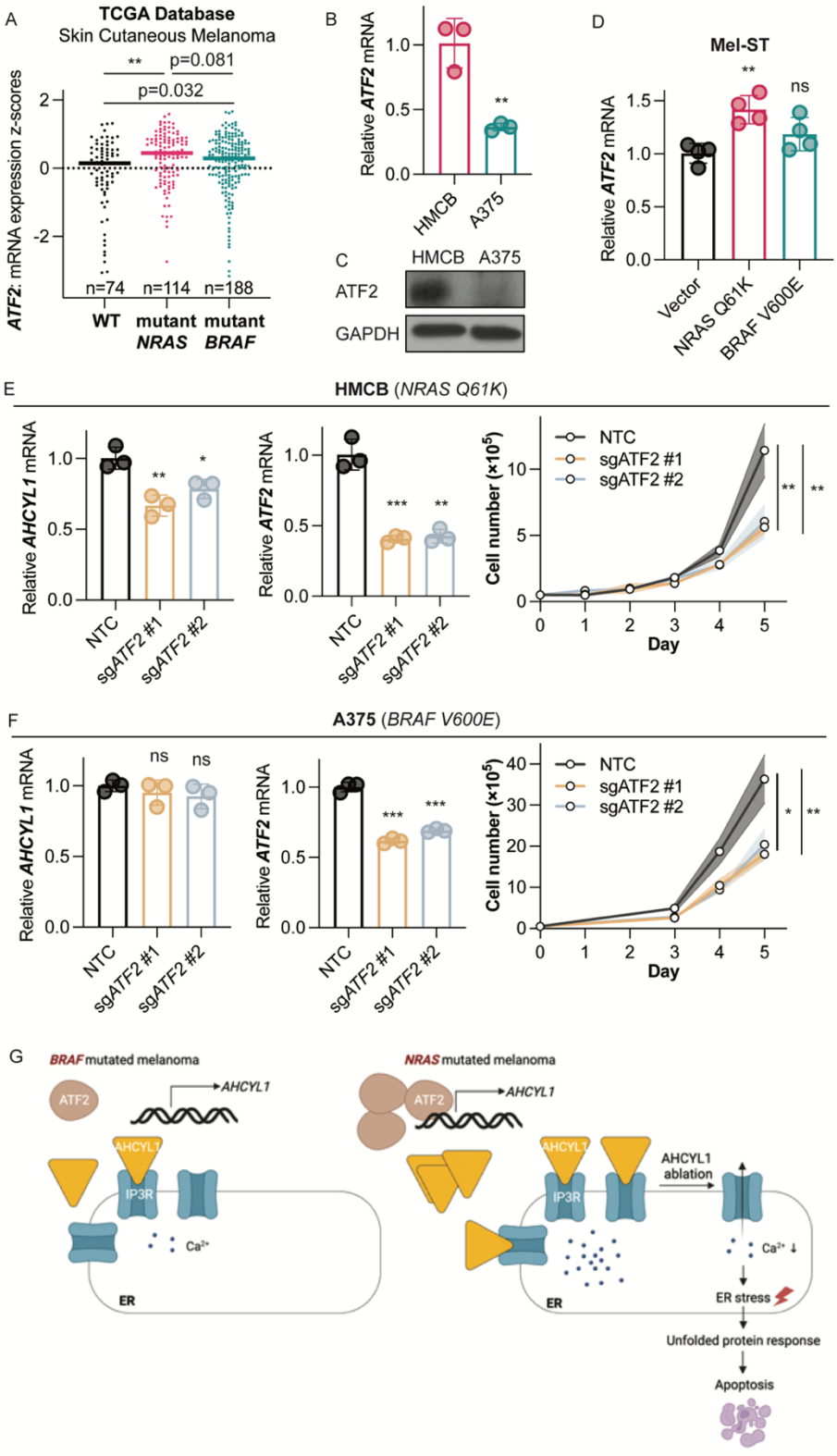

Figure 2.7 *AHCYL1* transcription in *NRAS*-mutated melanoma cells is regulated by the transcription factor ATF2. A, TCGA database analysis of *ATF2* mRNA levels in human skin cutaneous melanoma samples expressing *NRAS* mutant, *BRAF* mutant, or WT. Highlighted lines indicate data set median. B, *ATF2* relative mRNA expression in human melanoma cell lines expressing mutated *NRAS* or mutated *BRAF* by RT-qPCR. C, ATF2 protein expression in human melanoma cell lines expressing mutated *NRAS*

(continued)

or mutated *BRAF* by immunoblotting. D, Relative *ATF2* mRNA levels in human immortal melanocytes Mel-ST, exogenously expressed with mutated *NRAS*, mutated *BRAF*, or vector by RT-qPCR. E, Relative *AHCYL1* (left) and *ATF2* (middle) mRNA levels after *ATF2* knockout by RT-qPCR. Cell proliferation (right) of human melanoma cells expressing *NRAS* mutant. F, Relative *AHCYL1* (left) and *ATF2* (middle) mRNA levels after *ATF2* knockout by RT-qPCR. Cell proliferation (right) of human melanoma cells expressing *BRAF* mutant. G, Proposed working model (created with BioRender.com). Error bars indicate means ± SD ($n \geq 3$). P values were calculated using two-tailed, unpaired Student t test (ns, not significant; *, $P \leq 0.05$; **, $P \leq 0.01$; ***, $P \leq 0.001$).

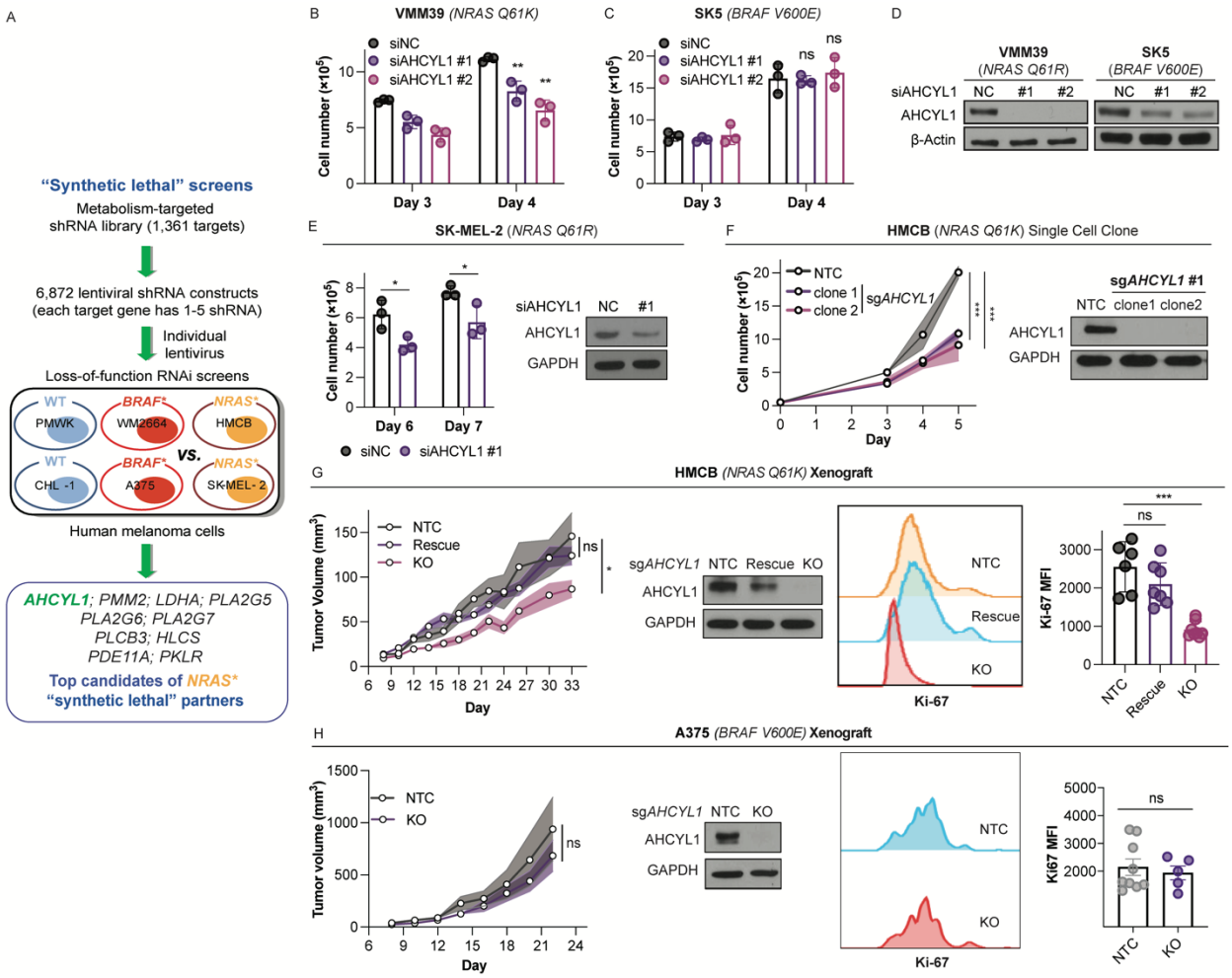

Figure S2.1

AHCYL1 is selectively critical for *NRAS*-mutated but not for *BRAF*-mutated human melanoma cells. A, Screening strategy: supervised analysis of viability data obtained from loss-of-function RNAi screens to identify candidate genes that are metabolism-related, which, when knocked down by shRNAs, distinguish human melanoma cells expressing mutant *NRAS* cells from *BRAF V600E* human melanoma cells and cells expressing wild-type *BRAF* and *NRAS*. Cell proliferation of human melanoma cells expressing (B) *NRAS* mutation or (C) *BRAF* mutation after siRNA mediated *AHCYL1* knockdown. D, AHCYL1 protein expression after knockdown checked by immunoblotting. E, Cell proliferation of human melanoma cells

(continued)

SK-MEL-2 expressing mutant *NRAS* after siRNA mediated *AHCYL1* knockdown (left); AHCYL1 protein levels after *AHCYL1* knockdown checked by immunoblotting (right). F, Cell proliferation of single cell clones from *AHCYL1* knockout *NRAS*-mutated human melanoma cells, and single cell clones were obtained from AHCYL1 knockout cells sgAHCYL1 #1 (Fig. 2I) (left); AHCYL1 protein expression of single cell clones by immunoblotting (right). G, Tumor growth potential in nude mice xenograft-implanted with human melanoma cells expressing mutated *NRAS* before and after *AHCYL1* knockout and after putting back WT AHCYL1, called "Rescue". Cells were from *AHCYL1* knockout single cell clone 1 (Fig. S1F) (left); AHCYL1 protein expression checked by immunoblotting (middle left); Representative Ki-67 levels checked by flow cytometry (middle right); Summary of Ki-67 levels (right). H, Tumor growth potential in nude mice xenograft-implanted with human melanoma cells expressing mutated *BRAF* before and after *AHCYL1* knockout. Cells were from *AHCYL1* knockout single cell clone (left); AHCYL1 protein expression checked by immunoblotting (middle left); Representative Ki-67 levels checked by flow cytometry (middle right); Summary of Ki-67 levels (right). Error bars indicate means ± SD ($n \geq 3$). p-values were calculated using two-tailed, unpaired Student's t-test (ns, not significant; *, $p \leq 0.05$; **, $p \leq 0.01$; ***, $p \leq 0.001$). Data B-D was generated by Dr. Rong Wu.

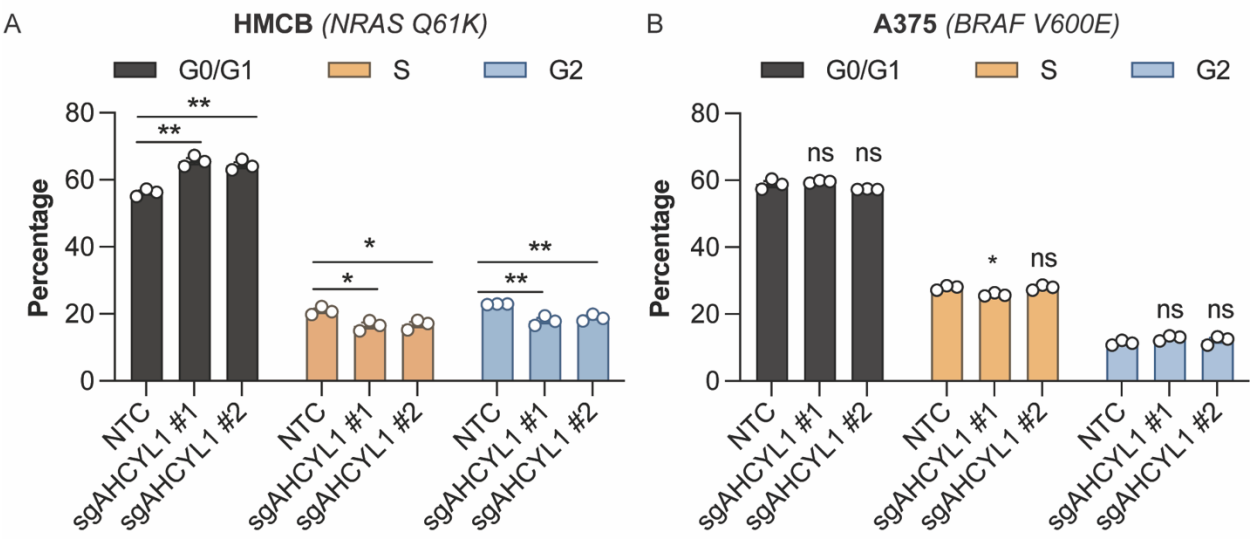

Figure S2.2

AHCYL1 knockout selectively causes cell cycle arrest in *NRAS*-mutant expressing human melanoma cells. Percentage of cells in G0/G1, S, or G2 phases of the cell cycle before and after *AHCYL1* knockout, in A, HMCB cells (*NRAS* mutation) and B, A375 cells (*BRAF* mutation). Error bars indicate means ± SD ($n \geq 3$). p-values were calculated using two-tailed, unpaired Student's t-test (ns, not significant; *, $p \leq 0.05$; **, $p \leq 0.01$; ***, $p \leq 0.001$).

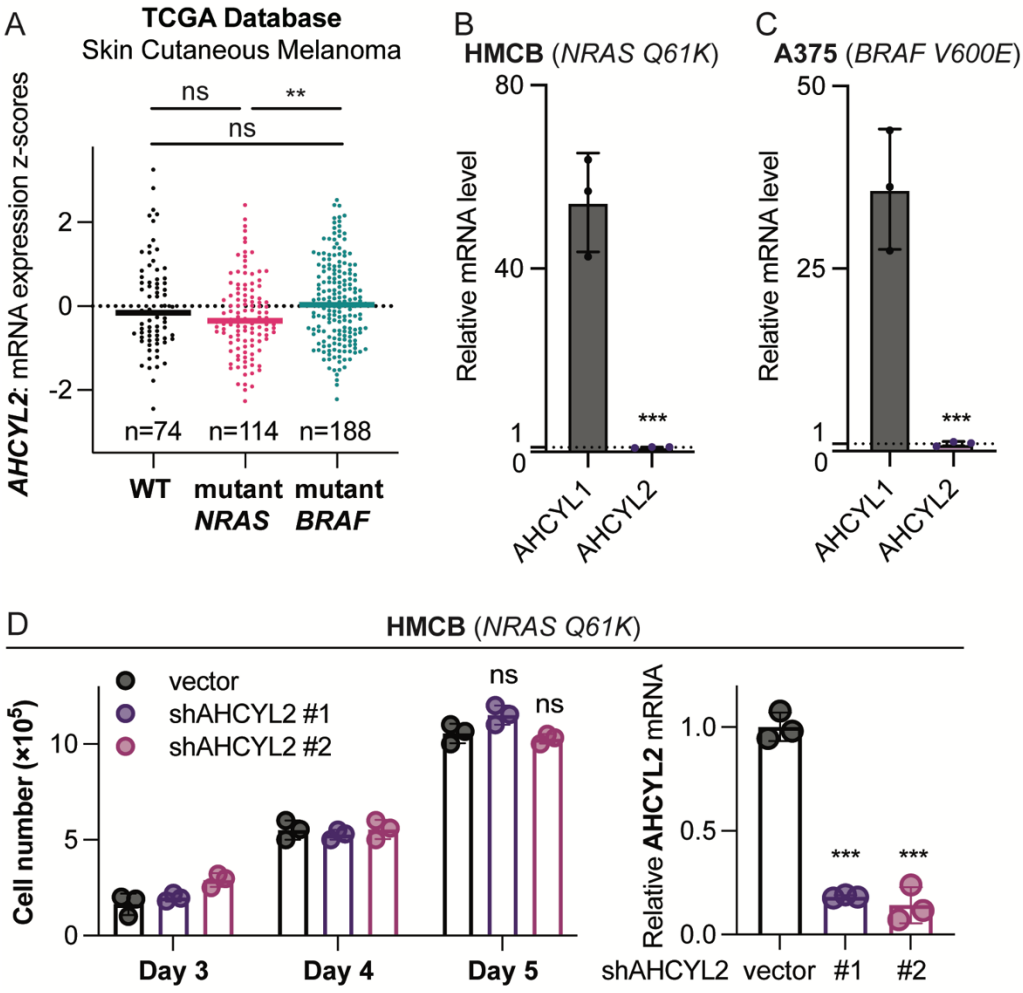

Figure S2.3

AHCYL2 does not overexpress and is not critical in human *NRAS*-mutated melanoma as AHCYL1. A, TCGA database analysis of *AHCYL2* mRNA levels in human skin cutaneous melanoma samples expressing mutated *NRAS*, mutated *BRAF*, or WT. Highlighted lines indicate dataset median. Relative *AHCYL1* and *AHCYL2* mRNA expression in human melanoma cells expressing (B) mutated *NRAS* or (C) mutated *BRAF*. D, Cell proliferation of human melanoma cells expressing *NRAS* mutant after shRNA-mediated *AHCYL2* knockdown (left); *AHCYL2* knockdown efficiency by RT-qPCR (right). Error bars indicate means ± SD (n ≥ 3).

(continued)

p-values were calculated using two-tailed, unpaired Student's t-test (ns, not significant; *, $p \leq 0.05$; **, $p \leq 0.01$; ***, $p \leq 0.001$).

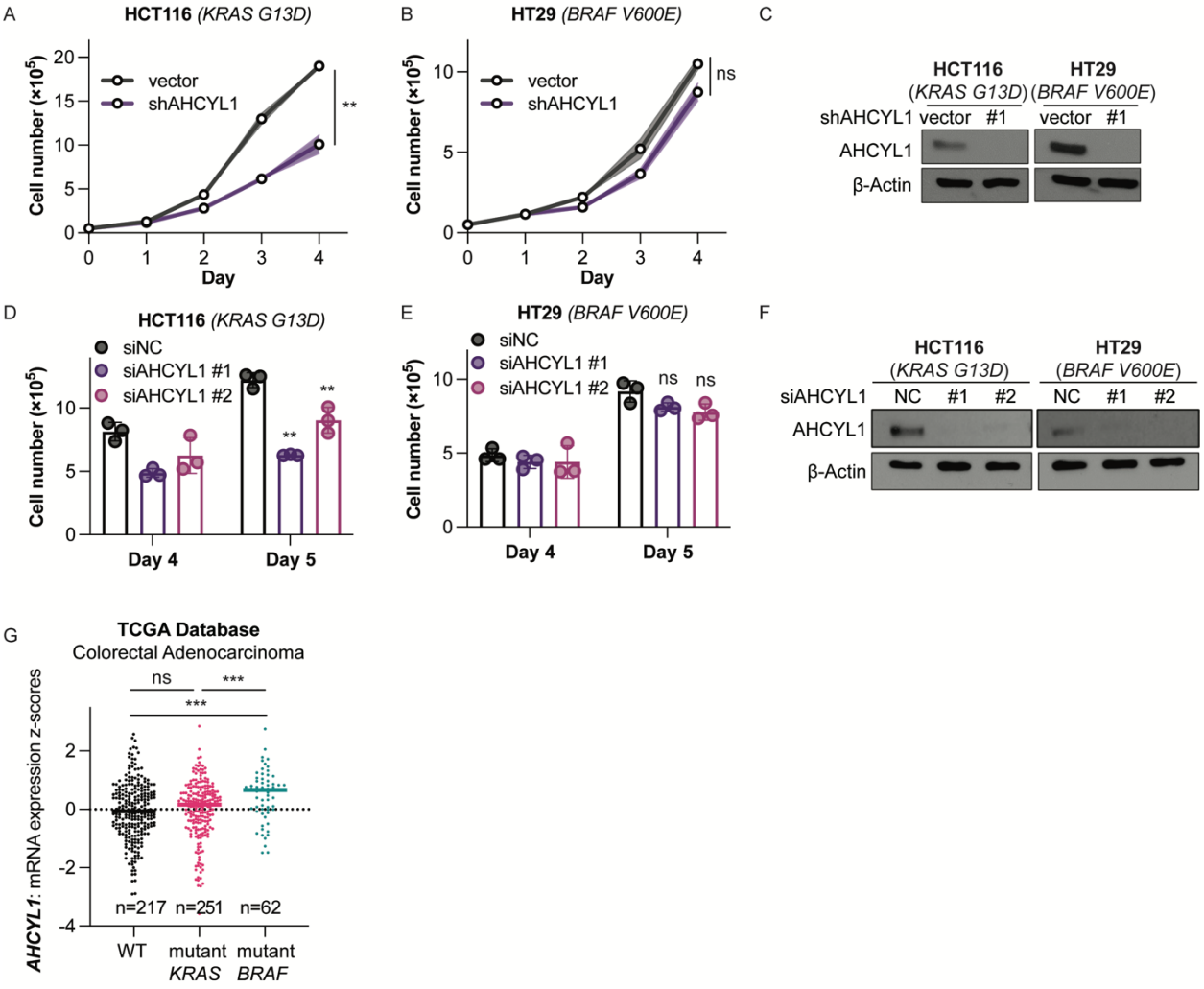

Figure S2.4

AHCYL1 is selectively critical for *KRAS*-mutated but not for *BRAF*-mutated human colorectal cancer cells. Cell proliferation of human colon cancer cells expressing (A) mutant *KRAS* or (B) mutant *BRAF* after shRNA mediated *AHCYL1* knockdown. C, AHCYL1 protein expression after knockdown checked by immunoblotting. Cell proliferation of human colon cancer cells expressing (D) *KRAS* mutation or (E) *BRAF* mutation after siRNA mediated *AHCYL1* knockdown. F, AHCYL1 protein expression after knockdown checked by immunoblotting. TCGA database analysis of *AHCYL1* (G) mRNA levels in human colorectal adenocarcinoma samples expressing mutated *NRAS*, mutated *BRAF*, or WT. Highlighted lines

(continued)

indicate dataset median. Error bars indicate means ± SD (n ≥ 3). p-values were calculated using two-tailed, unpaired Student's t-test (ns, not significant; *, p ≤ 0.05; **, p ≤ 0.01; ***, p ≤ 0.001). All the data in this figure was generated by Dr. Rong Wu.

Figure S2.5

IP3R deficiency doesn't change AHCYL1 protein level in the whole cell lysates. A, IP3R and AHCYL1 protein level in isolated ER or in post mitochondria fraction (PMF) of A375 cells before and after shRNA mediated *IP3R* knockdown. PMF is the cytosol after removing the nucleus, the ER, and the mitochondria. B, AHCYL1 protein levels before and after shRNA mediated *IP3R* knockdown in human melanoma cells expressing mutant *NRAS* (HMCB) or mutant *BRAF* (A375) by immunoblotting.

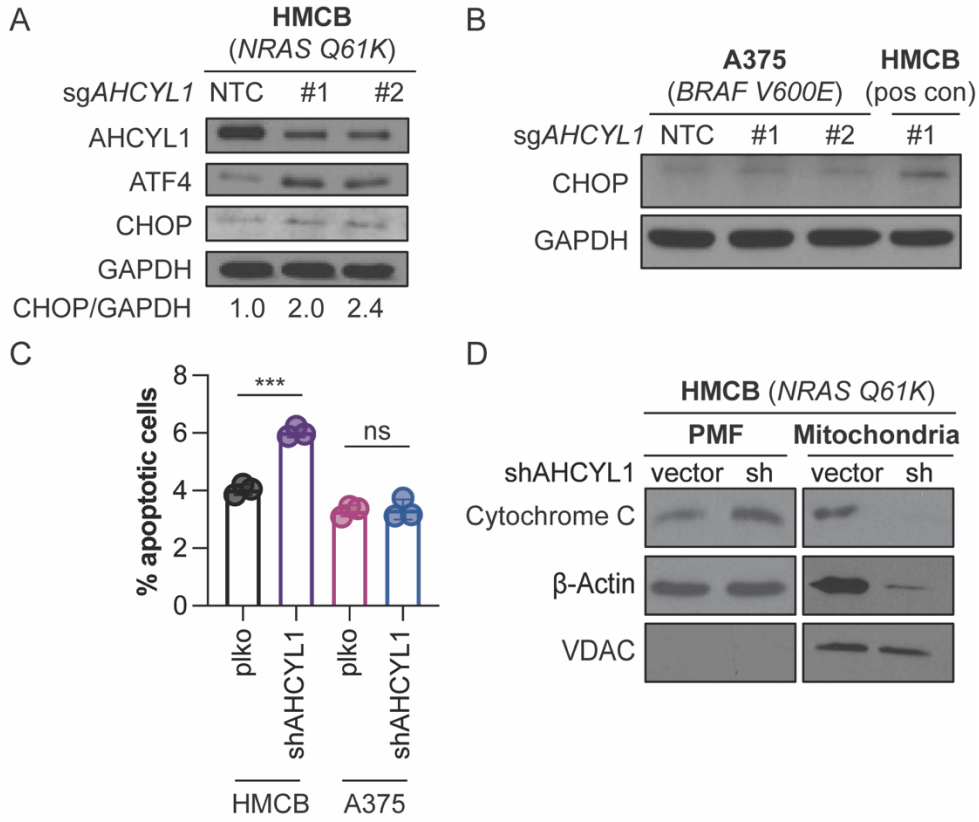

Figure S2.6

AHCYL1 deficiency triggers apoptosis resulted from the UPR activation. A, AHCYL1, ATF4, and CHOP protein expression after CRISPR-Cas9 mediated *AHCYL1* knockout in HMCB cells. B, CHOP protein expression after CRISPR-Cas9 mediated *AHCYL1* knockout in A375 cells, "pos con" is positive control. C, Percentage apoptotic cells after shRNA mediated *AHCYL1* knockdown by Annexin V and PI staining in both HMCB and A375 cells. D, Cytochrome C level in PMF or in isolated mitochondria in HMCB cells before and after shRNA mediated *AHCYL1* knockdown. Error bars indicate means ± SD (n ≥ 3). p-values were calculated using two-tailed, unpaired Student's t-test (ns, not significant; *, $p \leq 0.05$; **, $p \leq 0.01$; ***, $p \leq 0.001$).

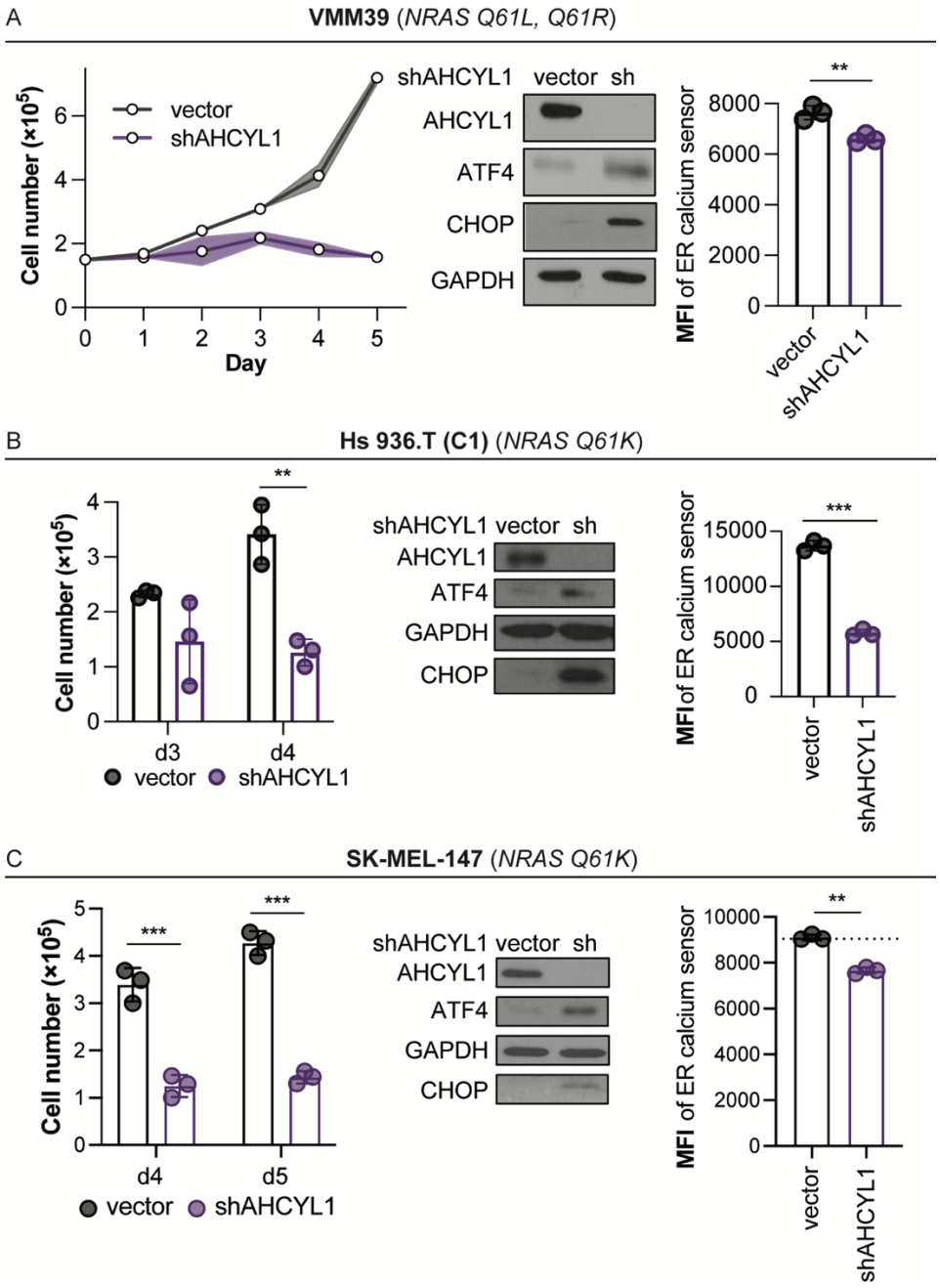

Figure S2.7

AHCYL1 deficiency attenuates cell proliferation, decreases ER calcium levels, and activates the UPR. A, Cell proliferation of human melanoma cells VMM39 expressing mutant *NRAS* after shRNA mediated *AHCYL1* knockdown (left); AHCYL1, ATF4, CHOP protein expression after *AHCYL1* knockdown checked by immunoblotting (middle); MFI of ER calcium

(continued)

sensor after shRNA mediated *AHCYL1* knockdown (right). B, Cell proliferation of human melanoma cells Hs 936.T expressing mutant *NRAS* after shRNA mediated *AHCYL1* knockdown (left); AHCYL1, ATF4, CHOP protein expression after *AHCYL1* knockdown checked by immunoblotting (middle); MFI of ER calcium sensor after shRNA mediated *AHCYL1* knockdown (right). C, Cell proliferation of human melanoma cells SK-MEL-147 expressing mutant *NRAS* after shRNA mediated *AHCYL1* knockdown (left); AHCYL1, ATF4, CHOP protein expression after *AHCYL1* knockdown checked by immunoblotting (middle); MFI of ER calcium sensor after shRNA mediated *AHCYL1* knockdown (right). p-values were calculated using two-tailed, unpaired Student's t-test (ns, not significant; *, $p \leq 0.05$; **, $p \leq 0.01$; ***, $p \leq 0.001$). All the calcium measurement in this figure was performed by Dr. Jiayi Tu.

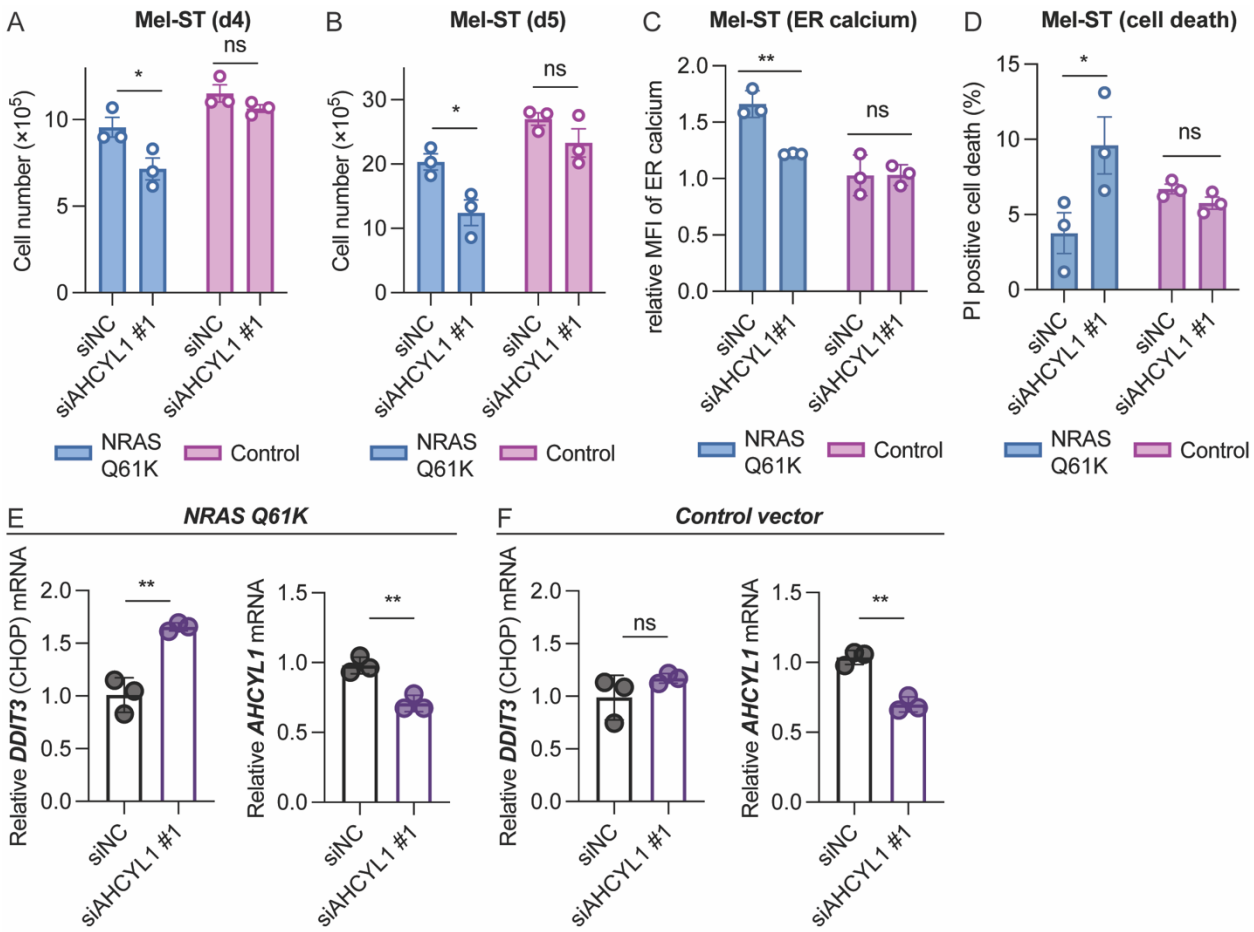

Figure S2.8

AHCYL1 deficiency causes cell growth attenuation, ER calcium decrease, and apoptosis in *NRAS-Q61K* overexpressed Mel-ST cells. Cell proliferation of *NRAS Q61K* overexpressed-human Mel-ST cells before and after *AHCYL1* knockdown by siRNA, cell number checked at (A) day 4 and (B) day 5; overexpression of control vector serves as control. MFI of ER calcium (C) and cell death (D) in *NRAS Q61K* overexpressed-human Mel-ST cells before and after *AHCYL1* knockdown by siRNA. Relative *DDIT3* (CHOP) and *AHCYL1* mRNA level before and after siRNA mediated *AHCYL1* knockdown in *NRAS Q61K* (E) or control vector (F) overexpressed-human Mel-ST cells. Error bars indicate means ± SD (n ≥ 3). p-values

(continued)

were calculated using two-tailed, unpaired Student's t-test (ns, not significant; *, $p \leq 0.05$; **, $p \leq 0.01$; ***, $p \leq 0.001$). Data C and D were generated by Dr. Jiayi Tu.

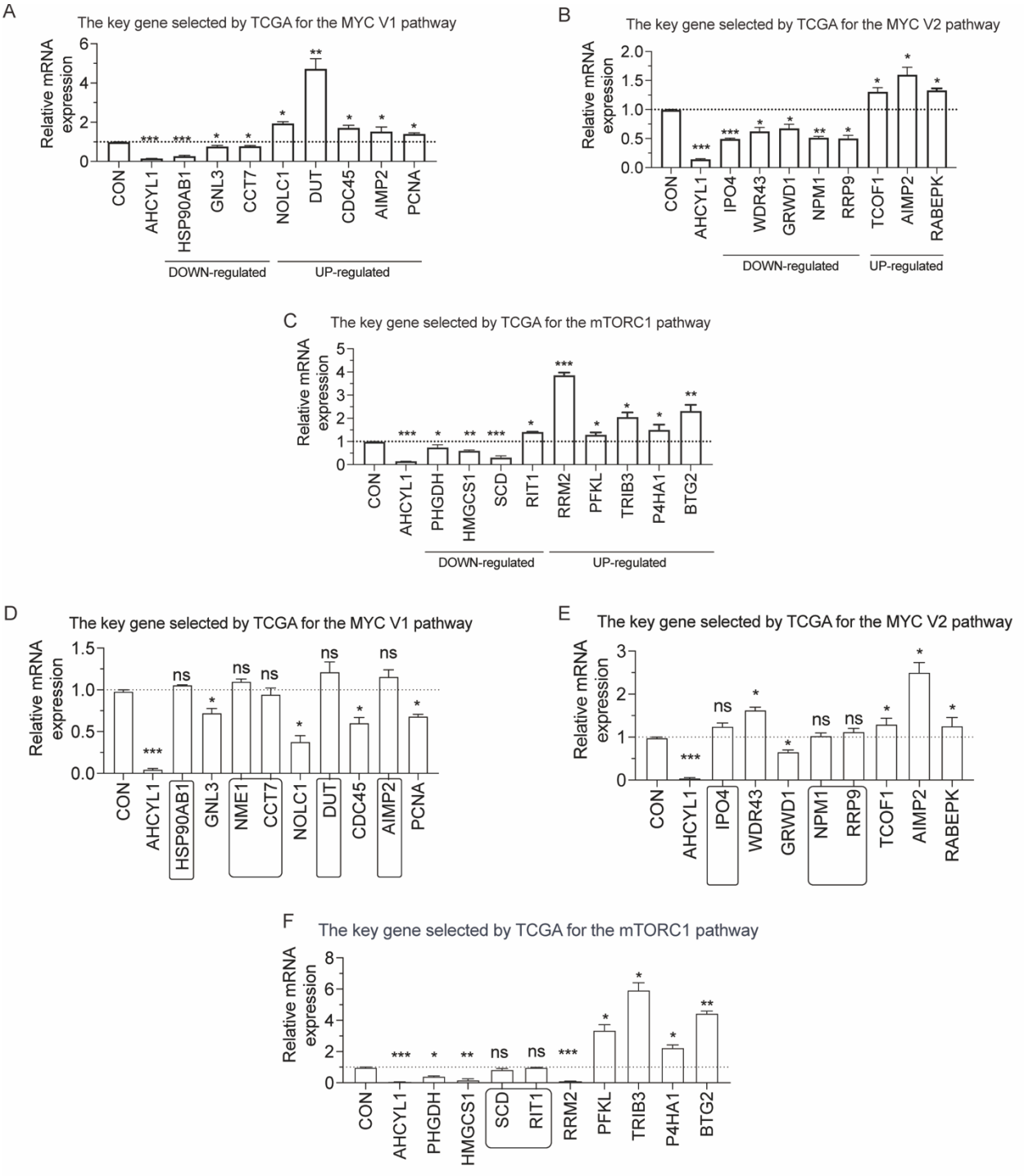

Figure S2.9

RT-qPCR validates key up/downregulated target genes from gene sets related to cell proliferation from RNA-seq. A, Relative mRNA levels of key up/downregulated

(continued)

genes from Hallmark_MYC_Targets_V1 gene set after siRNA mediated *AHCYL1* knockdown by RT-qPCR in HMCB cells. B, Relative mRNA levels of key up/downregulated genes from Hallmark_MYC_Targets_V2 gene set after siRNA mediated *AHCYL1* knockdown by RT-qPCR in HMCB cells. C, Relative mRNA levels of key up/downregulated genes from Hallmark_MTORC1_Signaling gene set after siRNA mediated *AHCYL1* knockdown by RT-qPCR in HMCB cells. D, Relative mRNA levels of key up/downregulated genes from Hallmark_MYC_Targets_V1 gene set after siRNA mediated *AHCYL1* knockdown by RT-qPCR in A375 cells. E, Relative mRNA levels of key up/downregulated genes from Hallmark_MYC_Targets_V2 gene set after siRNA mediated *AHCYL1* knockdown by RT-qPCR in A375 cells. F, Relative mRNA levels of key up/downregulated genes from Hallmark_MTORC1_Signaling gene set after siRNA mediated *AHCYL1* knockdown by RT-qPCR in A375 cells. Error bars indicate means ± SD ($n \geq 3$). p-values were calculated using two-tailed, unpaired Student's t-test (ns, not significant; *, $p \leq 0.05$; **, $p \leq 0.01$; ***, $p \leq 0.001$). All the data in this figure was generated by Dr. Jiayi Tu.

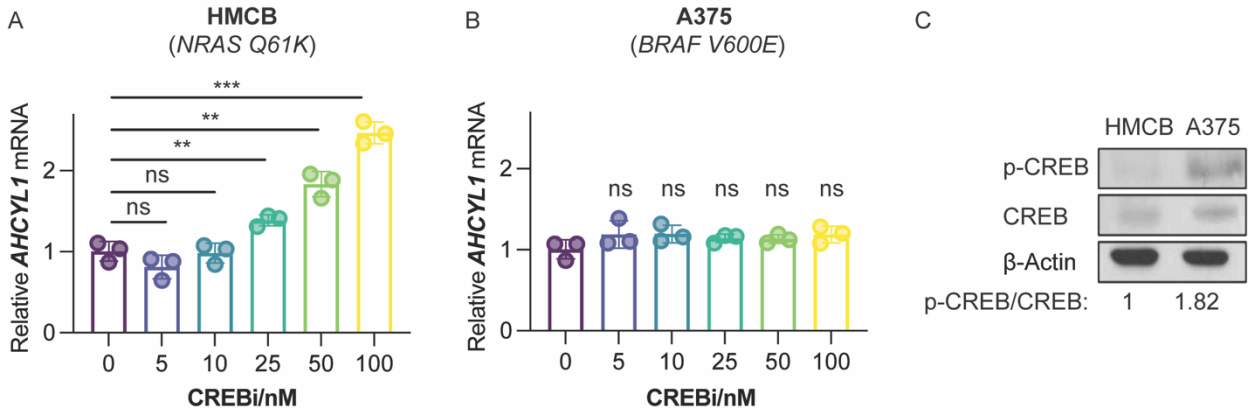

Figure S2.10

CREB doesn't positively regulate *AHCYL1* transcription. Relative *AHCYL1* mRNA levels after treated with dose-increasing concentrations of CREB inhibitor 666-15 in (A) *NRAS*-mutated and (B) *BRAF*-mutated human melanoma cells. C, CREB and p-CREB protein expression in *NRAS* or *BRAF* mutant expression human melanoma cells checked by immunoblotting. Error bars indicate means ± SD (n ≥ 3). p-values were calculated using two-tailed, unpaired Student's t-test (ns, not significant; *, p ≤ 0.05; **, p ≤ 0.01; ***, p ≤ 0.001).

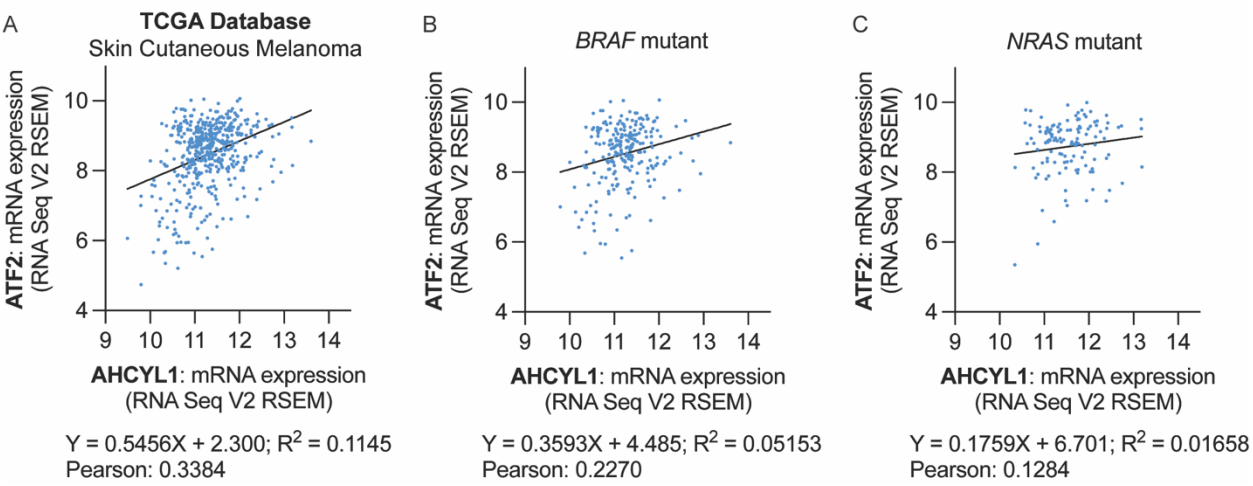

Figure S2.11

There is positive correlation between *ATF2* and *AHCYL1* mRNA levels in human cutaneous melanoma patients by TCGA analysis. A, *ATF2* and *AHCYL1* mRNA levels in human skin cutaneous melanoma patients regardless of mutation types. B, *ATF2* and *AHCYL1* mRNA levels in *BRAF* mutation harboring human skin cutaneous melanoma patients. C, *ATF2* and *AHCYL1* mRNA levels in *NRAS* mutation harboring human skin cutaneous melanoma patients.

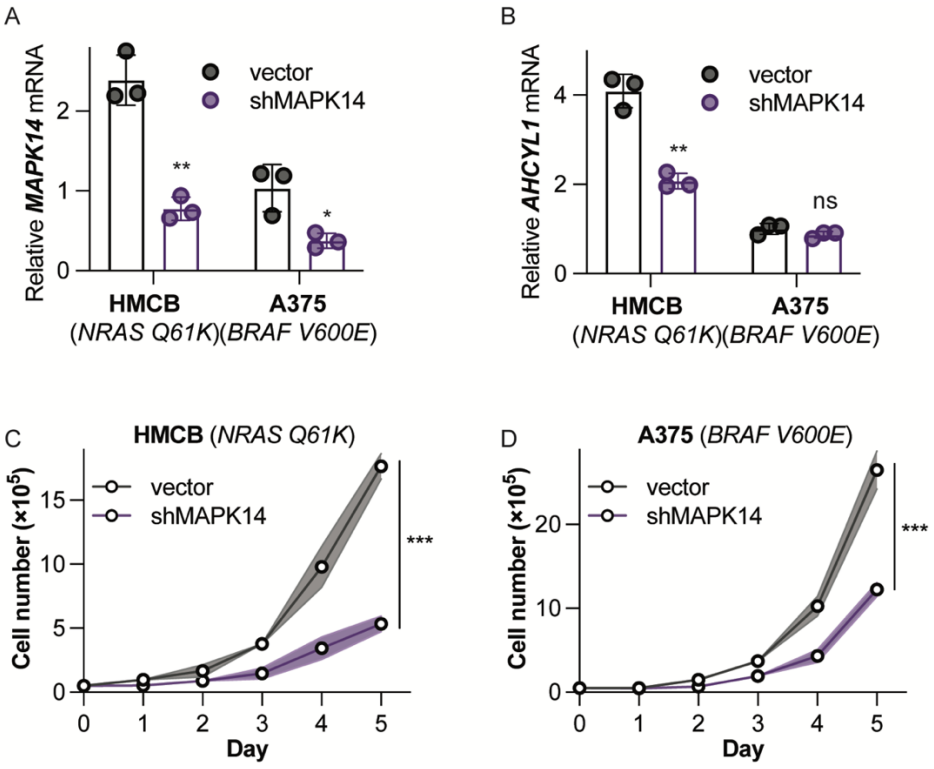

Figure S2.12

AHCYL1 transcription in *NRAS*-mutated melanoma cells is related to MAPK14. Relative (A) *MAPK14* and (B) *AHCYL1* mRNA expression before and after shRNA mediated *MAPK14* knockdown in HMCB and A375 human melanoma cells. Cell proliferation of human melanoma cells expressing (C) mutant *NRAS* or (D) mutant *BRAF* after shRNA mediated *MAPK14* knockdown. Error bars indicate means ± SD (n ≥ 3). p-values were calculated using two-tailed, unpaired Student's t-test (ns, not significant; *, p ≤ 0.05; **, p ≤ 0.01; ***, p ≤ 0.001).

Matrix identifier	Position (strand)	Core match	Matrix match	Sequence (always the (+) strand is shown)	Factor name
V$OCT1_Q6	75 (+)	0.893	0.891	gaccatGAAAAtcca	1-Oct
V$ELK1_02	372 (+)	1.000	0.98	aggacCGGAAggcc	Elk-1
V$AP1_Q2	535 (-)	1.000	0.991	tctgAGTCAgt	AP-1
V$AP1_Q4	535 (-)	1.000	0.981	tctgAGTCAgt	AP-1
V$HNF4_01	693 (-)	1.000	0.936	ctctggtCTTTGctcccaa	HNF-4
V$CREBP1_Q2	909 (+)	1.000	0.986	ggTGACGtcacg	CRE-BP1
V$CREBP1_Q2	909 (-)	1.000	0.983	ggtgaCGTCAcg	CRE-BP1
V$CREB_01	911 (+)	1.000	1.000	TGACGtca	CREB
V$CREB_01	911 (-)	1.000	1.000	tgaCGTCA	CREB
V$CREBP1CJUN_01	911 (+)	1.000	1.000	tGACGTca	CRE-BP1/c-Jun
V$CREBP1CJUN_01	911 (-)	1.000	1.000	tgACGTCa	CRE-BP1/c-Jun
V$HNF4_01	924 (-)	0.883	0.900	gagtgccCTTTCtccccgc	HNF-4

Supplemental Table 2.1

Transcription factor scan. Transcription factors candidates for *AHCYL1* transcription were generated based on reported binding response elements that can match *AHCYL1* promoter region sequence.

2.4 Discussion

Our study for the first time demonstrates the critical role of AHCYL1 in regulating ER calcium homeostasis in human melanoma and highlights the therapeutic potential of targeting AHCYL1 in *NRAS*-mutated melanoma. This is of clinical significance given the lack of effective treatments specific to *NRAS* mutations and the ever-present challenges of targeting mutated *NRAS* itself (Moore et al. 2020). Our study reinforces the strategy of targeting synthetic lethal partners in addition to targeting hard-to-target oncogenes directly, which can be worth for therapeutic exploration (Ryan et al. 2023; Huang et al. 2020). Additionally, we also showed that the critical role of AHCYL1 may apply to broader *RAS* mutation harboring cancers, such as *KRAS*-mutated human colorectal cancer (Fig. S2.4). Thus, AHCYL1 can be a promising target for *RAS* mutated human cancers.

Conceptually, our finding highlights the critical role of ER calcium homeostasis for cancer cell proliferation and survival (Sehgal et al. 2017; Preissler et al. 2020; Ibarra et al. 2022; Krebs, Agellon, and Michalak 2015; Luo and Lee 2013; Bahar, Kim, and Yoon 2016), and that the sustained UPR can trigger cell apoptosis (Sano and Reed 2013). Moreover, we not only observed changes in ER calcium before and after AHCYL1 deficiency but also there are differences in cellular basal ER calcium levels: in *NRAS*-mutated human melanoma cell HMCB, the basal ER calcium is significantly higher than *BRAF*-mutated melanoma cell A375 (Fig. 2.3C). This observation raises the question of whether basal ER calcium levels vary across cell types and whether such variation is oncogenic background dependent. Particularly, *NRAS*-mutated melanoma has been reported to be more sensitive to intracellular calcium alterations than *BRAF*-mutated melanoma (Esteves et al. 2020). Intriguingly, we also noted that HMCB cells were larger in size than A375, suggesting greater cell growth and more extensive protein

synthesis and folding in *NRAS*-mutated HMCB cells. Future studies will explore whether cell growth and size can be oncogene-dependent and whether they correlate with basal ER calcium levels and protein folding requirements. To summarize, *NRAS* and *BRAF* mutant expressing human melanoma cells respond differently to AHCYL1 deficiency, this may be attributed to the following reasons: we have found that AHCYL1 is selectively highly expressed in mutant *NRAS* but not mutant *BRAF* expressing human melanoma (Fig. 2.1), which leads to selectively higher calcium level in the ER (Fig. 2.3C) as well as basal UPR activation (Fig. 2.4A-2.4E) only in *NRAS* mutant-expressing HMCB cells but not in A375 cells expressing *BRAF V600E*. In addition, we found that there is more ER AHCYL1 protein in the *NRAS*-mutated than *BRAF*-mutated human melanoma cells (Fig. 2.3B). Thus, AHCYL1 deficiency in *NRAS*-mutated human melanoma cells causes calcium leakage from the ER and introduces additional ER stress signals, which ultimately causes cell apoptosis (Fig. 2.7G).

Moreover, our study expands the current understanding of the function and regulation of AHCYL1 protein itself. First, our work is consistent with previous literatures on the binding and suppression of IP3R by AHCYL1 (Ando et al. 2006, 2003; Devogelaere et al. 2006), and we further show that AHCYL1 deficiency disrupts downstream ER calcium homeostasis, activates the UPR and triggers apoptosis in cancer cells. In addition to the downstream of AHCYL1, our work also reveals that AHCYL1 upstream transcription is controlled by ATF2 (Fig. 2.7) and may relate to p38α (MAPK14) (Fig. S2.12). Consistent with AHCYL1 selective upregulation, we show that its transcription factor ATF2 is also selectively upregulated in *NRAS*-mutated melanoma cell HMCB (Fig. 2.7A-2.7C). Previous studies indicate that ATF2 is activated by stress

kinases JNK and p38 (Lopez-Bergami, Lau, and Ronai 2010; Fritz et al. 2021; Lau and Ronai 2012; Wan et al. 2020), and that ATF2 is a reported downstream target of MAPK14 (Wan et al. 2020; Fritz et al. 2021). Interestingly, JNK and p38 pathways are known to be activated by mutated *RAS*, which may explain why AHCYL1 upregulation is specific to *NRAS*-mutated melanoma but not observed in *BRAF*-mutated melanoma that belongs to the ERK pathway (Pua et al. 2022). In future studies, it would be valuable to investigate the detailed signaling regulation, especially phosphorylation status and the protein activities.

Over the past decade, our research group and others elucidated multiple oncogene-specific metabolic regulations (Xia et al. 2017; Kang et al. 2015; Gao et al. 2022; Zhao et al. 2017; Lin et al. 2018; Min and Lee 2018; Tarrado-Castellarnau, de Atauri, and Cascante 2016). We have found that the ketogenic enzyme HMG-CoA lyase (HMGCL) is selectively essential in melanoma cells expressing *BRAF V600E*, where its product acetoacetate promotes *BRAF V600E*-dependent MEK1 activation (Kang et al. 2015; Xia et al. 2017; Zhao et al. 2017). Moreover, we demonstrated that chondroitin-4-sulfate (CHSA), a circulating dietary supplement, exhibits intracellular signaling function by enhancing casein kinase II (CKII)-PTEN binding, leading to PTEN inhibition and subsequent AKT activation, which are crucial for cancers expressing *BRAF V600E* (Lin et al. 2018). We also reported that Phospholipase A2, group VII (PLA2G7) and Lyso-PAF act as key elements of RAS-RAF1 signaling and exhibit intracellular signaling functions (Gao et al. 2022). Our study on AHCYL1 further adds to this knowledge and demonstrates the concept of oncogene-specific calcium regulations in cancer cells, and sheds light on oncogene-mediated metabolic rewiring in cancer cells compare to normal cells, providing new insights in development of novel precision medicine for cancer treatment (Hanahan 2022).

CHAPTER 3: TUMOR MICROENVIRONMENTAL ATP REGULATES CANCER-ASSOCIATED FIBROBLAST HETEROGENEITY

ACKNOWLEDGEMENTS:

Data A in Sup Figure 3.2 was performed by Dr. Simon Schwörer.

All the rest experiments shown in this thesis were performed by me.

3.1 Introduction

Pancreatic ductal adenocarcinoma (PDAC) is one of the most aggressive cancers with a 13% five-year survival rate (American Cancer Society 2024), and it is predicted to be the second leading cause of cancer-related deaths in the United States by 2030 (Orth et al. 2019). One of the prominent features of PDAC is the desmoplastic response, in which the dense stroma can make up to 90% of the tumor mass (Helms, Onate, and Sherman 2020). Over the years, efforts have been made in targeting the stromal matrix, for example, in mice harboring PDAC, targeting hyaluronan improves chemotherapy through more efficient drug delivery (Jacobetz et al. 2013). However, a clinical trial targeting hyaluronan has failed in phase III to show any benefits in PDAC patients (Hakim et al. 2019). The PDAC stroma has a high abundance of cancer-associated fibroblasts (CAFs), which primarily produce the stromal milieu. Attempts have been made in depleting CAF-derived collagen I, while ultimately promotes PDAC growth and reduces survival in mouse models (Chen et al. 2021). In addition, depletion of alpha smooth muscle actin $(SMA)^+$ CAFs, which are the source of collagen I, led to increased tumor progression (Özdemir et al. 2014). Consistently, PDAC patients with higher amount of SMA^+ CAFs in tumors show better overall survival, but they also respond poorly to immunotherapies (Özdemir et al. 2014). These data suggest that a better understanding of the PDAC stroma is needed to develop advanced approaches for therapies that target both the stroma and cancer cells.

Over the last decade, functionally and transcriptionally heterogeneous CAF populations have been identified and gradually appreciated in both mouse and human PDAC (Öhlund et al. 2017; Elyada et al. 2019; Dominguez et al. 2020; Hosein et al. 2019). Myofibroblastic CAFs (myCAFs) feature expression of SMA, are the main producers of extracellular matrix, and are

thought to be tumor restraining (McAndrews et al. 2022; Özdemir et al. 2014). Meanwhile, inflammatory CAFs (iCAFs) are characterized by low SMA expression and their ability to secret inflammatory cytokines and chemokines such as IL-6 and CXCL1, and are thought to be tumor promoting (McAndrews et al. 2022; Lo et al. 2017; Schwörer et al. 2023). myCAF and iCAFs are the most abundant CAF populations in PDAC, however, another distinct yet smaller CAF population has been identified recently, the antigen presenting CAFs (apCAFs). apCAFs express MHC II and CD74 but lack classical co-stimulatory molecules; consequently, apCAFs can potentially activate $CD4^+$ T cells but cause anergy (Elyada et al. 2019). Based on their distinct roles in PDAC, selectively altering the CAF states is thought to have significant clinical benefits.

Heterogeneity within the CAF population has been suggested to be established in part by growth factors and cytokines. For example, TGFβ can induce myCAFs, TNFα, IL-1α and LIF can induce the iCAF state, and IFNγ can induce the apCAF state (Biffi et al. 2019; Elyada et al. 2019). While cytokines and growth factors can drive CAF heterogeneity, iCAF and myCAF states are plastic, i.e., they can convert into each other. How this plasticity is regulated is largely unknown. We recently identified oxygen availability in the tumor microenvironment (TME) as a central regulator of CAF state decisions, indicating that metabolic factors in the TME can modulate the CAF state (Schwörer et al. 2023).

Extracellular ATP (eATP) has been found to accumulate at high micromolar levels in the TME (Pellegatti et al. 2008; L.-P. Hu et al. 2019). eATP accumulates in the TME due to cellular stress and apoptosis, in addition, hypoxia also induces ATP release without cell injury (Di Virgilio et al. 2018), suggesting that eATP might contribute to iCAF accumulation in hypoxic PDAC regions. eATP can act as signaling molecule modulating immune functions and one of the

most established pathways is mediated by eATP binding to purinergic receptors (Di Virgilio et al. 2018). However, the role of eATP in regulating CAF state decisions is poorly understood.

Here, we report that, from a high-content screen using a human blood nutrient library (Fan et al. 2023) in combination with a fibroblast reporter (FIRE) system (Schwörer et al. 2023), we identified and validated that eATP blunts TGFβ-induced SMA expression and promotes cytokines-induced IL-6 expression in both time- and dose-dependent manner. Pretreatment of pancreatic stellate cells (PSCs) with physiological concentrations of eATP is sufficient to alter fibroblast states and to promote PDAC tumor growth. Mechanistically, our data suggest that eATP acts independently of its canonical purinergic receptor pathways to promote an iCAF state in PSCs. The JAK-STAT pathway, one of the major regulators of iCAFs (Biffi et al. 2019), is strongly activated upon eATP treatment and mediates its effect in inducing an iCAF state. Further, we showed this is serum dependent. These findings support the idea that TME metabolites can alter PDAC progression by regulating CAF heterogeneity.

3.2 Materials and Methods

Cell culture:

Human HEK293T (RRID: CVCL_0063) cells were obtained from the ATCC. PSCs (PSC1s and PSC3s) were isolated from *αSMA*-DsRed mice (LeBleu et al. 2013) or wildtype mice, respectively, by differential centrifugation as described previously (Jesnowski et al. 2005) and immortalized by spontaneous outgrowth. *IL6*-EGFP was introduced into PSC1s by viral transduction and PSC1 double (PSC1d) cells were generated featuring the FIRE system (Schwörer et al. 2023). KPC59 cells were a generous gift from the Muir Lab (Apiz Saab et al. 2023). HEK293T cells and PSCs were cultured in Dulbecco Modified Eagle Medium (DMEM; Gibco, 11965-092) with 10% fetal bovine serum (FBS; Sigma, F2442) and 1% penicillin/streptomycin (P/S; Gibco, 15070-063). KPC59 cells were cultured in RPMI-1640 (Gibco, 11875-093) with 10% FBS and 1% P/S. All the cells were cultured at 37℃ in 5% CO_2 and 20% O_2. For hypoxia experiments, cells were cultured in a hypoxia glove box (Coy) set at 1% O_2, 37°C and 5% CO_2 for 48 hours.

Cells were treated with a combination of 2 ng/ml murine IL-1α (Peprotech, 211-11A), TNFα (Peprotech, 315-01A), and LIF, as indicated ("cytokines"). Cells were also treated with 2 ng/ml TGFβ, 10 μM MLN120B (IKKβ inhibitor), 2 μM AZD1480 (JAK2 inhibitor), anti-leukemia inhibitory factor (LIF; 4 mg/mL, AF449, R&D), 100 μM cobalt chloride ($CoCl_2$; Sigma, C8661), 390 μM Adenosine 5′-triphosphate disodium salt hydrate (ATP; Sigma, A2383), 390 μM Adenosine 5′-diphosphate bis (cyclohexylammonium) salt (ADP; Sigma, A4386), 390 μM Adenosine-5'-monophosphate disodium salt (AMP; Fisher Scientific, AAJ6164306), 390 μM Adenosine (Cayman, 21232), 390 μM Adenine hydrochloride hydrate (Adenine; Sigma, A9795), 390 μM Adenosine 5'-(γ-thio)-triphosphate (lithium salt) (ATPγS; Cayman, 14957),

390 μM UDP-α-D-Glucose (Cayman, 15602), 390 μM UTP sodium salt (Cayman, 9003530), 390 μM UDP sodium salt hydrate (Cayman, 18137), 10 μM BAPTA AM (Cayman, 15551), 10 μg/ml LPS (Sigma, L4391), 10 μM MRS2578 (P2Y6 antagonist; Cayman, 19704), 10 μM AR-C 118925XX (P2Y2 antagonist; Biotechne, 4890), 10 μM AZ10606120 (P2X7 antagonist; Sigma, SML3600), 10 μM MRS2179 (P2Y1 antagonist; Cayman, 10011450), 10 μM 5-BDBD (P2X4 antagonist; Sigma, SML0450), 200 nM 666-15 (CREB inhibitor); 200 nM H89 (PKA inhibitor); 1 μM NLRPA3 agonist. Cell experiments were conducted and designed according to protocols approved by the Institutional Biosafety Committee of the University of Chicago.

Fibroblast reporter (FIRE) system and blood chemical screen on Incucyte:

We previously developed a novel fibroblast reporter (FIRE) system (Schwörer et al. 2023) to rapidly assess the CAF state in response to perturbations. In this FIRE system, the expression EGFP or dsRED fluorescent protein is driven by the murine *IL6* or *SMA* promoter regions, respectively.

For the screen, 10k PSC1d cells were seeded in 100 μl of media in 96-well plates, leaving top and bottom rows filled with PBS. The next day, media was changed into FluoroBrite DMEM (Gibco, A18967-01) supplemented with 1% Pen Strep Glutamine and 10% FBS. Blood nutrient library was added as previously reported (Fan et al. 2023) and known CAF inducers were added simultaneously. For hypoxia experimental conditions, plates were transferred to a hypoxia chamber set at 1% oxygen immediately after adding treatments. Cells were cultured for another 48 hours, and fluorescence was analyzed on IncuCyte S3 (Essen BioScience) at the UChicago Cellular Screening Center. To interpret fluorescence, we calculated the FIRE score combing the green and red fluorescence for every compound tested following equation:

$$FIRE\ score = log_2(\frac{DsRED\ fluorescence\ intensity}{EGFP\ fluorescence\ intensity})$$

$$Compound\ score = FIRE\ (compound\ X) - FIRE\ (DMSO)$$

Animal study:

The mouse study was approved by the Institutional Animal Care and Use Committee (IACUC) at the University of Chicago.

PSC1d cells and KPC59 cells were seeded separately, and PSC1d cells were treated with 390 nM ATP for 24 hours. Next day, cells were harvested and combined in 5:1 ratio in PBS (8.2 million PSC1d cells and 1.64 million KPC59 cells in 1 ml PBS for 10 injections) for subcutaneous co-injection. Tumor growth was measured starting from 8 days after inoculation by measurement of two perpendicular diameters with calipers. Tumor volume was calculated using formula $4\pi/3 \times (\text{width}/2)^2 \times (\text{length}/2)$, and tumors were harvested from euthanized mice and weighed at experimental endpoints. Freshly excised mouse tumor tissues were minced into small pieces by scissors in cold PBS and transferred and digested in 10 ml digestion buffer (HBSS, 0.8 ml/ml Dispase II, 0.5 mg/ml Collagenase P, 0.1 mg/ml Liberase TL, 0.1 mg/ml DNAse I, 0.4 mg/ml Hyaluronidase, and 0.02 mg/ml trypsin inhibitor). The digestion reaction was quenched by adding 0.5 mM EDTA pH 8.0. The digested tumor tissues were then filtered into new tube through 40 μm nylon mesh strainer and centrifuged at 500 g for 5 minutes at room temperature, supernatant was discarded. Then, 5 ml ACK lysis buffer was added, and tumor tissues were incubated at room temperature for 3 minutes. Reaction was quenched by FBS-containing media and washed 3 times. Next, isolated tumor cells were processed for flow cytometry analysis.

Enzyme-linked immunosorbent assay (ELISA):

PSC1d cells were seeded and treated with 390 μM ATP and cytokines for 6 hours, and condition media was obtained by collecting supernatant after centrifugation. IL-6 protein levels in the condition media were quantified by Mouse IL-6 ELISA Kit (Abcam, ab 100712). Similarly, CXCL1 protein levels were quantified by ELISA MAX™ Deluxe Set Mouse CXCL1 (BioLegend, 447504), and LIF was quantified by Quantikine ELISA Mouse LIF Immunoassay (R&D Systems, MLF00), all following the manufacturer's instructions. Absorbance in experimental wells was converted to absolute cytokine concentration calculated based on standard curve, and after calculation any values below zero were set to zero.

Quantification of gene expression:

Total RNA was purified from cultured cells using TRIzol reagent (Ambion, 15596026), and 1 μg of cDNA was synthesized from total isolated RNA using iScript cDNA Synthesis Kit (Bio-Rad, 1708891) per manufacturer's instructions. qPCR analysis was performed in biological triplicates using 1:50 diluted cDNAs and 0.1 μM forward and reverse primers together using iTaq Universal SYBR Green Supermix (Bio-Rad, 1725121) on a QuantStudio 7 Flex (Applied Biosystems). Geometric mean of the endogenous control genes mouse *Actb* and *Hmbs* were used as reference samples. Primer pair sequences are as follow:

m*Rplp0*: F-AGATTCGGGATATGCTGTTGGC; R-TCGGGTCCTAGACCAGTGTTC.

m*Actb*: F-CGTGAAAAGATGACCCAGATCA; R-CACAGCCTGGATGGCTACGT.

m*Hmbs*: F-ATGAGGGTGATTCGAGTGGG; R-TTGTCTCCCGTGGTGGACATA.

m*IL6*: F-CTTCCATCCAGTTGCCTTCT; R-CTCCGACTTGTGAAGTGGTATAG.

m*Cxcl1*: F-GTGTCAACCACTGTGCTAGT; R-CACACATGTCCTCACCCTAATAC.

m*Lif*: F-CTGCTCTCCCTCTTTCCTTTC; R-ACATTCCCACAGGGTACATTC.

m*Acta2* (*aSMA*): F-CCATCATGCGTCTGGACTT; R-GGCAGTAGTCACGAAGGAATAG.

m*Tgfb1*: F-CTTCCCGAATGTCTGACGTA; R-GACCGCAACAACGCCATCT.

m*Col1a1*: F-ACTGCAACATGGAGACAGGTCAGA; R-ATCGGTCATGCTCTCTCCAAACCA.

m*Fn1*: F-GGCCACACCTACAACCAGTA; R-TCGTCTCTGTCAGCTTGCAC.

m*Ccn2*: F-TGACCTGGAGGAAAACATTAAGA; R-AGCCCTGTATGTCTTCACACTG.

h*IL6*: F-GGAGACTTGCCTGGTGAAA; R-CTGGCTTGTTCCTCACTACTC.

h*CXCL1*: F-GGAACAGAAGAGGAAAGAGAGAC; R-TCTCCTAAGCGATGCTCAAAC.

h*LIF*: F-ATAGGGAGGGAGCTAGAAGAAG; R-GGCCAAAGGGACAAGTAGAG.

h*HMBS*: F-GGCCAAAGGGACAAGTAGAG; R-GGGTACCCACGCGAATCAC.

h*ACTB*: F-CTGGAACGGTGAAGGTGACA; R-AAGGGACTTCCTGTAACAATGCA.

Flow cytometry:

PSC1d cells were trypsinized, washed, and stained with eBioscience™ Fixable Viability Dye eFluor™ 780 (1:1000; Invitrogen, 65-0865-14) in PBS for 20 mins at 4 degrees in the dark for discriminating viable cells. Next, cells were washed with FACS buffer (PBS supplemented with 3% FBS) and stained in FACS buffer with Brilliant Violet 421™ anti-mouse Ly-6C Antibody (1:800; BioLegend, 128031) for 30 mins at 4 degrees in the dark. Samples were washed and analyzed on NovoCyte Quanteon (Agilent), and data was analyzed using FlowJo v10.4.

For isolated tumor cells, cells were treated with TruStain FcX™ (anti-mouse CD16/32) Antibody (BioLegend, 101319), Ghost Dye™ Violet 510 (CYTEK, SKU 13-0870-T500), FITC-EpCAM (1:100), Brilliant Violet 785™ anti-mouse I-A/I-E Antibody (1:800; BioLegend,

107645), PE/Cyanine5 anti-mouse Ly-6G/Ly-6C (Gr-1) Antibody (1:800; BioLegend, 108409), Brilliant Violet 711™ anti-mouse CD45 Antibody (1:800; BioLegend, 103147), Brilliant Violet 421™ anti-mouse Ly-6C Antibody (1:800; BioLegend, 128031), PE/Cyanine7 anti-mouse CD31 Antibody (1:1000; BioLegend, 102417), APC anti-mouse CD140a Antibody (BioLegend, 135907), BV605- F4/80 (1:400), AF700-CD11b (1:1000), PerCP/Cy5.5-PDPN (1:800), APC/Cy7-CD8 for 30 minutes at 4 degrees. Then, cells were fixed for 30 minutes at room temperature followed by permeabilization. Cells were further stained intracellularly by Human Alpha-Smooth Muscle Actin PE-conjugated Antibody (1:400; Biotechne, IC1420P), AF488-panCK (1:100), and analyzed on a Fortessa 4-15 at UChicago cytometry and antibody technology core facility, and data was analyzed using FlowJo v10.4.

Serum starvation:

PSC1d cells were seeded the evening before the experiments and changed into 0.5% FBS the next morning. After 6 hours of serum starvation, treatments were added in 0.5% FBS for another 24 hours. Cells were then collected for subsequent analysis.

Phospho-Kinase Array:

PSC1d cells were seeded before the experiments, and ATP and cytokines were added for 1 hour, followed by protein extraction and array analysis using Proteome Profiler Phospho-Kinase Array Kit (R&D Systems, ARY003C) following the manufacturer's instructions. The quantification for pixel density in each spot of the array was carried out by subtracting background signals from the spot intensity using software ImageJ (ImageJ, RRID: SCR_003070).

Immunoblotting and antibodies:

For all western blot experiments, protein lysates were prepared using RIPA cell lysis buffer (Millipore Sigma, 20-188) supplemented with protease inhibitors (Millipore Sigma, 59813300) and incubated on ice for 30 minutes. Protein lysate was quantified using Pierce™ BCA Protein Assay Kits (Thermo Fisher Scientific, 23225) and denatured with Laemmli SDS sample buffer (Thermo Fisher Scientific, J61337). A total of 20 to 30 µg of protein was loaded into wells of homemade SDS-PAGE gel along with molecular weight markers (Thermo Fisher Scientific, 26616). Gel was run at 110V for 1–2 hours. Resolved proteins were then transferred onto a nitrocellulose membrane by wet transfer. After transfer, membrane was blocked in TBST with 5% skimmed milk for 1 hour and probed with relevant primary and secondary antibodies in TBST with 5% skimmed milk. The following primary antibodies were used: Rabbit monoclonal anti-GAPDH antibody (1:15,000 dilution, Cell Signaling Technology, 2118S, RRID: AB_561053), Mouse monoclonal anti-β-actin antibody (1:5000, Sigma-Aldrich, A1978, RRID: AB_476692), pSTAT3 Tyr705 (1:1000, Cell Signaling Technology, 9131L, RRID: AB_331586), STAT3 (1:1000, Cell Signaling technology, 9139, RRID: AB_331757), GFP (1:1,000, Sigma, 11814460001, RRID:AB_390913). p65 (1:1,000, Cell Signaling Technology, 8242S, RRID:AB_331757), Lamin A/C (1:1,000, Cell Signaling Technology, 4777, RRID:AB_10545756).

The following secondary antibody was used: Goat anti-Mouse IgG (HþL) Secondary Antibody, HRP (1:5000 dilution, Thermo Fisher Scientific, 31430, RRID: AB_228307), Goat anti-Rabbit IgG (HþL) Secondary Antibody, HRP (1:5000 dilution, Thermo Fisher Scientific, 31460, RRID: AB_228341). HRP was detected by chemiluminescence by Clarity Western ECL Substrate (Bio-Rad, 1705061) by a film developer.

Cytoplasmic and nuclear protein fraction preparation:

PSC1d cells were seeded in 6-well plate the day before the experiments, and ATP and cytokines were added for 1 hour. Cells were washed with ice cold PBS and lysed with 100 µl harvest buffer (10 mM HEPES-KOH pH 7.9, 50 mM NaCl, 0.5 M Sucrose, 0.1 mM EDTA, 0.5% Triton X-100, protease inhibitors) for 5 minutes on ice. Next, cells were scraped, collected, and centrifuged at 500g for 5 minutes at 4 degrees. Supernatant was saved as cytoplasmic/membrane protein fraction.

Then, pellet was resuspended with 500 µl buffer A (10 mM HEPES-KOH pH 7.9, 10 mM KCl, 0.1 mM EDTA, 0.1 mM EGTA) and centrifuged immediately at 500g for 5 minutes at 4 degrees. Supernatant was carefully removed, and pellet was lysed in 50 µl buffer C (10 mM HEPES-KOH pH 7.9, 500 mM NaCl, 0.1 mM EDTA, 0.1 mM EGTA, 0.1% NP-40) for 10 minutes on ice, followed by 10,000g 5 minutes centrifugation at 4 degrees. Finally, supernatant was collected as nuclear protein fraction.

Cytosolic calcium flux detection:

12.5k PSC1d cells were seeded per well in black-edge, clear-bottom 96-well plates (Corning, 353219) the evening before experiments. Next day, cells were loaded with 2 µM Fura-2 AM (ThermoFisher Scientific, F1221) and 10 µM BAPTA-AM (Cayman, 15551) in serum-free DMEM at 37 degree for 30 minutes in the dark. Then, cells were washed three times with calcium-free Ringers (Concepcion et al. 2022) and F340/F380 absorbance was analyzed on FlexStation3 multimode microplate reader (Molecular Devices). During analysis, 390 µM of ATP, 1 mM Ca^{2+} containing Ringers, and 1 µM ionomycin (all final concentrations) were injected sequentially for real time cytosolic calcium flux analysis.

RNA-sequencing and gene set enrichment analysis (GSEA):

PSC1d cells were treated with ATP and cytokines for 1 hour, 6 hour, 24 hours, and sample triplicates were collected and followed by RNA extraction using the TRIzol reagent (Ambion, 15596026) per the manufacturer's instructions. The extracted RNA was treated with Invitrogen DNA-free DNA Removal Kit (Invitrogen, AM1906) to remove excess DNAs per manufacture's instructions. At least 500 ng of extracted RNA per sample was sent to Novogene for sequencing and bioinformatics analysis. RNA sequencing was performed via Illumina Next-Generation Sequencing. Fragments were aligned with HISAT2 to reference genes, and differential gene-expression analysis was performed by DESeq. The list of differential expressed genes was filtered by "protein_coding", and the average counts that are less than 20 are filtered out. GSEA was performed by entering pre-ranked gene fold change data (.rnk file) into the tool "Run GSEAPreranked" in the GSEA software (Broad Institute, GSEA 4.3.3) matching mh.all.v2023.2.Mm.symbols gene set database.

Statistical analysis:

Statistical analysis for all experimental data is included in the figure legends, with sample size and type of analysis indicated. P values less than or equal to 0.05 is considered as significant: ns, not significant; *, $P \leq 0.05$; **, $P \leq 0.01$; ***, $P \leq 0.001$.

3.3 Results

A blood chemical screen identified ATP as metabolite that potentiates the cytokine induced inflammatory CAF state.

We previously developed a novel fibroblast reporter (FIRE) system (Schwörer et al. 2023) to rapidly assess the CAF states in response to perturbations. The FIRE system features both myofibroblastic CAF (*SMA*-DsRed) and inflammatory CAF (*IL6*-EGFP) transcriptional reporters and adequately indicates CAF state transitions by fluorescence readings in response to established modulators of the CAF state (TGFβ for the myCAF state, and cytokines and the hypoxia mimetic $CoCl_2$ for the iCAF state) (Fig. 3.1A). We calculated a Z-factor of 0.8, indicating the suitability of the assay for high-content screening (J. H. Zhang, Chung, and Oldenburg 1999).

To identify extracellular metabolic factors that regulate the CAF state, we used PSCs, the CAF precursors in PDAC tumors (Helms, Onate, and Sherman 2020), expressing FIRE to screen a library of metabolites that are present both in blood and in tumors (Fan et al. 2023). Out of 255 metabolites, various purines promote FIRE changes towards an iCAF-like state (negative FIRE score) in the presence of cytokines or TGFβ (Fig. 3.1B). Intriguingly, we found that the top hit, ATP, can blunt TGFβ-induced αSMA expression in a time-dependent manner (Fig. 3.1C) while promoting cytokines (IL-1α/LIF/TNFα)-induced *IL6* expression both time- and dose-dependently (Fig. 3.1D).

To further validate the effect of ATP in potentiating the cytokine-induced iCAF state, we examined more iCAF markers, *Cxcl1* and *Lif*, and verified the *IL6* mRNA levels directly. In two mouse PSC cell lines (Fig. 3.2A&3.2B), mouse primary lung fibroblasts (Fig. 3.2C), and in human primary lung CAFs (Fig. 3.2D), ATP treatment synergizes with cytokines in stimulating

Cxcl1, Lif, and IL6 gene expression. Further, analysis of conditioned media from PSCs shows that ATP and cytokines synergistically upregulate mouse IL-6 (Fig. 3.2E), CXCL1 (Fig. 3.2F), and LIF (Fig. 3.2G) protein levels. Moreover, we tested another iCAF marker, Ly6C, and flow cytometry shows that ATP treatments promotes both *IL6* and Ly6C expression and synergizes with cytokines (Fig. 3.2H-3.2K). Consistently, pretreatment of PSCs with ATP in culture (Fig. 3.2L) was sufficient to decrease myCAF to iCAF ratios in tumors (Fig. 3.2M) and increase their tumor-promoting properties (Fig. 3.2N) after subcutaneous co-injection with KPC cells.

Altogether, these data indicate that eATP can potentiate an inflammatory CAF state in combination with cytokines and increase the tumor-promoting properties of PSCs.

The iCAF state-promoting effect of ATP is not mediated through purinergic receptors. ATP is an intracellular energy carrier, while eATP is an important extracellular signaling molecule and one of its most established pathways is through binding purinergic receptors (Di Virgilio et al. 2018). Thus, we sought to explore this classical eATP signaling pathway for its role in mediating the effect of eATP on the CAF state.

There are two major outcomes downstream of purinergic signaling activation: intracellular calcium flux and cAMP-CREB pathways (Woods et al. 2021). Indeed, eATP triggers an immediate cytosolic calcium response, and such calcium response can be repressed by pretreatment with intracellular calcium chelator BAPTA-AM (Fig. 3.3A). However, repressing the intracellular calcium flux does not increase the FIRE score after eATP treatment (Fig. 3.3B). This indicates that, although eATP can trigger a calcium response, the calcium response is not responsible for eATP's effect in inducing an iCAF-like state in PSCs. Also, perturbing the cAMP-CREB pathway by PKA or CREB inhibition does not affect the FIRE

score decreased by eATP (Fig. 3.3C, 3.3D). These data indicate that purinergic receptor pathways do not explain ATP's effect on promoting an iCAF-like state, suggesting a purinergic receptor unrelated mechanism. To confirm, we inhibited selected purinergic receptors based on their mRNA expression from our previous RNAseq (Schwörer et al. 2023) (data not shown). Inhibiting P2X4, P2X7, P2Y1, P2Y2, or P2Y6 does not affect eATP-mediated induction of an iCAF state (Fig. 3.3E-3.3I). UTP is the preferred agonist of P2Y2 and P2Y4, UDP is of P2Y6, and UDP-glucose is of P2Y14 (Di Virgilio et al. 2018). Treating cells with the same or double the concentrations of UTP, UDP, UDP-glucose does not induce an iCAF-like state in PSCs in comparison to ATP (Fig. 3.3J-3.3K). Altogether, although eATP can trigger purinergic receptor responses (such as calcium flux), our data suggest that purinergic receptor signaling may not mediate eATP's impact in promoting an iCAF-like state in PSCs.

At least one phosphate group is required for eATP's effect in inducing an iCAF state, and it is independent of pH change.

To further explore the mechanism of eATP effect on PSCs, we examined multiple ATP derivatives, including ADP, AMP, adenosine, and adenine. We also included a non-hydrolysable ATP analog, ATPγS. ATP, ATPγS, ADP, and AMP, but not adenosine nor adenine, can increase *IL6* and Ly6C protein levels alone and synergize with cytokines (Fig. S3.1A). This indicates that adenosine with at least one phosphate group is needed to promote an iCAF-like state in PSCs. ATPγS findings further indicate that ATP does not need to be degraded to mediate its effect on PSCs. Since ATP has hydrolysable triphosphate groups, we examined if there is a change in media pH at the concentration that can induce an iCAF state. Results show that, adding ATP, ATPγS, ADP, AMP, adenosine, or adenine does not significantly change media pH (Fig. S3.1B).

Moreover, altering media pH by NaOH or HCl does not increase *IL6*-EGFP levels (Fig. S3.1B, S3.1C).

Altogether, for eATP and its derivatives to promote an iCAF-like state, at least one phosphate group is required, and the effect is independent of pH change in the media and does not require ATP hydrolysis.

eATP effect in promoting an iCAF state is through JAK-STAT3 pathway.

eATP can promote the iCAF state within a few hours (Fig. 3.1D), this prompted us to investigate other potential signaling roles of eATP. PSCs were treated with ATP and/or cytokines for 1 hour, and multiple phosphorylation pathways were resolved simultaneously by a phospho-kinase array (Fig. 3.4A, 3.4B). STAT3 phosphorylation at site Y705 increases almost forty times upon ATP treatment and is further increased together with cytokines (Fig. 3.4A, 3.4B). To confirm these findings, after 1-hour ATP and cytokine treatments, nucleus and cytosol proportions were isolated from PSCs, and STAT3 activity as well as p65 levels were resolved by immunoblotting. p65 is a key component of the NF-*k*B pathway, which has previously been reported, along with the JAK-STAT3 pathway, to be the two key effector iCAF pathways (Biffi et al. 2019). Consistent with the phospho-kinase array results, ATP alone increases STAT3 phosphorylation, and this further increases upon cytokine stimulation (Fig. 3.4C). However, there is no change of nuclear p65 levels upon ATP treatment (Fig. 3.4C), suggesting that ATP does not activate NF-*k*B signaling. In addition, we performed RNA-Seq on 6-hour (Fig. 3.4D) and 24-hour (Fig. 3.4E) of ATP and cytokines treatment. Using GSEA, we found that consistently, after 6 hours of treatments, IL-6-JAK-STAT3 pathway is upregulated by ATP alone compared to untreated

PSCs, or by ATP and cytokines compared to cytokines alone (Fig. 3.4D); while after 24 hours of treatments, the Hallmark inflammatory pathway is upregulated (Fig. 3.4E).

To test if JAK-STAT3 signaling is indeed critical for ATP's effect, a potent JAK2 inhibitor was applied, which has previously been validated to effectively abrogate pSTAT3 levels in PSCs (Schwörer et al. 2023), along with ATP for 24 hours. Results show that, upon ATP treatment there is an increase in *IL6* and Ly6C levels, and the effect completely disappears with JAK inhibition (Fig. 3.4F).

Altogether, these data show that, upon ATP treatment, STAT3 is activated, and inhibition of JAK2 blocks ATP's effect in inducing Ly6C and *IL6.* This indicates that ATP promotes an iCAF-like state through the JAK-STAT3 pathway.

ATP promotion of an iCAF state is serum dependent.

Since the JAK-STAT pathway can be activated by both cytokines and growth factors (X. Hu et al. 2021), we removed cytokines and growth factors from the media by serum starvation to test whether ATP was still effective under these conditions. Cells were serum starved in 0.5% FBS for 6 hours, and ATP was added for another 24 hours in 0.5% FBS. Intriguingly, ATP no longer increases *IL6* nor Ly6C expression after serum starvation to the same extend as in 10% FBS (Fig. 3.5A, 3.5B), suggesting that ATP's effect in promoting an iCAF state is serum dependent.

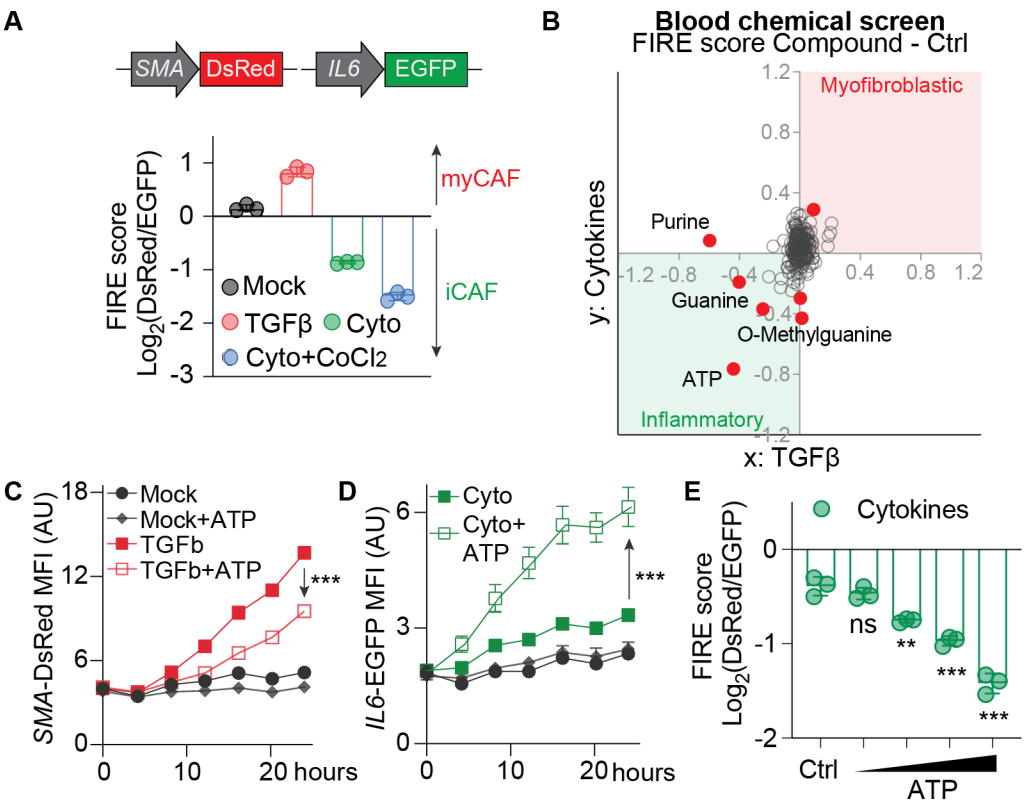

Figure 3.1

ATP is the top candidate from the blood chemical screen that potentials an inflammatory CAF state. A, Fibroblast reporter (FIRE) score calculated out of fluorescence of transcriptional reporters *SMA*-DsRed and *IL6*-EGFP measured on Incucyte, with 2 ng/ml TGFβ, cytokines (2 ng/mL murine IL-1*a*, TNF*a*, and LIF), or 100 µM cobalt chloride ($CoCl_2$). B, Summary of blood chemical screen plotted on FIRE of candidates subtracted by FIRE of control, and red dots highlights the candidates that have an adjusted p-value less than 0.05 and a fold change over 20%. Time course transcriptional reporters (C) *SMA*-DsRed, (D) *IL6*-EGFP fluorescence measurement on Incucyte after adding 390 µM ATP, 2 ng/ml TGFβ, and cytokines on time 0. E, FIRE score of PSC1d cells after 24-hour treatment with 0, 156, 390, 780, 1560 µM dose-increasing ATP and cytokines, and p values are relative to the control condition.

(continued)

Error bars indicate means ± SD (N = 3 biological replicates). P values were calculated using two-tailed, unpaired Student t test (ns, not significant; *, $P \leq 0.05$; **, $P \leq 0.01$; ***, $P \leq 0.001$).

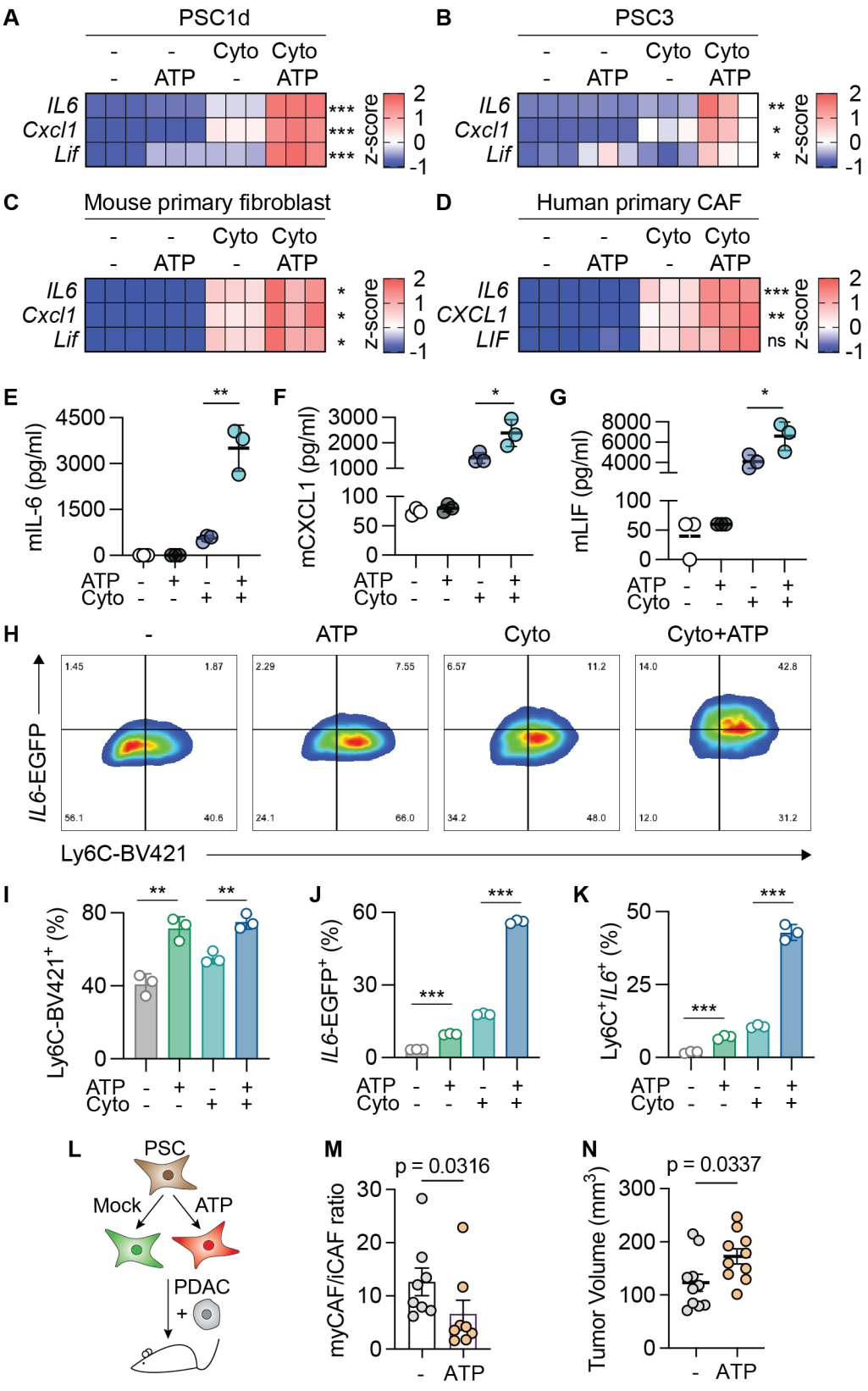

Figure 3.2 Validation of eATP effect in potentiating iCAF state and affecting tumor growth. A-D, mRNA levels of (A) PSC1d cells, (B) PSC3 cells, (C) mouse primary lung fibroblasts, and (D) human primary lung CAFs after 24-hour of ATP and cytokines treatment by RT-qPCR. All qPCRs are

(continued)

N = 3 biological replicates, and statistic comparison is performed on cytokines versus cytokines with ATP. E-G, IL-6 (E), CXCL1 (F), LIF (G) protein secretion detected in PSC1d conditional media after 24-hour ATP and cytokines treatment by ELISA. N = 3 biological replicates. H-K, Flow cytometry on PSC1d after 24-hour ATP and cytokine treatment, and *IL6* and Ly6C are shown and quantified in (I)-(K). L-N, PSC1d cells were pretreated with eATP for 24 hours and subcutaneously co-injected with KPC cells into mice for 20 days, N = 10 mice. (L) Schematic diagram of the coinjection experiment; (M) Endpoint myCAF/iCAF ratio; (N) Endpoint tumor volume. All error bars indicate means ± SD, and p values were calculated using two-tailed, unpaired Student t test (ns, not significant; *, $P \leq 0.05$; **, $P \leq 0.01$; ***, $P \leq 0.001$).

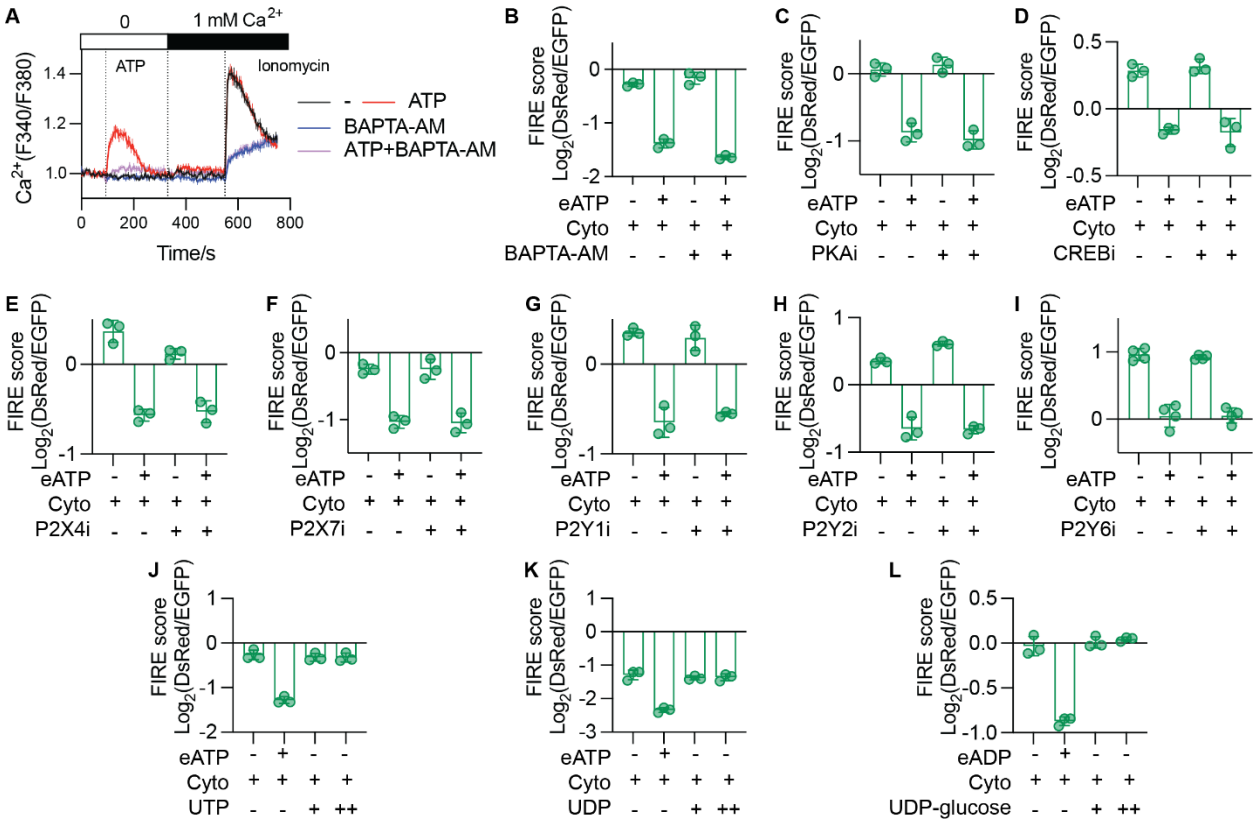

Figure 3.3

The iCAF state-promoting effect of ATP is not mediated through purinergic receptors. A, Cytosolic calcium flux in PSC1d cells upon acute eATP treatment analyzed on FlexStation3; B-I, FIRE score of PSC1d cells analyzed on Incucyte after 24-hour treatment with 390 μM eATP and cytokines, (B) 10 μM BAPTA-AM, (C) 200 nM PKAi (H89), (D) 200 nM CREBi (666-15), (E) 10 μM P2X4i (5-BDBD), (F) 10 μM P2X7i (AZ10606120), (G) 10 μM P2Y1i (MRS2179), (H) 10 μM P2Y2i (AR-C 118925XX), or (I) 10 μM P2Y6i (MRS2578). J-L, FIRE score of PSC1d cells analyzed on Incucyte after 24-hour treatment with ATP and cytokines, (J) UTP, (K) UDP, or (L) UDP-glucose (+, 390 μM; ++, 780 μM).

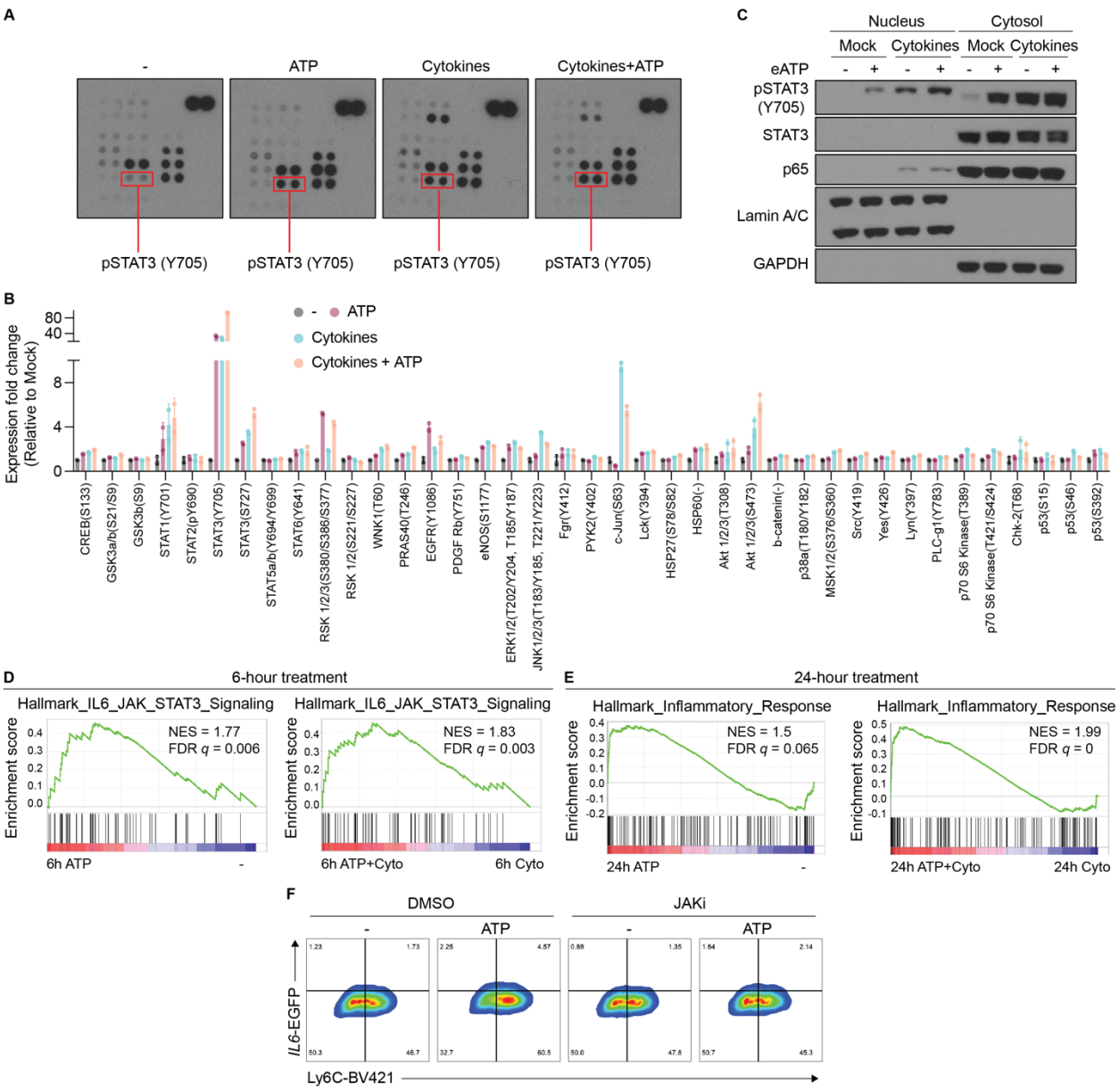

Figure 3.4

eATP effect in promoting an iCAF state is through JAK-STAT3 pathway. A, Signaling pathway analysis by a phospho-kinase array in PSC1d cells treated with eATP and cytokines for 1 hour, and pSTAT3 is highlighted. B, Quantification of phospho-kinase array and all relative to their own mock levels. C, p-STAT3, STAT3, p65 levels in isolated nucleus and cytosol of PSC1d cells after 1-hour ATP and cytokines treatment by immunoblotting. D-E, GSEA

(continued)

analysis from RNA-Seq on (D) 6-hour ATP and cytokines treatment and (E) 24-hour ATP and cytokines treatment. $N = 3$ biological replicates. F, *IL6* and Ly6C levels in PSC1d cells after 24-hour treatment with ATP, cytokines, and 2 μM JAK2 inhibitors by flow cytometry.

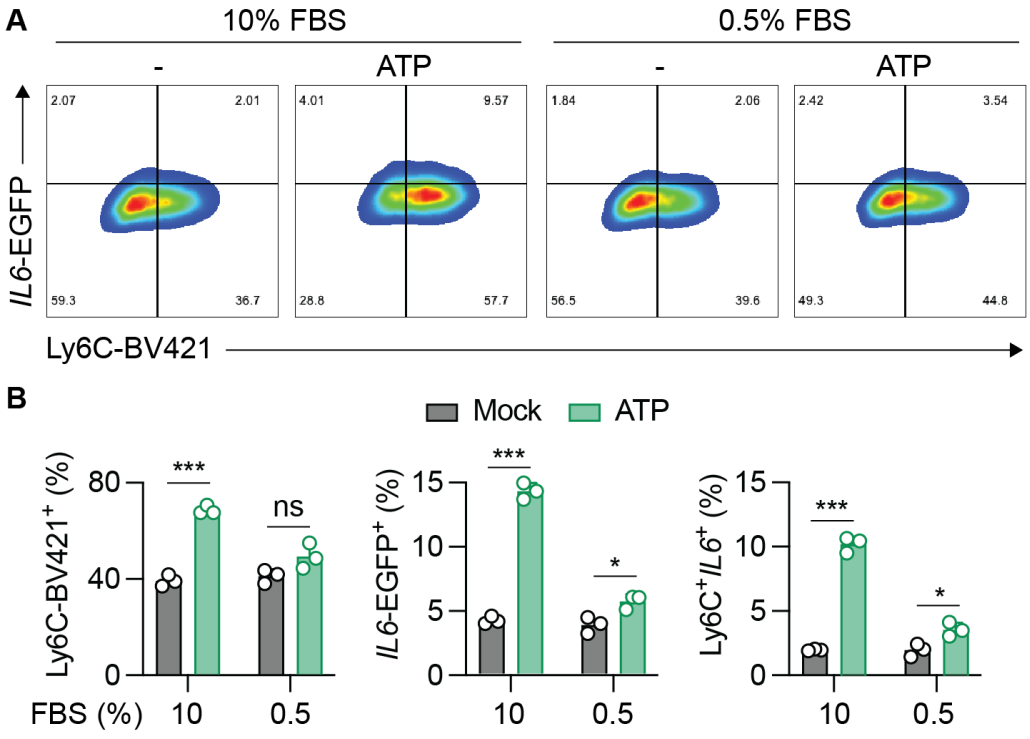

Figure 3.5

ATP promotion of an iCAF state is serum dependent. A, *IL6* and Ly6C levels in PSC1d cells after 24-hour treatment with ATP and cultured in 10% or 0.5% FBS. B, Quantification of percentage Ly6C positive, *IL6* positive, and double positive cells in (A).

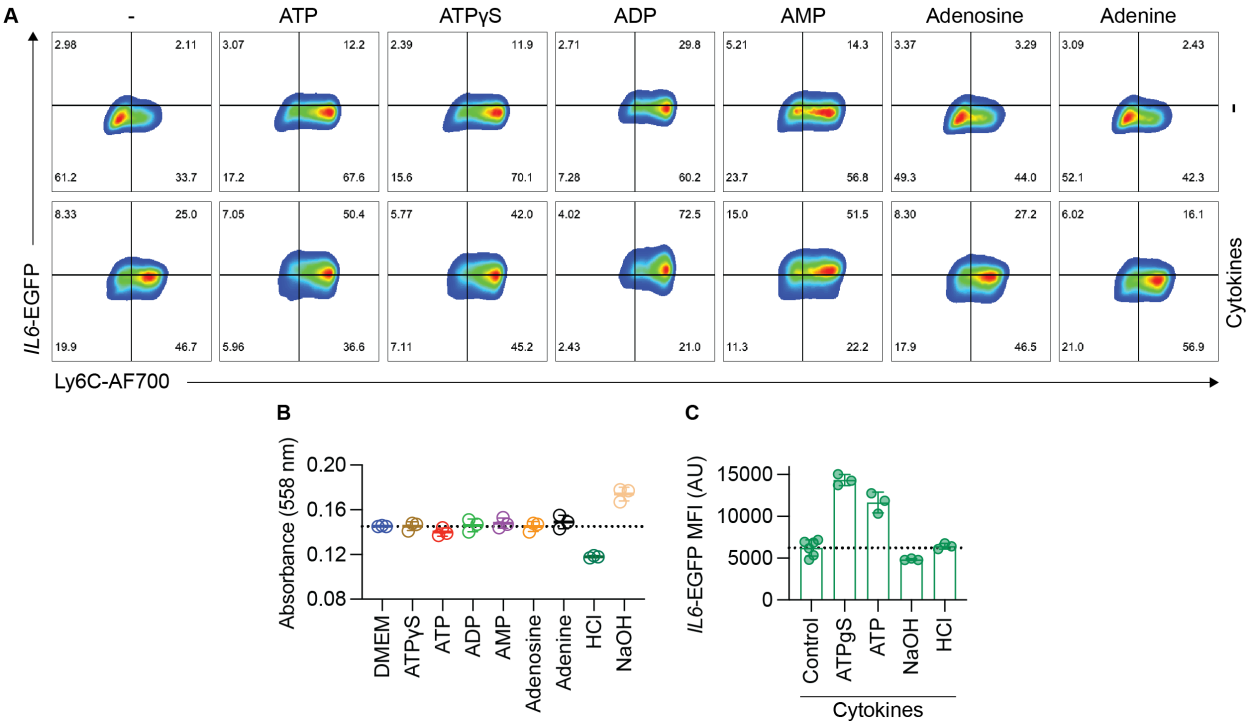

Figure S3.1

At least one phosphate group is required for eATP effect in inducing an iCAF state, and it's independent of media pH change. B, Phenol red absorbance measured at 558 nm by plate reader for DMEM based media immediately after adding 390 µM ATPγS, ATP, ADP, AMP, adenosine, adenine; HCl, or NaOH. C, *IL6*-EGFP fluorescence levels measured on Incucyte after 24-hour treatment with 390 µM ATPγS, or ATP; HCl or NaOH. Data in A was generated by Dr. Simon Schwörer.

3.4 Discussion

ATP accumulation in the TME is a feature of many other solid tumors, such as human melanoma and ovarian carcinoma (Pellegatti et al. 2008), and was ATP also accumulates in PDAC (L.-P. Hu et al. 2019). Similarly, CAF heterogeneity is also observed across various malignancies (Biffi and Tuveson 2021). That is to say, the findings of this study have the potential to be applied to wide range of solid tumors. This idea is further supported by our observation that eATP synergizes with cytokines not only in PSCs but also lung fibroblasts and CAFs (Fig. 3.2 C-D). Moreover, chemotherapy is a standard of care for human PDAC patients, and chemotherapy can induce cell death, a major source of extracellular ATP. Does chemotherapy prompt CAFs to an iCAF state? Do iCAFs secrete inflammatory factors and may make cancer cells relapse? Would a combination of chemotherapy and iCAF targeting be beneficial for PDAC treatments? These are the questions that are potentially interesting for future studies.

Since we saw eATP promotes an iCAF state in a serum dependent manner (Fig. 3.5), future experiments will need to resolve the contributions of individual growth factors and cytokines from the serum, based on reported serum components (Lee et al. 2022). This will shed light on eATP's mechanism. For example, if there is one major contributor from the serum that eATP is dependent on to induce the iCAF state, eATP's effect may be mediated through its receptor or downstream effectors. Moreover, since the JAK2 inhibitor can abrogate the eATP effect, the activity of more JAK isoforms should be tested to figure out the exact JAK isoform be affected, which can also help to narrow down the exact mechanism.

At this stage, we cannot rule out the possibility that eATP enters the cell and functions intracellularly. If we are not able to identify cell surface proteins mediating the combined effect of eATPs and cytokines, a whole-genome CRISPR/Cas9 screen will be performed. In addition,

we haven’t tested by ourselves if the PKA and CREB inhibitors are functional at the concentrations we used. We also cannot rule out that eATP enters the cell and acts intracellular.

CHAPTER 4: DISCUSSION AND FUTURE DIRECTIONS

4.1 Calcium levels in the ER may also be oncogene dependent.

Our finding highlights the critical role of ER calcium homeostasis for cancer cell proliferation and survival (Sehgal et al. 2017; Preissler et al. 2020; Ibarra et al. 2022; Krebs, Agellon, and Michalak 2015; Luo and Lee 2013; Bahar, Kim, and Yoon 2016), and that the sustained UPR can trigger cell apoptosis (Sano and Reed 2013) (Figure 4.1).

Moreover, we not only observed changes in ER calcium before and after AHCYL1 deficiency but also there are differences in cellular basal ER calcium levels: in *NRAS*-mutated human melanoma cell HMCB, the basal ER calcium is significantly higher than *BRAF*-mutated melanoma cell A375 (Fig. 2.3C). This observation raises the question of whether basal ER calcium levels vary across cell types and whether such variation is oncogenic background dependent. Particularly, *NRAS*-mutated melanoma has been reported to be more sensitive to intracellular calcium alterations than *BRAF*-mutated melanoma (Esteves et al. 2020). Intriguingly, we also noted that HMCB cells were larger in size than A375, suggesting greater cell growth and more extensive protein synthesis and folding in *NRAS*-mutated HMCB cells.

Future studies will explore whether cell growth and size can be oncogene-dependent and whether they correlate with basal ER calcium levels and protein folding requirements.

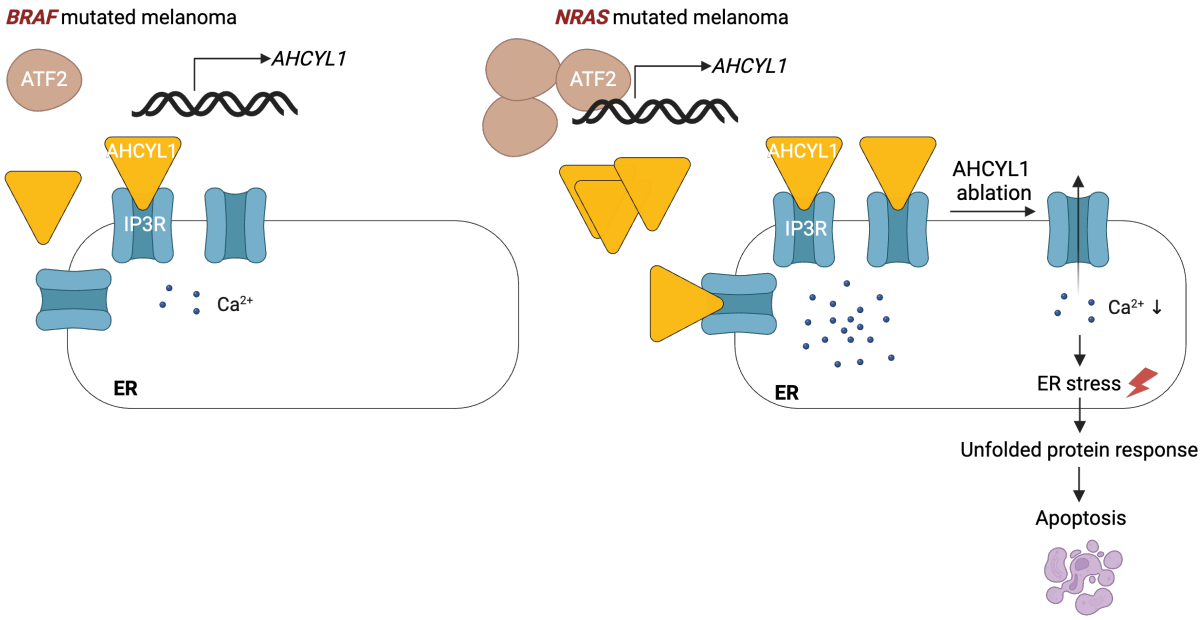

Figure 4.1 Schematic of *NRAS*-dependent AHCYL1 requirement in human melanoma (created with BioRender.com).

4.2 Our findings reinforce the idea that there are oncogene specific metabolic alterations.

Over the past decade, our research group and others elucidated multiple oncogene-specific metabolic regulations (Xia et al. 2017; Kang et al. 2015; Gao et al. 2022; Zhao et al. 2017; Lin et al. 2018; Min and Lee 2018; Tarrado-Castellarnau, de Atauri, and Cascante 2016). We have found that the ketogenic enzyme HMG-CoA lyase (HMGCL) is selectively essential in melanoma cells expressing *BRAF V600E*, where its product acetoacetate promotes *BRAF V600E*-dependent MEK1 activation (Kang et al. 2015; Xia et al. 2017; Zhao et al. 2017). Moreover, we demonstrated that chondroitin-4-sulfate (CHSA), a circulating dietary supplement, exhibits intracellular signaling function by enhancing casein kinase II (CKII)-PTEN binding, leading to

PTEN inhibition and subsequent AKT activation, which are crucial for cancers expressing *BRAF V600E* (Lin et al. 2018). We also reported that Phospholipase A2, group VII (PLA2G7) and Lyso-PAF act as key elements of RAS-RAF1 signaling and exhibit intracellular signaling functions (Gao et al. 2022).

Here, our study on AHCYL1 (Cai et al. 2024) further adds to this knowledge and demonstrates the concept of oncogene-specific calcium regulations in cancer cells, and sheds light on oncogene-mediated metabolic rewiring in cancer cells compare to normal cells, providing new insights in development of novel precision medicine for cancer treatment (Hanahan 2022).

4.3 What is the potential of targeting AHCYL1 for clinical treatments?

Despite the ever-present challenge to target oncogenes directly, our research reinforces the idea of targeting oncogene synthetic lethal partners. We identified AHCYL1 is overexpressed in *NRAS*-mutant expressing human melanoma cells, and it is selectively critical. AHCYL1 can be a promising target for *NRAS* mutated human melanoma treatments.

Based on data on healthy human tissues from human protein atlas, AHCYL1 expression is medium to low across all healthy tissues and organs, indicating it may be a relative safe target, especially considering the fact that even in melanoma, there is differential expression levels of AHCYL1 that is oncogene dependent (Figure 4.1).

4.4 Where does eATP come from?

eATP has been found to accumulate at high micromolar levels in the TME comparing to healthy tissues (Pellegatti et al. 2008; L.-P. Hu et al. 2019). However, where does it come from?

eATP can accumulate in the TME due to cell apoptosis and dead cells, in addition, cells under hypoxia and stress can also release ATP without cell injury (Di Virgilio et al. 2018). Given the fact that PDAC has necrotic centers and hypoxic regions as discussed in chapter 1.6, eATP might further contribute to the iCAF accumulation at PDAC hypoxic regions (Schwörer et al. 2023). Intriguingly, a recent study also found that macrophages can release ATP under hypoxia conditions (Bhattacharyya et al. 2022), and macrophages are the major immune population in the PDAC TME (Poh and Ernst 2021). Altogether, ATP accumulation in the PDAC TME may derive from: (1) necrotic center and dead cells; (2) Hypoxia causing cell stress making cells release ATP from their intracellular stock; (3) Macrophages in hypoxia regions.

While eATP accumulation in the PDAC has been measured previously, we need to measure and validate eATP accumulation in the PDAC TME ourselves, in particular in the mouse models used to determine the effect of eATP pretreatment on tumor growth and the accumulation of iCAFs in the hypoxic tumor regions. We have obtained a P2Y1-based extracellular ATP sensor from Addgene, GRAB_ATP1.0 (Wu et al. 2022), and have engineered it into lentiviral backbone with the help of Sayana Isaac and Nicole Liu (undergraduate students from the Schwörer Lab) for later stable expression. After confirming the sequence is correct, we will stably express it in our PDAC cancer cell lines. Then, we will first test the sensitivity of this sensor *in vitro*, by adding titrations of eATP and detecting EGFP and mCherry fluorescence. The EGFP fluorescence is hypothesized to rise with increasing concentrations of eATP, and is normalized to mCherry fluorescence to account for the expression levels of the sensor. The

ultimate goal is to inject GRAB_ATP1.0_PDAC cells together with PSCs into mice and record fluorescence, comparing to healthy mouse pancreas. This will help us understand: (1) is ATP accumulating in the PDAC TME comparing to healthy pancreas; (2) is ATP accumulating at certain regions of a PDAC tumor, for example, hypoxia by pimonidazole staining, or near macrophages.

Not only for PDAC, ATP accumulation in the TME is a feature of many other solid tumors, such as human melanoma and ovarian carcinoma (Pellegatti et al. 2008). Similarly, CAF heterogeneity is also observed across various malignancies (Biffi and Tuveson 2021). That is to say, the findings of this study have the potential to be applied to wide range of solid tumors. Moreover, chemotherapy is a standard of care for human PDAC patients, and chemotherapy can induce cell death, a major source of extracellular ATP. Does chemotherapy prompt CAFs to an iCAF state? Do iCAFs secrete inflammatory factors and may make cancer cells relapse? Would a combination of chemotherapy and iCAF targeting be beneficial for PDAC treatments? These are all questions from a bigger picture and imply therapeutic potential.

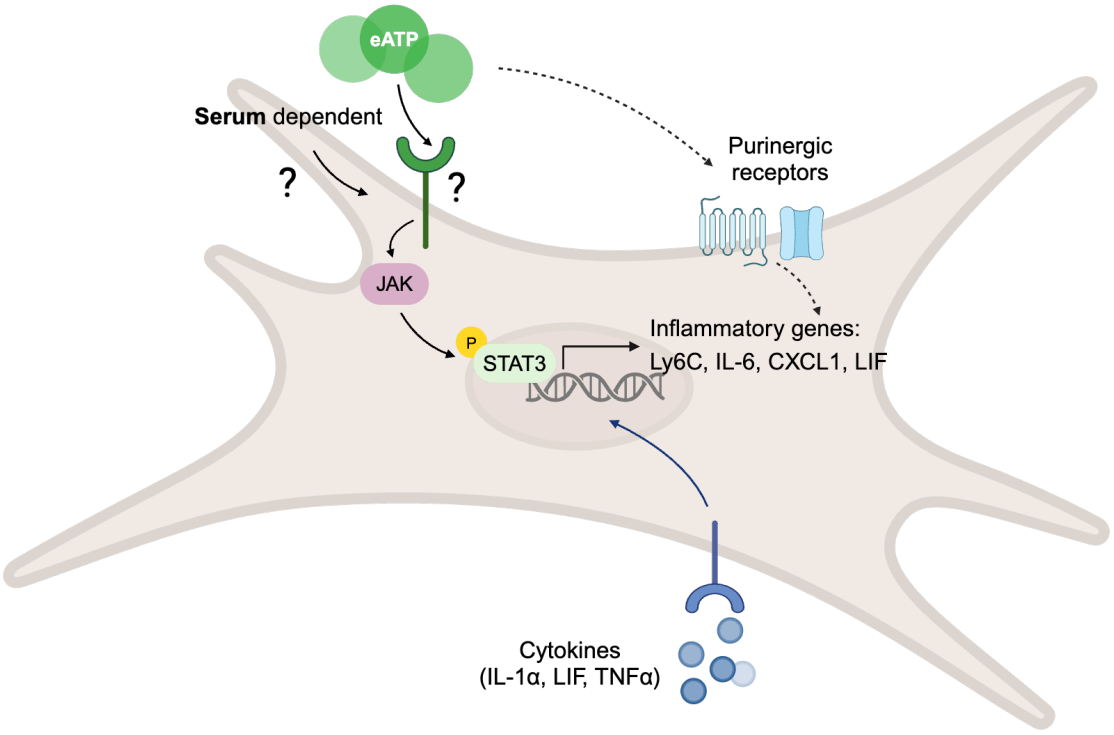

Figure 4.2 Proposed model for eATP promoting an iCAF state (created with BioRender.com).

4.5 Is the effect of eATP promoting an iCAF-like state solely from extracellular signaling?

We have found that eATP can induce phosphorylation of STAT3 (Fig.3.4A-C) as well as initiate gene transcription (data not shown) within 1 hour. In addition, eATP can increase EGFP fluorescence driven by *IL6* promoter at early time points (Fig.3.1D). Not only eATP can work in a relative short time, but also its effect can almost be completely abolished by JAK inhibition (Fig. 3.4F). Moreover, ATP is a relatively big molecule with a lot of negative charges and has thus been thought to be cell impermeable. These pieces of evidence make us lean toward the hypothesis that the ATP promotes an iCAF state by acting as an extracellular signaling molecule.

However, at this stage, we cannot fully rule out the possibility that eATP enters the cell and functions intracellularly. Indeed, studies have showed that ATP-treated mouse cells significantly and rapidly increase its membrane permeability, which leads to a massive efflux of nucleotide pools (Chaudry 1982). In addition, some equilibrative nucleoside transporters (ENTs) can mediate the uptake of eATP, although more pronounced in its degraded form, adenosine (Boswell-Casteel and Hays 2017).

Thus, we propose the following experiments:

1) Check nucleoside transporters expression in our PSC1d cells based on the RNA-seq results and abolish nucleoside transporters by using Dipyridamole (a pan ENT, CNT inhibitor) and examine if eATP effect on iCAF state is significantly decreased. However, if there is no effect, later it can be difficult to justify if the inhibitor itself is functional as expected.

2) Obtain and treat cells with isotope labelled eATP. First, we need to confirm that the isotope labelled ATP can still promote an iCAF state. Second, we will lyse the cells, extract intracellular metabolites, and run on GC/MS to see if the labelling of metabolites can be detected. If so, it can suggest that eATP can get inside the cells. There are several isotope labeled ATP that are commercially available, such as, [γ-18O4]ATP, 18O-ATP, 2-F-2-C13-ATP, 13C10-15N5-ATP. Among them, [γ-18O4]ATP may not be ideal because its labelling is at phosphate group that can be hydrolyzed, making the detected labelling potentially independent of ATP but from the phosphate group. The pitfalls are, first, even if ATP is detected inside the cells, it is unknown if the iCAF promoting effect is from intracellular ATP – it can still be through eATP signaling, just some can get inside of the cells. Second, ATP can be hydrolyzed extracellularly into adenosine, and labelled adenosine gets inside the cell and then reassemble into ATP intracellularly. Thus, we might need to disturb CD39 or CD73 to inhibit the potential

ATP hydrolyzation. Worth noting that, the gene *Entpd1* (encodes CD39) and *Nt5e* (encodes CD73) are almost not expressed in our PSC1d cells from RNA-seq analysis (data not shown), which we need to confirm by immunoblotting. In short, even if ATP can get inside the cells, and either initiating signaling or metabolism, it is still unknown if these mechanisms explain the ATP effect in promoting an iCAF state. To answer that question, we can inhibitor ATP transporters and check if the iCAF state promoting effect of eATP still exists.

4.6 How does our story fit into the purinergic receptor field?

We would like to clarify that although our current data does not support eATP functions through purinergic receptor to promote an iCAF state, we are not claiming that in our system eATP does not bind to purinergic receptors. In fact, we have shown that eATP can indeed induce intracellular calcium flux, a major effect downstream of purinergic receptor, but our data suggest that this downstream effect does not explain the iCAF promoting effect of eATP (Fig.3.3A-B). In addition, we also found that, after treating cells with purinergic receptor inhibitors, eATP effect is enhanced rather than diminished (Fig.3.3C-I), potentially indicating that by blocking purinergic receptors, it frees up more eATP so as to bind to its real effector in fibroblasts.

Indeed, one can easily criticize that, we have not tested how specific are the inhibitors, and whether they really block the purinergic receptors. We choose inhibitors based on literatures and used at concentrations around and above the reported IC50. For future directions, we should test these inhibitors by examining if they block calcium flux by eATP. Also, we should genetically knock out these receptors and validate eATP effect. Not only for some technical concerns regarding inhibitor effect; biologically, the purinergic receptors can present redundancy, so that abolishing one may not explain the effect of eATP. To solve that problem,

we have obtained pan-P2X inhibitors, PPADS, and will test if eATP still promotes an iCAF state with PPADS. In short, we cannot completely rule out the purinergic receptors yet (Fig. 4.2).

Worth noting is that, there are some studies that explored extracellular nucleotides and fibroblasts before. In a study published in 2011, the authors also found extracellular ATP can elicit intracellular calcium flux in PSCs, as well as ADP and AMP, and this is both P2X and P2Y receptor dependent (Hennigs et al. 2011). In addition, eATP can increase calcium in human pulmonary fibroblasts, and also increase TGFβ, collagen A1, and fibronectin RNA levels through P2Y receptors (Janssen et al. 2009). Also, a study shows that cardiac fibroblasts can release ATP, and that in turn activates P2Y2 receptor that leads to increased αSMA and collagen production in an ERK-dependent manner (Lu et al. 2012). ATP can dose-dependently increase ECM and TGFβ production in rat mesangial cells (Solini et al. 2005). Moreover, ATP can bind to P2X4 and induce profibrogenic gene expression (αSMA, IL-6, TIMP-1, VEGF-A) in hepatic stellate cells (Le Guilcher et al. 2018). Altogether, previous work suggests that in lung fibroblasts, eATP go through purinergic receptors to induce αSMA and ECM production and further causes lung fibrosis. Thus, it is possible that if the majority of eATP binds to purinergic receptors, the effect is mainly through αSMA and causes ECM remodeling. However, no study has yet to show the effect of eATP in pancreatic fibroblasts. It is possible that, there is a cell surface receptor that specifically expressed by PSCs that has a much higher affinity to eATP than purinergic receptors, or itself is expressed at much higher level than purinergic receptors. And this receptor can recruit JAK and initiate JAK-STAT pathway to make PSCs toward an inflammatory state that override the effect through purinergic receptors. Furthermore, while we have shown that eATP downregulates *Acta2* (encoding SMA) expression, we have not yet analyzed SMA and ECM expression after eATP treatment on a protein level.

4.7 Why is it serum dependent for eATP to promote an iCAF state?

We have shown that under serum starvation, eATP is no longer able to increase Ly6C and IL-6 levels (Fig.3.5). There are several possibilities to explain such serum dependency:

1) Expression of the putative eATP receptor(s) on the cell surface is serum dependent. Thus, without serum, the eATP receptor is not expressed, rendering eATP unable to promote an iCAF state. To test this hypothesis, we can isolate cell membrane from PSC1d cells under both 0.5% FBS and 10% FBS and perform proteomics and compare the differentiation of receptor expression.

2) Recruitment of JAK to the putative eATP receptor(s) is serum dependent. To test that, we have obtained a phospho-Jak family antibody sampler kit that contains various p-JAK antibodies. We will isolate protein lysate from PSC1d cells treated with eATP and cultured under both 0.5% FBS and 10% FBS and examine JAK phosphorylation by immunoblotting. If JAK is no longer phosphorylated under serum starvation, indicating that JAK recruitment is serum dependent.

Future experiments will need to resolve the contributions of individual growth factors and cytokines from the serum, based on reported serum composition (Lee et al. 2022).

4.8 Is JAK-STAT pathway the dominant mechanism?

We have found that eATP effect in promoting an iCAF state can be abolished by the JAK2 inhibitor AZD1480. Although this inhibitor has previously been tested by Dr. Schwörer in the same context of PSCs and showed great potency (Schwörer et al. 2023), we still need to further confirm the inhibition efficiency in our system especially after adding eATP. To test this,

we will extract protein from PSC1d cells treated with ATP, JAK2i, and combinations and examine JAK2 phosphorylation and STAT3 phosphorylation. One critique of our current study is, although we showed the JAK2i can abolish the eATP effect, and in a separate experiment, eATP can phosphorylate STAT3, we have not demonstrated the causality between them. Experiments proposed above can help answer this concern.

Moreover, there are four isoforms in JAK family, they are JAK1, JAK2, JAK2, and TYK2 (X. Hu et al. 2021). Although JAK2i can abolish the effect, we haven't shown JAK2 phosphorylation is dominant after eATP treatment. To test that, we have obtained a phospho-Jak family antibody sampler kit that contains various p-JAK antibodies. We will isolate protein lysate from PSC1d cells before and after treatment with eATP and examine JAK isoforms by immunoblotting.

Meanwhile, we will knockout STAT3 by CRISPR-Cas9 and if eATP effect is completely abolished in STAT3 KO cells, this indicate JAK-STAT3 pathway is the dominant mechanism for eATP promoting an iCAF state.

4.9 Since eATP promotes PSCs to secret IL-6, can it be IL-6 rather than eATP that activate the JAK-STAT pathway?

We have found that eATP can promote an iCAF state by upregulating multiple inflammatory markers, such as IL-6, CXCL1, LIF, and Ly6C (Figure 4.2). Among them, IL-6 is the classic cytokine that can activate JAK-STAT3 pathway (D. E. Johnson, O'Keefe, and Grandis 2018). Given that we also found JAK-STAT pathway can be the major downstream signaling pathway of eATP, it is possible that after eATP promoting IL-6 secretion, secreted IL-6

acts in an autocrine manner to activate JAK-STAT pathway and causes the inflammatory phenotype.

While this model is intriguing, we have shown by ELISA that without cytokines, eATP itself is not promoting IL-6 concentrations in the conditioned media, at least after 6 hours of eATP treatments (Fig.3.2E). However, we have also shown that eATP by itself can already induce p-STAT3 levels after 1 hour of eATP treatment (Fig.3.4A-C). This indicates that, eATP can promote JAK-STAT pathway by itself and it is not dependent on potential IL-6 autocrine function. If needed to further examine the idea, we can also obtain an IL-6 neutralization antibody and test if eATP can still promote an iCAF state with IL-6 protein neutralized.

Bibliography

American Cancer Society. 2024. “Cancer Facts & Figures 2024.” https://www.cancer.org/content/dam/cancer-org/research/cancer-facts-and-statistics/annual-cancer-facts-and-figures/2024/2024-cancer-facts-and-figures-acs.pdf.

Ando, Hideaki, Katsuhiro Kawaai, and Katsuhiko Mikoshiba. 2014. “IRBIT: A Regulator of Ion Channels and Ion Transporters.” *Biochimica et Biophysica Acta* 1843 (10): 2195–2204.

Ando, Hideaki, Akihiro Mizutani, Hélène Kiefer, Dai Tsuzurugi, Takayuki Michikawa, and Katsuhiko Mikoshiba. 2006. “IRBIT Suppresses IP3 Receptor Activity by Competing with IP3 for the Common Binding Site on the IP3 Receptor.” *Molecular Cell* 22 (6): 795–806.

Ando, Hideaki, Akihiro Mizutani, Toru Matsu-ura, and Katsuhiko Mikoshiba. 2003. “IRBIT, a Novel Inositol 1,4,5-Trisphosphate (IP3) Receptor-Binding Protein, Is Released from the IP3 Receptor upon IP3 Binding to the Receptor.” *The Journal of Biological Chemistry* 278 (12): 10602–12.

Ando, Hideaki, Akihiro Mizutani, and Katsuhiko Mikoshiba. 2009. “An IRBIT Homologue Lacks Binding Activity to Inositol 1,4,5-Trisphosphate Receptor Due to the Unique N-Terminal Appendage.” *Journal of Neurochemistry* 109 (2): 539–50.

Apiz Saab, Juan J., Lindsey N. Dzierozynski, Patrick B. Jonker, Roya AminiTabrizi, Hardik Shah, Rosa Elena Menjivar, Andrew J. Scott, et al. 2023. “Pancreatic Tumors Exhibit Myeloid-Driven Amino Acid Stress and Upregulate Arginine Biosynthesis.” *ELife* 12 (May). https://doi.org/10.7554/eLife.81289.

Are, Chandrakanth, Mashaal Dhir, and Lavanya Ravipati. 2011. “History of Pancreaticoduodenectomy: Early Misconceptions, Initial Milestones and the Pioneers.” *HPB: The Official Journal of the International Hepato Pancreato Biliary Association* 13 (6): 377–84.

Bahar, Entaz, Hyongsuk Kim, and Hyonok Yoon. 2016. “ER Stress-Mediated Signaling: Action Potential and Ca(2+) as Key Players.” *International Journal of Molecular Sciences* 17 (9). https://doi.org/10.3390/ijms17091558.

Balachandran, Vinod P., Gregory L. Beatty, and Stephanie K. Dougan. 2019. “Broadening the Impact of Immunotherapy to Pancreatic Cancer: Challenges and Opportunities.” *Gastroenterology* 156 (7): 2056–72.

Bhattacharyya, Aritra, Paola Torre, Preeti Yadav, Kaveh Boostanpour, Tian Y. Chen, Tatsuya Tsukui, Dean Sheppard, et al. 2022. “Macrophage Cx43 Is Necessary for Fibroblast Cytosolic Calcium and Lung Fibrosis After Injury.” *Frontiers in Immunology* 13 (May): 880887.

Biffi, Giulia, Tobiloba E. Oni, Benjamin Spielman, Yuan Hao, Ela Elyada, Youngkyu Park, Jonathan Preall, and David A. Tuveson. 2019. “IL1-Induced JAK/STAT Signaling Is Antagonized by TGFβ to Shape CAF Heterogeneity in Pancreatic Ductal Adenocarcinoma.” *Cancer Discovery* 9 (2): 282–301.

Biffi, Giulia, and David A. Tuveson. 2021. “Diversity and Biology of Cancer-Associated Fibroblasts.” *Physiological Reviews* 101 (1): 147–76.

Bittremieux, Mart, Jan B. Parys, Paolo Pinton, and Geert Bultynck. 2016. “ER Functions of Oncogenes and Tumor Suppressors: Modulators of Intracellular Ca2+ Signaling.”

Biochimica et Biophysica Acta (BBA) - Molecular Cell Research 1863 (6, Part B): 1364–78.

Bollag, Gideon, James Tsai, Jiazhong Zhang, Chao Zhang, Prabha Ibrahim, Keith Nolop, and Peter Hirth. 2012. "Vemurafenib: The First Drug Approved for BRAF-Mutant Cancer." *Nature Reviews. Drug Discovery* 11 (11): 873–86.

Boswell-Casteel, Rebba C., and Franklin A. Hays. 2017. "Equilibrative Nucleoside Transporters-A Review." *Nucleosides, Nucleotides & Nucleic Acids* 36 (1): 7–30.

Cai, Chufan, Jiayi Tu, Jeronimo Najarro, Rukang Zhang, Hao Fan, Freya Q. Zhang, Jiacheng Li, et al. 2024. "NRAS Mutant Dictates AHCYL1-Governed ER Calcium Homeostasis for Melanoma Tumor Growth." *Molecular Cancer Research: MCR*, January. https://doi.org/10.1158/1541-7786.MCR-23-0445.

Carroll, Simon F., Conor T. Buckley, and Daniel J. Kelly. 2021. "Measuring and Modeling Oxygen Transport and Consumption in 3D Hydrogels Containing Chondrocytes and Stem Cells of Different Tissue Origins." *Frontiers in Bioengineering and Biotechnology* 9 (May). https://doi.org/10.3389/fbioe.2021.591126.

Chalmers, Fiona, Bernadette Sweeney, Katharine Cain, and Neil J. Bulleid. 2017. "Inhibition of IRE1α-Mediated XBP1 MRNA Cleavage by XBP1 Reveals a Novel Regulatory Process during the Unfolded Protein Response." *Wellcome Open Research* 2 (June): 36.

Chaudry, I. H. 1982. "Does ATP Cross the Cell Plasma Membrane." *The Yale Journal of Biology and Medicine* 55 (1): 1–10.

Chen, Yang, Jiha Kim, Sujuan Yang, Huamin Wang, Chang-Jiun Wu, Hikaru Sugimoto, Valerie S. LeBleu, and Raghu Kalluri. 2021. "Type I Collagen Deletion in ASMA+ Myofibroblasts Augments Immune Suppression and Accelerates Progression of Pancreatic Cancer." *Cancer Cell* 39 (4): 548-565.e6.

Concepcion, Axel R., Larry E. Wagner 2nd, Jingjie Zhu, Anthony Y. Tao, Jun Yang, Alireza Khodadadi-Jamayran, Yin-Hu Wang, et al. 2022. "The Volume-Regulated Anion Channel LRRC8C Suppresses T Cell Function by Regulating Cyclic Dinucleotide Transport and STING-P53 Signaling." *Nature Immunology* 23 (2): 287–302.

Costa-Mattioli, Mauro, and Peter Walter. 2020. "The Integrated Stress Response: From Mechanism to Disease." *Science* 368 (6489). https://doi.org/10.1126/science.aat5314.

Cui, Chaochu, Robert Merritt, Liwu Fu, and Zui Pan. 2017. "Targeting Calcium Signaling in Cancer Therapy." *Acta Pharmaceutica Sinica. B* 7 (1): 3–17.

Deng, Yulan, Shangyi Luo, Chunyu Deng, Tao Luo, Wenkang Yin, Hongyi Zhang, Yong Zhang, et al. 2019. "Identifying Mutual Exclusivity across Cancer Genomes: Computational Approaches to Discover Genetic Interaction and Reveal Tumor Vulnerability." *Briefings in Bioinformatics* 20 (1): 254–66.

Devitt, Bianca, Wendy Liu, Renato Salemi, Rory Wolfe, John Kelly, Chin-Yuan Tzen, Alexander Dobrovic, and Grant McArthur. 2011. "Clinical Outcome and Pathological Features Associated with NRAS Mutation in Cutaneous Melanoma." *Pigment Cell & Melanoma Research* 24 (4): 666–72.

Devogelaere, Benoit, Nael Nadif Kasri, Rita Derua, Etienne Waelkens, Geert Callewaert, Ludwig Missiaen, Jan B. Parys, and Humbert De Smedt. 2006. "Binding of IRBIT to the IP3 Receptor: Determinants and Functional Effects." *Biochemical and Biophysical Research Communications* 343 (1): 49–56.

Devogelaere, Benoit, Eva Sammels, and Humbert De Smedt. 2008. “The IRBIT Domain Adds New Functions to the AHCY Family.” *BioEssays: News and Reviews in Molecular, Cellular and Developmental Biology* 30 (7): 642–52.

Di Virgilio, Francesco, Alba Clara Sarti, Simonetta Falzoni, Elena De Marchi, and Elena Adinolfi. 2018. “Extracellular ATP and P2 Purinergic Signalling in the Tumour Microenvironment.” *Nature Reviews. Cancer* 18 (10): 601–18.

Doench, John G., Nicolo Fusi, Meagan Sullender, Mudra Hegde, Emma W. Vaimberg, Katherine F. Donovan, Ian Smith, et al. 2016. “Optimized SgRNA Design to Maximize Activity and Minimize Off-Target Effects of CRISPR-Cas9.” *Nature Biotechnology* 34 (2): 184–91.

Dominguez, Claudia X., Sören Müller, Shilpa Keerthivasan, Hartmut Koeppen, Jeffrey Hung, Sarah Gierke, Beatrice Breart, et al. 2020. “Single-Cell RNA Sequencing Reveals Stromal Evolution into LRRC15+ Myofibroblasts as a Determinant of Patient Response to Cancer Immunotherapy.” *Cancer Discovery* 10 (2): 232–53.

Dvorak, H. F. 1986. “Tumors: Wounds That Do Not Heal. Similarities between Tumor Stroma Generation and Wound Healing.” *The New England Journal of Medicine* 315 (26): 1650–59.

Elyada, Ela, Mohan Bolisetty, Pasquale Laise, William F. Flynn, Elise T. Courtois, Richard A. Burkhart, Jonathan A. Teinor, et al. 2019. “Cross-Species Single-Cell Analysis of Pancreatic Ductal Adenocarcinoma Reveals Antigen-Presenting Cancer-Associated Fibroblasts.” *Cancer Discovery* 9 (8): 1102–23.

Esteves, Gabriela Nohemi Nuñez, Letícia Silva Ferraz, Marcela Maciel Palacio Alvarez, Claudia Alves da Costa, Rayssa de Mello Lopes, Ivarne Luis Dos Santos Tersariol, and Tiago Rodrigues. 2020. “BRAF and NRAS Mutated Melanoma: Different Ca2+ Responses, Na+/Ca2+ Exchanger Expression, and Sensitivity to Inhibitors.” *Cell Calcium* 90 (September): 102241.

Fan, Hao, Siyuan Xia, Junhong Xiang, Yuancheng Li, Matthew O. Ross, Seon Ah Lim, Fan Yang, et al. 2023. “Trans-Vaccenic Acid Reprograms CD8+ T Cells and Anti-Tumour Immunity.” *Nature* 623 (7989): 1034–43.

Fritz, Valerie, Lara Malek, Anne Gaza, Laura Wormser, Majken Appel, Andreas E. Kremer, Wolfgang E. Thasler, et al. 2021. “Combined De-Repression of Chemoresistance Associated Mitogen-Activated Protein Kinase 14 and Activating Transcription Factor 2 by Loss of MicroRNA-622 in Hepatocellular Carcinoma.” *Cancers* 13 (5). https://doi.org/10.3390/cancers13051183.

Gao, Xue, Yijie Liu, Yuancheng Li, Hao Fan, Rong Wu, Rukang Zhang, Brandon Faubert, et al. 2022. “Lyso-PAF, a Biologically Inactive Phospholipid, Contributes to RAF1 Activation.” *Molecular Cell*, April. https://doi.org/10.1016/j.molcel.2022.03.026.

Garajová, Ingrid, Marianna Peroni, Fabio Gelsomino, and Francesco Leonardi. 2023. “A Simple Overview of Pancreatic Cancer Treatment for Clinical Oncologists.” *Current Oncology* 30 (11): 9587–9601.

Gonzalez-Cao, Maria, Rafael Rosell, Salvador Martin Algarra, Teresa Puertolas, and Enrique Espinosa. 2023. “Sequence of Therapies for Advanced BRAFV600E/K Melanoma.” *Annals of Translational Medicine*. AME Publishing Company.

Grandjean, Julia M. D., and R. Luke Wiseman. 2020. “Small Molecule Strategies to Harness the Unfolded Protein Response: Where Do We Go from Here?” *The Journal of Biological Chemistry* 295 (46): 15692–711.

Hakim, Nausheen, Rajvi Patel, Craig Devoe, and Muhammad W. Saif. 2019. “Why HALO 301 Failed and Implications for Treatment of Pancreatic Cancer.” *Pancreas* 3 (1): e1–4.
Hanahan, Douglas. 2022. “Hallmarks of Cancer: New Dimensions.” *Cancer Discovery* 12 (1): 31–46.
Helms, Erin, M. Kathrina Onate, and Mara H. Sherman. 2020. “Fibroblast Heterogeneity in the Pancreatic Tumor Microenvironment.” *Cancer Discovery* 10 (5): 648–56.
Hennigs, Jan K., Oliver Seiz, Julia Spiro, Marc J. Berna, Hans Jörg Baumann, Hans Klose, and Andrea Pace. 2011. “Molecular Basis of P2-Receptor-Mediated Calcium Signaling in Activated Pancreatic Stellate Cells.” *Pancreas* 40 (5): 740–46.
Hetz, Claudio, Kezhong Zhang, and Randal J. Kaufman. 2020. “Mechanisms, Regulation and Functions of the Unfolded Protein Response.” *Nature Reviews. Molecular Cell Biology* 21 (8): 421–38.
Hosein, Abdel Nasser, Huocong Huang, Zhaoning Wang, Kamalpreet Parmar, Wenting Du, Jonathan Huang, Anirban Maitra, Eric Olson, Udit Verma, and Rolf A. Brekken. 2019. “Cellular Heterogeneity during Mouse Pancreatic Ductal Adenocarcinoma Progression at Single-Cell Resolution.” *JCI Insight* 5 (July). https://doi.org/10.1172/jci.insight.129212.
Hrabák, P., M. Kalousová, T. Krechler, and T. Zima. 2021. “Pancreatic Stellate Cells - Rising Stars in Pancreatic Pathologies.” *Physiological Research*, December, S597–616.
Hu, Li-Peng, Xiao-Xin Zhang, Shu-Heng Jiang, Ling-Ye Tao, Qing Li, Li-Li Zhu, Ming-Wei Yang, et al. 2019. “Targeting Purinergic Receptor P2Y2 Prevents the Growth of Pancreatic Ductal Adenocarcinoma by Inhibiting Cancer Cell Glycolysis.” *Clinical Cancer Research: An Official Journal of the American Association for Cancer Research* 25 (4): 1318–30.
Hu, Xiaoyi, Jing Li, Maorong Fu, Xia Zhao, and Wei Wang. 2021. “The JAK/STAT Signaling Pathway: From Bench to Clinic.” *Signal Transduction and Targeted Therapy* 6 (1): 402.
Huang, Alan, Levi A. Garraway, Alan Ashworth, and Barbara Weber. 2020. “Synthetic Lethality as an Engine for Cancer Drug Target Discovery.” *Nature Reviews. Drug Discovery* 19 (1): 23–38.
Ibarra, Juan, Yassmin A. Elbanna, Katarzyna Kurylowicz, Michele Ciboddo, Harrison S. Greenbaum, Nicole S. Arellano, Deborah Rodriguez, et al. 2022. “Type 1 but Not Type 2 Calreticulin Mutations Activate the IRE1a/XBP1 Pathway of the Unfolded Protein Response to Drive Myeloproliferative Neoplasms.” *Blood Cancer Discovery*, April. https://doi.org/10.1158/2643-3230.BCD-21-0144.
Jacobetz, Michael A., Derek S. Chan, Albrecht Neesse, Tashinga E. Bapiro, Natalie Cook, Kristopher K. Frese, Christine Feig, et al. 2013. “Hyaluronan Impairs Vascular Function and Drug Delivery in a Mouse Model of Pancreatic Cancer.” *Gut* 62 (1): 112–20.
Jakob, John A., Roland L. Bassett Jr, Chaan S. Ng, Jonathan L. Curry, Richard W. Joseph, Gladys C. Alvarado, Michelle L. Rohlfs, et al. 2012. “NRAS Mutation Status Is an Independent Prognostic Factor in Metastatic Melanoma.” *Cancer* 118 (16): 4014–23.
Janssen, Luke J., Laszlo Farkas, Tahseen Rahman, and Martin R. J. Kolb. 2009. “ATP Stimulates Ca(2+)-Waves and Gene Expression in Cultured Human Pulmonary Fibroblasts.” *The International Journal of Biochemistry & Cell Biology* 41 (12): 2477–84.
Jesnowski, Ralf, Daniel Fürst, Jörg Ringel, Ying Chen, Andrea Schrödel, Jörg Kleeff, Armin Kolb, Wolfgang D. Schareck, and Matthias Löhr. 2005. “Immortalization of Pancreatic Stellate Cells as an in Vitro Model of Pancreatic Fibrosis: Deactivation Is Induced by

Matrigel and N-Acetylcysteine." *Laboratory Investigation; a Journal of Technical Methods and Pathology* 85 (10): 1276–91.
Johnson, Daniel E., Rachel A. O'Keefe, and Jennifer R. Grandis. 2018. "Targeting the IL-6/JAK/STAT3 Signalling Axis in Cancer." *Nature Reviews. Clinical Oncology* 15 (4): 234–48.
Johnson, Douglas B., and Jeffrey A. Sosman. 2013. "Update on the Targeted Therapy of Melanoma." *Current Treatment Options in Oncology* 14 (2): 280–92.
Joseph, Ann Mary, Ahmad Al Aiyan, Basel Al-Ramadi, Shiv K. Singh, and Uday Kishore. 2024. "Innate and Adaptive Immune-Directed Tumour Microenvironment in Pancreatic Ductal Adenocarcinoma." *Frontiers in Immunology* 15 (February). https://doi.org/10.3389/fimmu.2024.1323198.
Kamphorst, Jurre J., Michel Nofal, Cosimo Commisso, Sean R. Hackett, Wenyun Lu, Elda Grabocka, Matthew G. Vander Heiden, et al. 2015. "Human Pancreatic Cancer Tumors Are Nutrient Poor and Tumor Cells Actively Scavenge Extracellular Protein." *Cancer Research* 75 (3): 544–53.
Kang, Hee-Bum, Jun Fan, Ruiting Lin, Shannon Elf, Quanjiang Ji, Liang Zhao, Lingtao Jin, et al. 2015. "Metabolic Rewiring by Oncogenic BRAF V600E Links Ketogenesis Pathway to BRAF-MEK1 Signaling." *Molecular Cell* 59 (3): 345–58.
Karamitopoulou, Eva. 2019. "Tumour Microenvironment of Pancreatic Cancer: Immune Landscape Is Dictated by Molecular and Histopathological Features." *British Journal of Cancer* 121 (1): 5–14.
Karim, Sherko Abdullah Molah, Karzan Seerwan Abdulla, Qalandar Hussein Abdulkarim, and Fattah Hama Rahim. 2018. "The Outcomes and Complications of Pancreaticoduodenectomy (Whipple Procedure): Cross Sectional Study." *International Journal of Surgery (London, England)* 52 (April): 383–87.
Katsuta, Eriko, Qianya Qi, Xuan Peng, Steven N. Hochwald, Li Yan, and Kazuaki Takabe. 2019. "Pancreatic Adenocarcinomas with Mature Blood Vessels Have Better Overall Survival." *Scientific Reports* 9 (1): 1310.
Kemp, Samantha B., Noah Cheng, Nune Markosyan, Rina Sor, Il-Kyu Kim, Jill Hallin, Jason Shoush, et al. 2023. "Efficacy of a Small-Molecule Inhibitor of KrasG12D in Immunocompetent Models of Pancreatic Cancer." *Cancer Discovery* 13 (2): 298–311.
Kolbeinsson, Hordur Mar, Sreenivasa Chandana, G. Paul Wright, and Mathew Chung. 2023. "Pancreatic Cancer: A Review of Current Treatment and Novel Therapies." *Journal of Investigative Surgery: The Official Journal of the Academy of Surgical Research* 36 (1): 2129884.
Krebs, Joachim, Luis B. Agellon, and Marek Michalak. 2015. "Ca(2+) Homeostasis and Endoplasmic Reticulum (ER) Stress: An Integrated View of Calcium Signaling." *Biochemical and Biophysical Research Communications* 460 (1): 114–21.
Krebs, Joachim, Jody Groenendyk, and Marek Michalak. 2011. "Ca2+-Signaling, Alternative Splicing and Endoplasmic Reticulum Stress Responses." *Neurochemical Research* 36 (7): 1198–1211.
Lau, Eric, and Ze'ev A. Ronai. 2012. "ATF2 - at the Crossroad of Nuclear and Cytosolic Functions." *Journal of Cell Science* 125 (Pt 12): 2815–24.
Le Guilcher, Camille, Isabelle Garcin, Olivier Dellis, Florent Cauchois, Ali Tebbi, Isabelle Doignon, Catherine Guettier, Boris Julien, and Thierry Tordjmann. 2018. "The P2X4

Purinergic Receptor Regulates Hepatic Myofibroblast Activation during Liver Fibrogenesis." *Journal of Hepatology* 69 (3): 644–53.
LeBleu, Valerie S., Gangadhar Taduri, Joyce O'Connell, Yingqi Teng, Vesselina G. Cooke, Craig Woda, Hikaru Sugimoto, and Raghu Kalluri. 2013. "Origin and Function of Myofibroblasts in Kidney Fibrosis." *Nature Medicine* 19 (8): 1047–53.
Lee, Da Young, Seung Yun Lee, Seung Hyeon Yun, Jae Won Jeong, Jae Hyeon Kim, Hyun Woo Kim, Jung Seok Choi, et al. 2022. "Review of the Current Research on Fetal Bovine Serum and the Development of Cultured Meat." *Food Science of Animal Resources* 42 (5): 775–99.
Leicht, Deborah T., Vitaly Balan, Alexander Kaplun, Vinita Singh-Gupta, Ludmila Kaplun, Melissa Dobson, and Guri Tzivion. 2007. "Raf Kinases: Function, Regulation and Role in Human Cancer." *Biochimica et Biophysica Acta* 1773 (8): 1196–1212.
Li, Xubin, Mengqiao Zhang, Xue Yu, Mei Xue, Xiaowei Li, Chao Ma, Wei Jia, Qiang Gao, and Chunbo Kang. 2022. "AHCYL1 Is a Novel Biomarker for Predicting Prognosis and Immunotherapy Response in Colorectal Cancer." *Journal of Oncology* 2022 (May): 5054324.
Lin, Ruiting, Siyuan Xia, Changliang Shan, Dong Chen, Yijie Liu, Xue Gao, Mei Wang, et al. 2018. "The Dietary Supplement Chondroitin-4-Sulfate Exhibits Oncogene-Specific Pro-Tumor Effects on BRAF V600E Melanoma Cells." *Molecular Cell* 69 (6): 923-937.e8.
Liszkay, Gabriella, Zoltán Mátrai, Kata Czirbesz, Nóra Jani, Eszter Bencze, and István Kenessey. 2021. "Predictive and Prognostic Value of BRAF and NRAS Mutation of 159 Sentinel Lymph Node Cases in Melanoma-A Retrospective Single-Institute Study." *Cancers* 13 (13). https://doi.org/10.3390/cancers13133302.
Lo, Albert, Chung-Pin Li, Elizabeth L. Buza, Rachel Blomberg, Priya Govindaraju, Diana Avery, James Monslow, Michael Hsiao, and Ellen Puré. 2017. "Fibroblast Activation Protein Augments Progression and Metastasis of Pancreatic Ductal Adenocarcinoma." *JCI Insight* 2 (19). https://doi.org/10.1172/jci.insight.92232.
Lopez-Bergami, Pablo, Eric Lau, and Ze'ev Ronai. 2010. "Emerging Roles of ATF2 and the Dynamic AP1 Network in Cancer." *Nature Reviews. Cancer* 10 (1): 65–76.
Lu, David, Sahar Soleymani, Rohit Madakshire, and Paul A. Insel. 2012. "ATP Released from Cardiac Fibroblasts via Connexin Hemichannels Activates Profibrotic P2Y2 Receptors." *FASEB Journal: Official Publication of the Federation of American Societies for Experimental Biology* 26 (6): 2580–91.
Luo, B., and A. S. Lee. 2013. "The Critical Roles of Endoplasmic Reticulum Chaperones and Unfolded Protein Response in Tumorigenesis and Anticancer Therapies." *Oncogene* 32 (7): 805–18.
Marchi, Saverio, Carlotta Giorgi, Lorenzo Galluzzi, and Paolo Pinton. 2020. "Ca2+ Fluxes and Cancer." *Molecular Cell* 78 (6): 1055–69.
Marchi, Saverio, and Paolo Pinton. 2016. "Alterations of Calcium Homeostasis in Cancer Cells." *Current Opinion in Pharmacology* 29 (August): 1–6.
McAndrews, Kathleen M., Yang Chen, J. Kebbeh Darpolor, Xiaofeng Zheng, Sujuan Yang, Julienne L. Carstens, Bingrui Li, et al. 2022. "Identification of Functional Heterogeneity of Carcinoma-Associated Fibroblasts with Distinct IL6-Mediated Therapy Resistance in Pancreatic Cancer." *Cancer Discovery* 12 (6): 1580–97.
"Melanoma." 2018. The Skin Cancer Foundation. July 23, 2018. https://www.skincancer.org/skin-cancer-information/melanoma/.

Min, Hye-Young, and Ho-Young Lee. 2018. “Oncogene-Driven Metabolic Alterations in Cancer.” *Biomolecules & Therapeutics* 26 (1): 45–56.
Monteith, Gregory R., Natalia Prevarskaya, and Sarah J. Roberts-Thomson. 2017. “The Calcium-Cancer Signalling Nexus.” *Nature Reviews. Cancer* 17 (6): 367–80.
Moore, Amanda R., Scott C. Rosenberg, Frank McCormick, and Shiva Malek. 2020. “RAS-Targeted Therapies: Is the Undruggable Drugged?” *Nature Reviews. Drug Discovery* 19 (8): 533–52.
Öhlund, Daniel, Abram Handly-Santana, Giulia Biffi, Ela Elyada, Ana S. Almeida, Mariano Ponz-Sarvise, Vincenzo Corbo, et al. 2017. “Distinct Populations of Inflammatory Fibroblasts and Myofibroblasts in Pancreatic Cancer.” *The Journal of Experimental Medicine* 214 (3): 579–96.
Orth, Michael, Philipp Metzger, Sabine Gerum, Julia Mayerle, Günter Schneider, Claus Belka, Maximilian Schnurr, and Kirsten Lauber. 2019. “Pancreatic Ductal Adenocarcinoma: Biological Hallmarks, Current Status, and Future Perspectives of Combined Modality Treatment Approaches.” *Radiation Oncology* 14 (1): 141.
Özdemir, Berna C., Tsvetelina Pentcheva-Hoang, Julienne L. Carstens, Xiaofeng Zheng, Chia-Chin Wu, Tyler R. Simpson, Hanane Laklai, et al. 2014. “Depletion of Carcinoma-Associated Fibroblasts and Fibrosis Induces Immunosuppression and Accelerates Pancreas Cancer with Reduced Survival.” *Cancer Cell* 25 (6): 719–34.
Papassava, Paraskevi, Vassilis G. Gorgoulis, Dimitra Papaevangeliou, Spiros Vlahopoulos, Hans van Dam, and Vassilis Zoumpourlis. 2004. “Overexpression of Activating Transcription Factor-2 Is Required for Tumor Growth and Progression in Mouse Skin Tumors.” *Cancer Research* 64 (23): 8573–84.
Pellegatti, Patrizia, Lizzia Raffaghello, Giovanna Bianchi, Federica Piccardi, Vito Pistoia, and Francesco Di Virgilio. 2008. “Increased Level of Extracellular ATP at Tumor Sites: In Vivo Imaging with Plasma Membrane Luciferase.” *PloS One* 3 (7): e2599.
Poh, Ashleigh R., and Matthias Ernst. 2021. “Tumor-Associated Macrophages in Pancreatic Ductal Adenocarcinoma: Therapeutic Opportunities and Clinical Challenges.” *Cancers* 13 (12): 2860.
Preissler, Steffen, Claudia Rato, Yahui Yan, Luke A. Perera, Aron Czako, and David Ron. 2020. “Calcium Depletion Challenges Endoplasmic Reticulum Proteostasis by Destabilising BiP-Substrate Complexes.” *ELife* 9 (December). https://doi.org/10.7554/eLife.62601.
Principe, Daniel R., Patrick W. Underwood, Murray Korc, Jose G. Trevino, Hidayatullah G. Munshi, and Ajay Rana. 2021. “The Current Treatment Paradigm for Pancreatic Ductal Adenocarcinoma and Barriers to Therapeutic Efficacy.” *Frontiers in Oncology* 11 (July): 688377.
Pua, Lesley Jia Wei, Chun-Wai Mai, Felicia Fei-Lei Chung, Alan Soo-Beng Khoo, Chee-Onn Leong, Wei-Meng Lim, and Ling-Wei Hii. 2022. “Functional Roles of JNK and P38 MAPK Signaling in Nasopharyngeal Carcinoma.” *International Journal of Molecular Sciences* 23 (3). https://doi.org/10.3390/ijms23031108.
Qunaj, Lindor, Michael S. May, Alfred I. Neugut, and Benjamin O. Herzberg. 2023. “Prognostic and Therapeutic Impact of the KRAS G12C Mutation in Colorectal Cancer.” *Frontiers in Oncology* 13 (September): 1252516.
Ryan, Colm J., Ishan Mehta, Narod Kebabci, and David J. Adams. 2023. “Targeting Synthetic Lethal Paralogs in Cancer.” *Trends in Cancer Research* 9 (5): 397–409.

Sanjana, Neville E., Ophir Shalem, and Feng Zhang. 2014. “Improved Vectors and Genome-Wide Libraries for CRISPR Screening.” *Nature Methods* 11 (8): 783–84.
Sano, Renata, and John C. Reed. 2013. “ER Stress-Induced Cell Death Mechanisms.” *Biochimica et Biophysica Acta* 1833 (12): 3460–70.
Schwörer, Simon, Francesco V. Cimino, Manon Ros, Kaloyan M. Tsanov, Charles Ng, Scott W. Lowe, Carlos Carmona-Fontaine, and Craig B. Thompson. 2023. “Hypoxia Potentiates the Inflammatory Fibroblast Phenotype Promoted by Pancreatic Cancer Cell–Derived Cytokines.” *Cancer Research* 83 (10): 1596–1610.
Sehgal, Pankaj, Paula Szalai, Claus Olesen, Helle A. Praetorius, Poul Nissen, Søren Brøgger Christensen, Nikolai Engedal, and Jesper V. Møller. 2017. “Inhibition of the Sarco/Endoplasmic Reticulum (ER) Ca2+-ATPase by Thapsigargin Analogs Induces Cell Death via ER Ca2+ Depletion and the Unfolded Protein Response.” *The Journal of Biological Chemistry* 292 (48): 19656–73.
Shalem, Ophir, Neville E. Sanjana, Ella Hartenian, Xi Shi, David A. Scott, Tarjei Mikkelson, Dirk Heckl, et al. 2014. “Genome-Scale CRISPR-Cas9 Knockout Screening in Human Cells.” *Science* 343 (6166): 84–87.
Sidrauski, Carmela, Diego Acosta-Alvear, Arkady Khoutorsky, Punitha Vedantham, Brian R. Hearn, Han Li, Karine Gamache, et al. 2013. “Pharmacological Brake-Release of MRNA Translation Enhances Cognitive Memory.” *ELife* 2 (May): e00498.
Sidrauski, Carmela, Anna M. McGeachy, Nicholas T. Ingolia, and Peter Walter. 2015. “The Small Molecule ISRIB Reverses the Effects of EIF2α Phosphorylation on Translation and Stress Granule Assembly.” *ELife* 4 (February). https://doi.org/10.7554/eLife.05033.
Singhal, Anupriya, Bob T. Li, and Eileen M. O’Reilly. 2024. “Targeting KRAS in Cancer.” *Nature Medicine* 30 (4): 969–83.
Solini, Anna, Carla Iacobini, Carlo Ricci, Paola Chiozzi, Lorena Amadio, Flavia Pricci, Umberto Di Mario, Francesco Di Virgilio, and Giuseppe Pugliese. 2005. “Purinergic Modulation of Mesangial Extracellular Matrix Production: Role in Diabetic and Other Glomerular Diseases.” *Kidney International* 67 (3): 875–85.
Sousa, Cristovão M., Douglas E. Biancur, Xiaoxu Wang, Christopher J. Halbrook, Mara H. Sherman, Li Zhang, Daniel Kremer, et al. 2016. “Pancreatic Stellate Cells Support Tumour Metabolism through Autophagic Alanine Secretion.” *Nature* 536 (7617): 479–83.
Tarrado-Castellarnau, Míriam, Pedro de Atauri, and Marta Cascante. 2016. “Oncogenic Regulation of Tumor Metabolic Reprogramming.” *Oncotarget* 7 (38): 62726–53.
Thomas, Nancy E., Sharon N. Edmiston, Audrey Alexander, Pamela A. Groben, Eloise Parrish, Anne Kricker, Bruce K. Armstrong, et al. 2015. “Association Between NRAS and BRAF Mutational Status and Melanoma-Specific Survival Among Patients With Higher-Risk Primary Melanoma.” *JAMA Oncology* 1 (3): 359–68.
Trebak, Mohamed, and Jean-Pierre Kinet. 2019. “Calcium Signalling in T Cells.” *Nature Reviews. Immunology* 19 (3): 154–69.
Wan, Zhong, Tingyu Liu, Liang Wang, Rong Wang, and Hai Zhang. 2020. “MicroRNA-216a-3p Promotes Sorafenib Sensitivity in Hepatocellular Carcinoma by Downregulating MAPK14 Expression.” *Aging* 12 (18): 18192–208.
Wang, Xiaolun, Shelley Allen, James F. Blake, Vickie Bowcut, David M. Briere, Andrew Calinisan, Joshua R. Dahlke, et al. 2022. “Identification of MRTX1133, a Noncovalent,

Potent, and Selective KRASG12D Inhibitor." *Journal of Medicinal Chemistry* 65 (4): 3123–33.
Watari, N., Y. Hotta, and Y. Mabuchi. 1982. "Morphological Studies on a Vitamin A-Storing Cell and Its Complex with Macrophage Observed in Mouse Pancreatic Tissues Following Excess Vitamin A Administration." *Okajimas Folia Anatomica Japonica* 58 (4–6): 837–58.
Woods, Lucas T., Kevin Muñoz Forti, Vinit C. Shanbhag, Jean M. Camden, and Gary A. Weisman. 2021. "P2Y Receptors for Extracellular Nucleotides: Contributions to Cancer Progression and Therapeutic Implications." *Biochemical Pharmacology* 187 (May): 114406.
Wu, Zhaofa, Kaikai He, Yue Chen, Hongyu Li, Sunlei Pan, Bohan Li, Tingting Liu, et al. 2022. "A Sensitive GRAB Sensor for Detecting Extracellular ATP in Vitro and in Vivo." *Neuron* 110 (5): 770-782.e5.
Xia, Siyuan, Ruiting Lin, Lingtao Jin, Liang Zhao, Hee-Bum Kang, Yaozhu Pan, Shuangping Liu, et al. 2017. "Prevention of Dietary-Fat-Fueled Ketogenesis Attenuates BRAF V600E Tumor Growth." *Cell Metabolism* 25 (2): 358–73.
Xie, Fuchun, Bingbing X. Li, Alina Kassenbrock, Changhui Xue, Xiaoyan Wang, David Z. Qian, Rosalie C. Sears, and Xiangshu Xiao. 2015. "Identification of a Potent Inhibitor of CREB-Mediated Gene Transcription with Efficacious in Vivo Anticancer Activity." *Journal of Medicinal Chemistry* 58 (12): 5075–87.
Zeng, Meichun, Wenhua Sang, Sha Chen, Ran Chen, Hailin Zhang, Feng Xue, Zhengmao Li, et al. 2017. "4-PBA Inhibits LPS-Induced Inflammation through Regulating ER Stress and Autophagy in Acute Lung Injury Models." *Toxicology Letters* 271 (April): 26–37.
Zhang, J. H., T. D. Chung, and K. R. Oldenburg. 1999. "A Simple Statistical Parameter for Use in Evaluation and Validation of High Throughput Screening Assays." *Journal of Biomolecular Screening* 4 (2): 67–73.
Zhang, Tianyi, Yanxian Ren, Pengfei Yang, Jufang Wang, and Heng Zhou. 2022. "Cancer-Associated Fibroblasts in Pancreatic Ductal Adenocarcinoma." *Cell Death & Disease* 13 (10): 897.
Zhao, Liang, Jun Fan, Siyuan Xia, Yaozhu Pan, Shuangping Liu, Guoqing Qian, Zhiyu Qian, et al. 2017. "HMG-CoA Synthase 1 Is a Synthetic Lethal Partner of BRAFV600E in Human Cancers." *The Journal of Biological Chemistry* 292 (24): 10142–52.
Zheng, Shanliang, Xingwen Wang, Dong Zhao, Hao Liu, and Ying Hu. 2022. "Calcium Homeostasis and Cancer: Insights from Endoplasmic Reticulum-Centered Organelle Communications." *Trends in Cell Biology*, July. https://doi.org/10.1016/j.tcb.2022.07.004.
Zhou, C., W. Li, Z. Song, Y. Zhang, Y. Zhang, D. Huang, Z. Yang, et al. 2023. "LBA33 A First-in-Human Phase I Study of a Novel KRAS G12D Inhibitor HRS-4642 in Patients with Advanced Solid Tumors Harboring KRAS G12D Mutation." *Annals of Oncology* 34 (October): S1273.
Zyryanova, Alisa F., Félix Weis, Alexandre Faille, Akeel Abo Alard, Ana Crespillo-Casado, Yusuke Sekine, Heather P. Harding, et al. 2018. "Binding of ISRIB Reveals a Regulatory Site in the Nucleotide Exchange Factor EIF2B." *Science* 359 (6383): 1533–36.